STRONGLY CORRELATED SURFACE STATES

By

VICTOR A ALEKSANDROV

A dissertation submitted to the

Graduate School—New Brunswick

Rutgers, The State University of New Jersey

in partial fulfillment of the requirements

for the degree of

Doctor of Philosophy

Graduate Program in Physics and Astronomy

written under the direction of

Piers Coleman

and approved by

_____

_____

_____

_____

_____

New Brunswick, New Jersey

October, 2014

ABSTRACT OF THE DISSERTATION

Strongly correlated surface states

By VICTOR A ALEKSANDROV

Dissertation Director:

Piers Coleman

Everything has an edge. However trivial, this phrase has dominated theoretical condensed matter in the past half a decade. Prior to that, questions involving the edge considered to be more of an engineering problem rather than a one of fundamental science: it seemed self-evident that every edge is different. However, recent advances proved that many surface properties enjoy a certain universality, and moreover, are 'topologically' protected. In this thesis I discuss a selected range of problems that bring together topological properties of surface states and strong interactions. Strong interactions alone can lead to a wide spectrum of emergent phenomena: from high temperature superconductivity to unconventional magnetic ordering; interactions can change the properties of particles, from heavy electrons to fractional charges. It is a unique challenge to bring these two topics together.

The thesis begins by describing a family of methods and models with interactions so high that electrons effectively disappear as particles and new bound states arise. By invoking the AdS/CFT correspondence we can mimic the physical systems of interest as living on the surface of a higher dimensional universe with a black hole. In a specific example we investigate the properties of the surface states and find helical spin structure of emerged particles.

The thesis proceeds from helical particles on the surface of black hole to a surface of

samarium hexaboride: an f-electron material with localized magnetic moments at every site. Interactions between electrons in the bulk lead to insulating behavior, but the surfaces found to be conducting. This observation motivated an extensive research: weather the origin of conduction is of a topological nature. Among our main results, we confirm theoretically the topological properties of SmB_6; introduce a new framework to address similar questions for this type of insulators, called Kondo insulators. Most notably we introduce the idea of Kondo band banding (KBB): a modification of edges and their properties due to interactions. We study (chapter 5) a simplified 1D Kondo model, showing that the topology of its ground state is unstable to KBB. Chapter 6 expands the study to 3D: we argue that not only KBB preserves the topology but it could also explain the experimentally observed anomalously high Fermi velocity at the surface as the case of large KBB effect.

Acknowledgments

First and foremost, I am very happy to have had Piers Coleman as my adviser. I am thankful for his support and collaboration. I only hope I have acquired some of his vision and enthusiasm (not to mention his British accent). During my thesis I have had two collaborators: both Maxim Dzero and Onur Erten were very helpful, and as we dealt with Piers' absences for his numerous invited talks (that's a downside of being famous) we established a very healthy working atmosphere. I would like to thank Matt Strassler, who taught me a great deal of advanced quantum field theory and was guiding me through the hurdles of becoming a physicist, assisting with choices I made for my career, he recommended and secured my participation in TASI summer school (Boulder, Colorado), which turns out to be indeed one of the biggest growing evens in my life. In recent months of my PhD I have a pleasure talking to Pouyan Ghaemi, who also agreed to be an external member on my committee.

I would like to thank Rutgers Physics and Astronomy Department, and all members of my PhD thesis committee for their patience, encouragement and support in allowing me to switch fields during graduate program. This extends also to a great atmosphere in the physics department and I would like to thank our Graduate directors: Ron Ransome, Ted Williams and Ron Gilman who worked so hard to maintain atmosphere of excitement feeling for all of us, graduate students.

I am indebted to many students and postdocs, whose inspirational and brain-nourishing discussions defined my life here: Dima Krotov, Simon Knapen, Michael Manhart, Sanjay Arora, Bryan Leung, Sergey Aryukhin, Michael Solway, Aline Ramires, Onur Erten, Turan Birol, Lucian Pascut, Anthony Barker, Wenhu Xu, Eliav Endrey, Aleksej Mialitsin, Rishi Patel and many more.

There was a time when I was organizing/(participating in) some journal clubs, to my

great benefit. I would like to acknowledge: Matt Foster, Francesco Benini, Tzen Ong, Matthias Kaminski and Yue Zhao (AdS/CMT club), Chuck Yee, Aline Ramires, Sebastian Reyes, Sergey Aryukhin, Adina Luican, Sinisa Coh, Tahir Yusufaly, Maryam Taherinejad and many more who participated in CMT journal club.

I have greatly enjoyed learning from the Rutgers faculty, especially Piers Coleman, Matt Strassler, Sasha Zamolodchikov, David Vanderbilt, Natan Andrei, Tom Banks, Kristjan Haule and Emil Yuzbashyan.

I would like to acknowledge the financial support from Department of Energy Grant No. DE-FG02-99ER45790 and National Science Foundation Grant No. DMR 0907179. In addition, Rutgers Fellowship and TA for the beginning of my PhD and Department Gradate assistantship for a partial support of my study.

Dedication

To my family, obviously.

Most of all to my grandfather, who was the only physicist in my household but who could never speak a word about physics as he was a nuclear physicist... in the USSR.

To Valentina Fedorovna, my physics teacher.

Table of Contents

Chapter 1

Motivation: Challenge of many body physics

In this chapter I will give a brief overview of my research field. The aim is for an incoming graduate student to create a general impression. A sophisticated reader can skip this section and go straight to the next chapter.

1.1 Challenge of many body physics

The purpose of condensed matter theory is to provide a predictive model for the behavior of realistic materials. On the fundamental level the problem is well understood to astonishing level of precision: all the interactions are of charged objects with spin and ar described by quantum electrodynamics. The **ch$_{\mathbf{a}}$ll$_{\mathbf{e}}$nge** is however in the number of interacting parts of the system. Solving such a many-body problem posed a formidable challenge for the most of 20-th century and even with ever-growing computing powers will likely to remain so for a long time.

This statement can actually be made quantitative: The Hilbert space of a quantum system grows exponentially, leading to the 'Van Vleck' catastrophe. One should not seek an exact solution of systems larger than several hundred electrons can not be solved *exactly*. For example, 150 electrons would require the total number of variables to define the wave-function to be more than all the particles in the universe. "Such a wavefunction therefore is not a sensible scientific concept" (see Walter Kohns analysis of this problem, in his Nobel lecture Reviews of Modern Physics [1]). It should be noted that there are many theoretical models (especially in one spatial dimension) that can be solved exactly for infinitely large systems.

There are however many successes. In particular the theory of metals delivers many

predictions. With the exception of magnetic properties we can describe even "dirty" materials. *In a successful theory* a small number of degrees of freedom (d.o.f.) should emerge from a vast number of individual characteristics. "Emergence" became a 'buzz' word for the field of theoretical condensed matter due to a celebrated Anderson's paper [2][1].

I would like to touch on some of this advances in the next section, it will also be our first example of the **Mean Field** (MF) approximation methods which will be used extensively in the main part of this thesis.

1.2 Advances of non-interacting physics

What are the methods to approach realistic systems? What can we describe and what we can not?

We first limit our discussion to the periodic arrangements of nuclei (forming a crystal) for which we would like to add electrons. And the first question is what are the properties of the ground state (state that could be measured at low temperature)?

By non-interacting we do not actually mean that particle must not feel each other presence; rather, the main effect of interaction can be described by an effective Hamiltonian, which is bilinear in elementary fields (no scattering). In addition, due to the Pauli Exclusion Principle the systems that involve fermions (nuclei, electrons) are strongly interacting to begin with. Moreover, Coulomb interactions between electrons and nuclei are the largest scale in the problem but they can be thought as a constant external potential for free electrons (due to small electron mass as compared to proton mass). Such 'non-interacting' media can be solved with arbitrary precision, however there is no electron-electron interaction, unless there is an approach to construct an effective an effective non-interacting system.

[1] "More is different" (1972)

One such approach, density functional theory (DFT), is so successful that some might wonder why we need to invest in new techniques. In fact, DFT and its various extensions have proven extraordinarily successful in computing, on an "ab initio" basis, many key properties of more weakly interacting materials, such as, the band structure (energy of electrons as a function of their momentum), crystal structure and its distortions, elastic properties including pressure dependencies and Young's moduli, optical and even magnetic properties. It is easy to understand, how, given this success, the immense importance of DFT to condensed matter physics continues to grow.

The main idea of DFT is to replace the many body wavefunction with an electronic density $n(\vec{r})$, which is a real valued function of only three coordinates [3]. The next step is to treat every electron as a single particle problem with a potential that depends only on the density $n(\vec{r})$ of all surrounding electrons. The corresponding Schrodinger equation and the expression for density $n(\vec{r})$ must be solved *self consistently*: the electron densities computed from the occupied states must be consistent with the input density. This is our first example of **Mean Field** (MF) approximation. The 'mean field' in DFT is the density of electrons.

The critical steps in development of DFT were taken by Hohenberg, Kohn, and Sham in 1960's. Hohenberg and Kohn [3] proved several non-trivial theorems showing that in interacting systems the energy is a unique functional of the electron densities, independently of any microscopic knowledge of the many body wavefunction; for any observable, the expectation values can in principle be computed without even knowing the many-body wave function, only the density. In the next step Kohn and Sham[4] narrowed the problem by separating out the classical contributions (Coulomb and Hartree[2] energy) and more importantly, they introduced the notion of an effective one-particle wave function, used to parameterize the density $n(r) = \sum_j |\psi_j(r)|^2$ and formulated the density functional as an effective one particle problem. Strictly, the Kohn Sham eigenstates are unrelated to the quasiparticles excitations of the system, though in practice, they have often proved to be a good semi empirical description of Landau quasiparticles.

[2]The Hartree energy is the self-interaction of electron gas with density n(r): $V_{Hartree}(r) = \int dr' \frac{n(r')}{|r-r'|}$

The Kohn Sham formulation is exact with one unknown: the exchange correlation potential. Once we know the potential that can imitate the correlations between electrons we can find the exact properties of ground state by working with densities alone. The good news is that this potential is only several % of all the energy in the system. The bad news is in many materials it is what makes all the difference and the problem to find $V(n)$ is no simpler than the original one. However working with densities is much handier and many approximations can be made. Some types of approximation for the exchange correlation potential turns out to work very well, such as Local Density Approximation (LDA), Generalized Gradient Approximations (GGA) and others. The later methods and many more are what now differentiates different techniques in the density functional approaches.

1.3 Beyond the non-interacting limit: local physics

Going beyond DFT is the purpose of this thesis. DFT works well when the systen is weakly correlated and the many-body ground state is well approximated by Slater determinant. When the ground state requires the sum of several such determinants, the one particle states become heavily entangled and a new description is required. One situation in which DFT becomes unreliable is when the key low energy electronic states are localized in the vicinity of the atomic nuclei[3], as for example f-electrons in rare earth and actinide compounds.

The bulk of this thesis is motivated by or directly related to representatives of f-electron physics, and in particular, several chapters devoted to rare earth compound, samarium hexaboride SmB_6.

[3]DFT would still work very well for all delocalized electrons in the material.

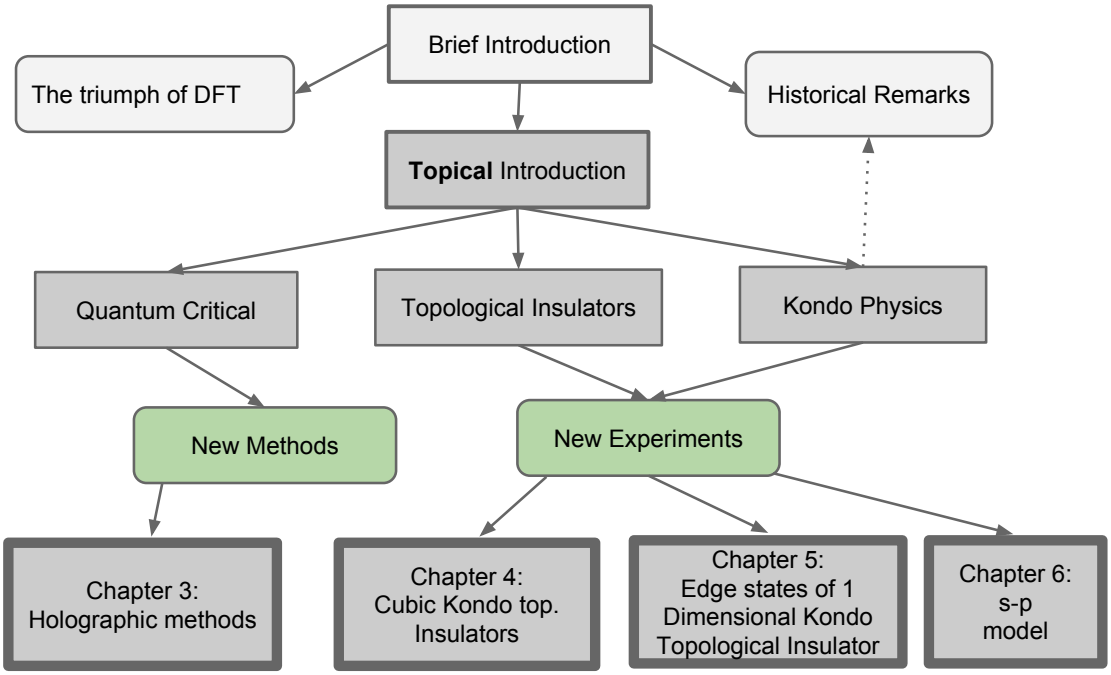

1.4 Outline of the thesis

This thesis is organized as follows

Chapter 2

Introduction and methods

In this chapter I present some of the key details needed to understand my research. It also includes discussions and snapshots of some recent experiments and guidelines from current theoretical works. The chapter consists of three parts: Topological Insulators, Kondo Insulators and Quantum Critical Kondo Metals.

In the first part the basics of topological insulators are discussed, from the definition to experimental data. The second part is devoted to a specific subfield of strongly interacting media - the Kondo lattice (where almost free conduction electrons interact with an array of local moments). The chapter ends with a discussion of quantum criticality in general and Kondo systems in particular.

There are many reviews of these topics. For Kondo insulators see [5]. To learn more on the subject of topological insulators refer to review papers [6, 7]. Note, there are many related recent developments which I did not cover here, for example the periodic table of topological states of matter which describe all possible topological indices for a given global symmetry. Another topic not covered here is that of 'topological crystalline' insulators introduced by Fu [8]. In addition there are a growing number of works that try to extend the classification to a wider class of correlated materials, where momentum is no longer a good quantum number and the topological index has to be defined in a different way. See for example the recent Science paper [9].

2.1 Topological Insulators

First, let us briefly recap the idea of band theory. For free electrons the energy as a function of momenta is the dispersion $E(\mathbf{k}) = \frac{\mathbf{k}^2}{2m}$. In the crystalline environment energy becomes a periodic function $E(\mathbf{k}) = E(\mathbf{k} + \mathbf{G})$ defined in the Brillouin zone, where G is reciprocal

vector. In the ground state all one particle states of lower energies are occupied. The locus of occupied **k** points with highest energy is then called a Fermi surface. If the empty and occupied bands are separated by a gap (Fig. 2.1) the material will be insulating, forming a "band insulator".

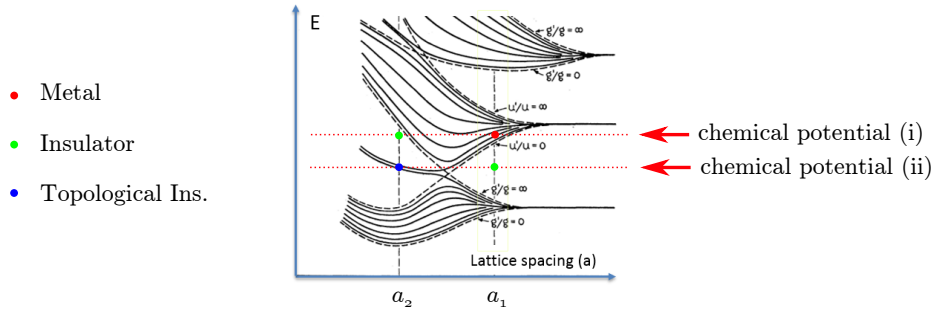

Figure 2.1: Reproduced from [10]. The energy dispersion of a one dimensional chain is shows. Black dashed lines are the band's boundaries. The bands evolve as the lattice spacing a (distance between nuclei) decreases. The insulting/conducting character is indicated for a specific choice of lattice spacing a (1 and 2) and chemical potentials (i) and (ii). One point is topological insulator and it is likely to be the first band structure calculation for a topological insulator, the paper was published in 1939.

So what is topological insulator? Topological insulators are band insulators with gapless (conducting) surface states. The surface states are protected by time reversal symmetry and they are quite different from a normal two-dimensional electron gas[1]. One of the defining characteristics of topological surface states is their helical spin structure, in which the spin is always locked to the momentum. Moreover when a one dimensional topological edge (wire) is brought into contact with a superconductor the wire develops two Majorana fermions at its ends.

What is a topological about these insulators? Topology is a basic mathematical concept that classifies objects in the same class if they can be smoothly deformed into each other. Surprisingly, one can understand the appearance of surface states using topology of band structure. The logic outlined below is often referred to as the *bulk-boundary correspondence*. Gapped quantum ground states with different topologies can not be adiabatically deformed into each other unles gapless conducting interface is formed. When two materials with different windings of their bands come into contact with each other, then, at the interface, the

[1] in case of a 3D topological insulator the surface is 2-dimensional

band structure (which was gapped in both materials) has to interpolate smoothly between them. If the gap does not close along the way, the topological index that counts the winding will be a well defined integer at every point along the interface. This is a clear ontrudiction to the assumption of different topologies, so the gap must close. Indeed, in the absence of gap the occupied bands are discontinues lines interrupted by a Fermi surface, allowing for the winding number to take any value.

Winding numbers have been used before in condensed matter to study Chern insulators (integer quantum Hall effect). They are very close in spirit to topological insulators and below some I highlight some of the aspects. The Chern number can be computed as follows

$$n = \frac{1}{2\pi} \int_{BZ} d^2k \ \mathcal{F}(\mathbf{k}) \tag{2.1}$$

where the integral is over the whole Brillouin zone and $\mathcal{F}(\mathbf{k})$ is a berry curvature $\mathcal{F} = \nabla \times \mathcal{A}$ defined through Berry connection

$$\mathcal{A} = i \sum_{n \in occ} \langle u_n | \partial_{\mathbf{k}} | u_n \rangle \tag{2.2}$$

where the summation is over all occupied bands, Bloch states of the electrons u_n are functions of $\mathbf{k}$ and $\mathbf{x}$ and are cell periodic parts of wavefunction of the corresponding band, indexed with n.

The Chern number is by construction an integer and is responsible for the extremely precise quantization in quantum Hall experiments. To show it we consider a single occupied band (n=1) and use the Stokes' theorem

$$n = \frac{1}{2\pi} \oint_{\partial BZ} d\mathbf{k} \ \cdot \mathcal{A}(\mathbf{k}) \tag{2.3}$$

where the integral is over the boundary of the Brillouin zone. As a consequence of local gauge invariance for the cell periodic functions $u \to ue^{i\phi}$ we can twist the gauge field $\mathcal{A}$ so that

$$\mathcal{A}_j = i\langle u_n | \partial_j | u_n \rangle \to i\langle 0 | u^* e^{-i\phi} \partial_j u e^{i\phi} | 0 \rangle = i\langle 0 | u \partial_j u | 0 \rangle - \partial_j \phi \langle 0 | u^* u | 0 \rangle,$$

$$\mathcal{A}_j = -\partial_j \phi,$$

hence

$$n = \frac{1}{2\pi} \oint_{\partial BZ} dk^j \partial_j \phi,$$

$$n = \frac{1}{2\pi} \oint_{\partial BZ} \phi d\phi.$$

The last equation is clearly an integer.

The integer quantum Hall effect is however only observed in high magnetic fields. It is then essential to break time reversal symmetry. In the absence of a strong magnetic field (which is rare to begin with) many materials preserve time reversal symmetry. In case of topological insulators this symmetry actually protects surface states against perturbations, except ones that violate the symmetry, such as magnetic impurities.

Time reversal symmetry, however, means that the Chern number for topological insulator is identically zero. At the first sight such a material would lose any topological protection. It turns out that even if the Chern number is equal to zero time reversal guarantees that one can split the system into two time reversal subsystems, for example, such that spin 'up' part has the Chern number $+n_\uparrow$ while spin 'down' has $n_\downarrow = -n_\uparrow$ then odd $n_\uparrow = 1, 3, 5, ...$ is a topologically non-trivial insulator. All that is left is Z_2 index

$$\nu = n_\uparrow \mod 2 \tag{2.4}$$

It can be quite tricky to calculate the topological index using the Chern number of a realistic system with multiple bands, it will never be as easy to as spin up and down. There are well defined procedures of how to split the system in half, it would take another chapter to introduce these methods. Luckily, a significant simplification was made by Fu and Kane [17], who noted that if the systems is inversion symmetric (parity invariant) the topological Z_2 index can be found as

$$(-1)^\nu = \prod_{i=1,occ}^{4} \delta(\Gamma_i), \tag{2.5}$$

according to this formula Z_2 index is defined by the parities δ at time reversal invariant points (TRIP's) Γ_i. Every TRIP is invariant under the flip of momentum. $\mathcal{T}\mathbf{k} = -\mathbf{k}$. On the lattice it means

$$\Gamma_i = -\Gamma_i + G \tag{2.6}$$

To appreciate how much of a simplification Fu-Kane formula brings to the table, note that to proceed along the above methods with the Chern number we need to solve for the wave

function everywhere. Importantly, one have to make sure it is smooth throughout the Brillouin zone. This however can be an issue, as non-trivial Chern number (and topological Z_2 index for that matter) is an obstacle in defining a smooth wavefunction. Especially as in numerics the resolution can be so not enough to distinguish between smooth and non-smooth transitions from one $\mathbf{k}$ point to another. On the other hand, the Fu-Kane formula offers to use the additional inversion symmetry to limit the calculation to just 4 points (8 points in three dimensions). At high symmetry points any Hamiltonian with Inversion symmetry can be written as

$$H(\mathbf{k} \sim \Gamma_i) = a(\mathbf{k})\hat{I} + d(\mathbf{k})\hat{P} \tag{2.7}$$

where $\hat{P}$ is parity operator that generates inversions. Then

$$\delta_i = \mathrm{sgn}(\Gamma_i) \tag{2.8}$$

In three dimensions a very non-trivial step was done by Moore and Balents [12][2] where there is no analog of the Chern number and thus time reversal topological state. Instead, three different Z_2 indices can be defined, roughly speaking ν_x, ν_y and ν_z. Together they differentiate between trivial, weak and strong topological insulator. The later must have all indices equal to 1. The weak topological insulator (defined only in 3D) is probably best thought as a stuck of layers of a two dimensional topological insulator. The term 'weak' was originally referring to its sensitivity to disorder, it is however not always the case[18]. The most significant difference is that weak topological insulators would only have surface states along fixed cuts.

Before turning to experimental evidence it is worth highlighting a little bit of history. Quite unusually, topological insulators were first predicted and then confirmed experimentally. First two papers by Kane and Mele [14] first suggested topological surface states in graphene and then introduced the Z_2 parameter [11]: pointing also to spin-orbit coupling as the tuning parameter. In 2006 Bernevig at al [15] suggested an experiment where spin-orbit interaction is much more stronger. And finally in 2007 Konig at al found the signatures of topological state in suggested CdTe/HgTe two dimensional setup. [Note: To

[2] within two weeks there were a second paper by Fu, Kane and Mele [13]

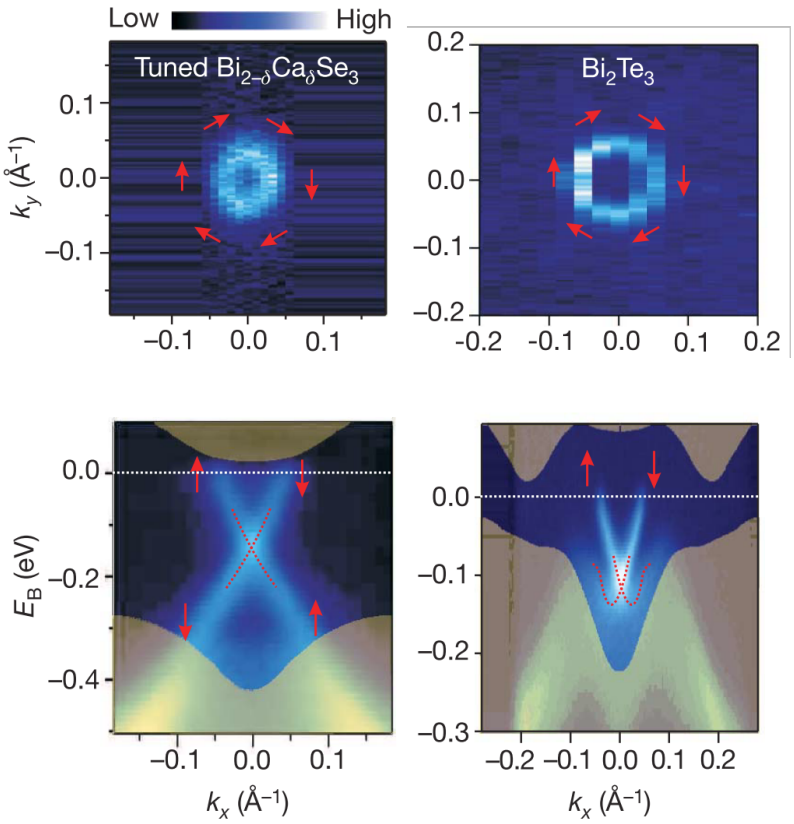

Figure 2.2: Reproduced from [16]. Dirac cone and spin-momentum locking in Bi_2Se_3 (left) and Bi_2Te_3 (right). For Bi_2Se_3 it has to be doped to restore stoichiometric pattern due to Se vacancies. Top: Fermi surface of Dirac fermions with arrows depicting the polarization of spin as measured with spin-resolved ARPES at E=-20 meV. Bottom: Dirac-like dispersion, the hallmark of topological insulators.

date no group were able to reproduce this experiment!]. Jumping ahead, the first Kondo topological insulator was also first predicted theoretically.

Experimentally one of the signatures of a topological insulator is a robust Dirac cone, protected by Kramer's degeneracy. One of the most direct techniques to measure electronic band structure of the solids and to see the Dirac cone is photoemission spectroscopy with angle resolved detection (ARPES). In experiment a strong photon source is used to pluck electrons out of the samples and measure its direction and momentum. Several original pictures for three dimensional topological insulator (Bi_xSB_{1-x} was suggested in 2007 [17] and experiment was done in 2008 by Hsieh at al [19]). I reproduce a more clear results by the same group with slightly different compounds [16] Bi_2Te_3 and Bi_2Se_3 in Fig. 2.2

To date, first generation of topological insulators (Bi_2Se_3/ Bi_2Te_3) have all been suffered

from a residual bulk conductivity [20], the chemical potential is always in the conduction band and all growth methods generate enough vacancies or impurities so that the bulk is metallic. As a result the surface effect is overshadowed by the bulk. However there are now more experiments coming on-line. The 'second generation' material Bi_2Te_2Se appears to have the chemical potential inside the gap an resistivity does grow at lower temperatures up to 6 $\Omega \cdot cm$ [21]. Such resistivity is comparable with the resistivity of a strongly correlated material SmB_6, which will be discussed in the next section.

In conclusion, (i) for uncorrelated systems there is a great deal of agreement between experiment and theory, to the extent that all the first materials were first predicted theoretically; (ii) there is a clear picture of topology linked to a winding of the wave function on a Brillouin zone.

2.2 Kondo Insulators

Correlated materials can exhibit many interesting phenomena and understanding some subclass of models can shed a light onto the whole field. We consider here one of the specific type of interactions: the Kondo interaction[22, 23], which describes the interaction of localized spins with itinerant electrons. A cartoon picture of a Kondo compound is a lattice of localized magnetic moments submerged into the sea of almost free conduction electrons. Local moments are most commonly associated with open d-shells in transition metals and open f-shells in compounds with rare earth and actinide elements.

The band structure would consist of a flat band of f-electrons (with very slow dispersion, indicating effective local nature) and an almost free quadratic band. At high temperature the two bands only weakly interact. At low temperature they start talking through Kondo effect: a crossover to a state where mobile electrons spend more and more time in a singlet bound state with local f-electron.

Two cases can happen: chemical potential is somewhere outside the gap or it is in the gap. The first case gives a hybridized band structure of a heavy fermion metal. Pictorially equivalent to a dressed electron with masses up to 1000 times larger than bare electron mass. The first material was discovered in 1975 [24]. These metallic materials are the

majority of the cases and often called heavy fermion compounds. In the second case the Kondo insulator is formed. As the gap is quite small (10-100 meV) – orders of magnitude smaller than in semiconducting materials, it is quite unlikely that the chemical potential is in the gap, however there is a handful of compounds that appears to have it in the gap. The list of Kondo insulators includes such materials as

SmB_6. $Ce_3Bi_4Pt_3$, $CeRu_4Sn_3$, CeRhAs, SmS, TmTe, TmSe, FeSi, and etc.

All of the Kondo insulators discovered to date have cubic crystal structure. This fact by itself is still unexplained and even seems counter-intuitive, because in such a high symmetry environment f-electron wavefunction would have many nodal planes and axes. In this case, if the symmetry of conduction electron (for example s-wave) does not match the symmetry of f-electron the gap will never open in the nodal directions, making it much harder to engineer any direct insulating gap.

Samarium hexaboride SmB_6, the first Kondo insulator, was discovered in the late 1960's [25]. SmB_6 is also one of the first correlated compounds studied. Now it again earned the title of the first among Kondo topological insulators.

One of the signatures of all Kondo materials is the fact that antiferromagnetic interaction with strength J get renormalized to a large value [31]. As can be clearly seen in experiments, the susceptibility shows quenching of magnetic moment at lower temperature. In the extreme limit of large J the singlet bonds are formed between local and mobile electrons. Kondo insulator is then best understood as having perfectly screened magnetic moments with an energy gap, see also Fig. 2.7(b).

2.2.1 Theory of Kondo insulator

In order to put together a theory of Kondo (topological) insulator we start form non-correlated conduction electrons with dispersion $\xi_k = \epsilon_k - \mu_c$ where ϵ_k is some periodic function of momenta. In second quantized language we can write

$$H_0 = \sum_{k,\sigma} \xi_k \; c^\dagger_{k\sigma} c_{k\sigma} \tag{2.9}$$

and the energy of interacting f-electrons is given by

$$H_f = \sum_r \epsilon^f n_r^f + \frac{1}{2} U \sum_r n_r^f (n_r^f - 1) \tag{2.10}$$

the first term defines the position of the flat f-band (infinitely flat in this case) and the second term specifies the penalty for having double occupancy, with the notations for $n_r^f = f_{r,\alpha}^\dagger f_{r,\alpha}$. $c^\dagger$ and $f^\dagger$ are creation operators, for example $f_{r\alpha}^\dagger$ creates an f-electron at coordinate r, α runs over all multiplets for f-electron, which have strong spin orbit coupling and spin is not a good quantum number. For rare earth and actinide ions, spin-orbit coupling is larger than crystal field splitting and instead of spin multiplet they combine to a total angular momentum multiplets $\vec{J} = \vec{S} + \vec{L}$. For instance, a Ce^{3+} ion has one f-electron (alternatively, Sm^{3+} has one f-hole). The state has $l = 3$ and $s = 1/2$ and the lowest in energy states have $J = 3 - 1/2 = 5/2$ (index α runs from 1 to 6, the degeneracy of 5/2 state).

The hybridization is given by

$$H_V = V_0 \sum_{r\alpha} f_{r\alpha}^\dagger c_{r\alpha} + h.c. \tag{2.11}$$

where c_α denotes the c-electron in the basis of f-electron multiplets. This can be done via a matrix of Clebsch-Gordan coefficients, called a form factor. The bare hybridization is denoted by V_0 as we will see this can be orders of magnitude larger than the one measured in the experiment.

$$c_{r\alpha} = \sum_k \Phi_{\alpha\sigma}(\hat{\mathbf{k}}) e^{-i\mathbf{k}\cdot r} c_{k\sigma} \tag{2.12}$$

The above model is a generalization of the model that was introduced for a single impurity (to treat a dilute concentration of magnetic atoms) by Anderson, thus the Kondo lattice model sometimes is referred to as Anderson lattice model or Periodic Anderson model (PAM). The interactions are maximized when they are forced to occupy the same orbital. In the limit of infinitely large U we can project out doubly occupancies out and in the special case, when the system is half filled (one f-electron per unit cell) we can enforce the constraint for every site r:

$$\sum_\alpha f_{\alpha,r}^\dagger f_{\alpha,r} = 1 \tag{2.13}$$

with this constrain one can do standard Schrieffer-Wolff transformation to obtain effective

Kondo Hamiltonian, where interaction is between spins only.

$$H_K = H_0 + J \sum_r \mathbf{S}_r \cdot \mathbf{s}_r \tag{2.14}$$

where the spin of conduction f-electrons is $\mathbf{s}_r = c^\dagger_{r\sigma} \boldsymbol{\sigma}_{\sigma\sigma'} c_{r\sigma'}$ and similar for f-electron spin $\mathbf{S}$. The effective coupling J turns out to be

$$J = \frac{V_0^2 U}{\epsilon^f(\epsilon^f + U)}. \tag{2.15}$$

2.2.2 Solving the Kondo Lattice

We would like to treat it with some kind of mean field theory treatment especially as we are hoping to apply the methods from a topological insulators section (like Fu-Kane prescription). The starting point in mean field is to decompose into a simpler interaction of MF's. The only problematic term in the Anderson model above is the density-density interaction in H_f.

We will motivate the choice of mean field parameter by first considering large U limit and use the large N to control the approximation [26, 27]. This techniques give rise to what is now called slave boson (or slave particle) approach. Where slave boson refers to a bosonic order parameter that must satisfy a constraint. One can start from Kondo Hamiltonian (2.14) where we can expanded definition of spins into a product of two creation-annihilation operators and incorporated the constraint with λ as Lagrange multiplier

$$H(U \to \infty) = H_0 - \frac{J}{N} \sum_{r,\alpha\beta} (c^\dagger_{r\alpha} f_{r\alpha})(f^\dagger_{r\beta} c_{r\beta}) + \lambda(n^f_r - Q) \tag{2.16}$$

Now the (large) number N appears in two places: in the Kondo coupling J and in enforced f-filling factor $q = Q/N$. This is a generalization of case $q = 1/2$ and $n^f = 1$ for spin 1/2 electrons. Otherwise not all terms in Hamiltonian scales with N and will become irrelevant for large N limit.

It is quite clear now that if one chooses the mean field parameter to be $V = -J/N\langle c^\dagger_{r\alpha} f_{r\alpha}\rangle$, not to be confused with the bare hybridization V_0 above, then the Hamiltonian can be rewritten as

$$H(V, \lambda) = H_0 + \sum_{r,\alpha} \left(V^*_r (c^\dagger_{r\alpha} f_{r\alpha}) + (c^\dagger_{r\alpha} f_{r\alpha}) V_r + \lambda(n^f_r - Q) + \frac{N}{J} V_r V^*_r \right). \tag{2.17}$$

This is the mean field Hamiltonian that can be solved with arbitrary precision as the size of the Hilbert space is of order of the system size. It is equally easy to put any boundary conditions and even impurities. However, it ignores all the zero-point fluctuations (for large spin s : $\langle \delta s \delta s \rangle / \langle s \rangle^2 \ll 1$), and in general should only be true for a system far from phase transitions and short-range order. It must be noted, that we can understand this particular type of decoupling as semi-classical approximation of a path integral formalism, where such a Hamiltonian can be found after doing Hubbard Stratonovich transformation.

Topological Kondo insulators

After self consistently solving Hamiltonian (2.17) one obtains the functions $\lambda(r)$ and $V(r)$. This simply renormalizes chemical potential $\epsilon^f \rightarrow \epsilon^f + \lambda$ and introduces a effective hybridization between f and conduction electrons, opening the gap. As shown schematically on Fig. 2.3 every time conduction electron band crosses the flat f-electron band there will be a gap opening as the bands always repel each other for any non-zero $|V|$. We can

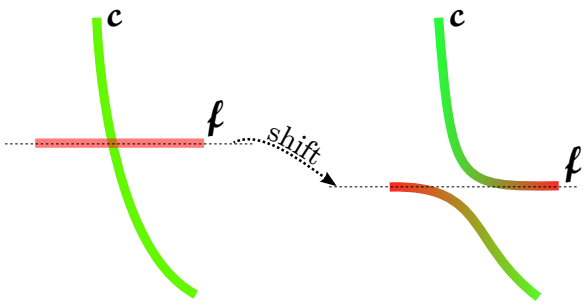

Figure 2.3: Schematic picture of the effect of interaction on the mean field level: at high temperature (left) the bands are not interacting, at lower temperature (right) energy of f level shifts (up or down) and bands start hybridizing, and can open a gap

diagonalize this Hamiltonian and solve for the wave function in case when hybridization is momentum independent (constant in space) $V(r) = V$. For example, the energy dispersion will take the form

$$E^{\pm}(k) = \frac{\epsilon_k + \lambda}{2} \pm \sqrt{\left(\frac{\epsilon_k - \lambda}{2}\right)^2 + VV^*} \tag{2.18}$$

where we for simplicity assumed the energy of original f-electron $\epsilon^f = 0$. This basic hybridization picture of Kondo inulators were first proposed by Neville Mott in the seventies [145]. The mean field approach was used in eighties [26].

Recently, before our work had started some Kondo insulators were proposed to be also topological insulators [96]. However, the predictions were made with an assumption of a tetragonal instead of cubic crystal structure. Here I would like to point out several important and pedagogical details of the previous works.

First, the solution was considered to be homogeneous in space, which would previously work well, when no surface properties were discussed. With the current view towards topology we have to admit that this approach seems to fail.

Secondly, one has to think carefully how to represent the results. There are several parameters one can tune, mainly the original f-level position ε^f (or equivalently chemical potential for conduction electrons "$-\mu_c$") and the bare hybridization. V_0, which was present in the initial Anderson lattice model (2.11). Maxim Dzero explored this parameter space and calculated the topological index while varying bare hybridization [28], the final result is reproduced in Fig. 2.4.

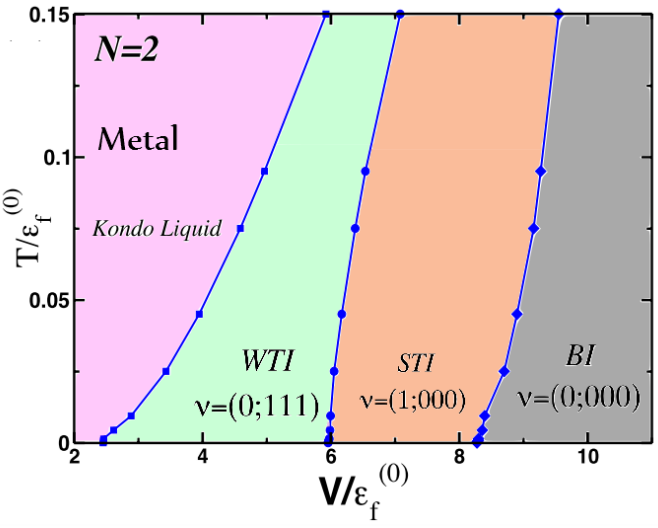

Figure 2.4: Reproduced from [28]. Phase diagram found from the solution of the mean-field equations. Kondo liquid state corresponds to the metallic state with heavy particles. WTI corresponds to weak topological insulator, STI corresponds to Strong topological insulator. BI corresponds to Band insulator. Color added for better visualization. Parameters of the model that are kept fixed are the original f-band dispersion and location $\epsilon^f = -1.05t + 0.1\epsilon_k$.

These results can be misleading, as it appears that the whole range of possibilities exists. However, this is not true. What we decided to do (for example in Chapter 4) is replot the same results as a function of Valence, by calculating the valence of Sm atoms (valence is

the charge of Sm, and can be varied from 2+ to 3+, can be measured in experiment). The same result now looks drastically different. For example, if in the WTI phase the valence is not in the physical range, a weak topological insulator phase will not be present. For zero temperature reevaluating of Fig. 2.4 is given in Fig. 2.5. Even more dramatic effect

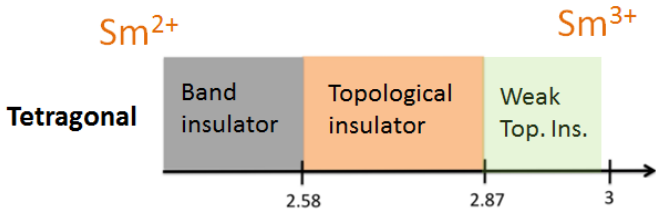

Figure 2.5: Results from Fig. 2.4 are re-plotted with valence along x-axes. The phase diagram is for zero temperature and tetragonal symmetry.

occurs when we considered a realistic cubic crystal structure (see Fig. 4.1 in Chapter 4).

2.2.3 SmB_6: The First Kondo insulator

The first Kondo insulator was discovered more than 45 years ago by Menth at al [25]. It is also one of the first correlated insulators that have been studied. The authors encounter a mystery that only recently has been understood. Menth at al measured the resistivity and saw a very convincing exponential activation, see fig. 2.6. In the paper they did not presented the data below 4K but mention in the text that below that temperature the exponential behavior breaks down. Many works that followed showed that the resistivity consistently saturates below 4K (see for example Fig. 2.8 with a more clear data). This puzzle endowed for over 40 years.

The debate on the nature of SmB_6 continued into 70s. First the metal was ruled out. Allen at al measured Hall effect to get carrier density [29]. Knowing carrier density and resistivity one can estimate the mean free path, and it turns out that it is 3×10^{-4}Åwhich is obviously impossible.

Another suggestion was that the extra conducting channels are due to impurities. This however was almost certainly ruled out by significant improvement of sample quality. Moreover, the effect still remained even when the Mott's resistance maximum criterion [30] has

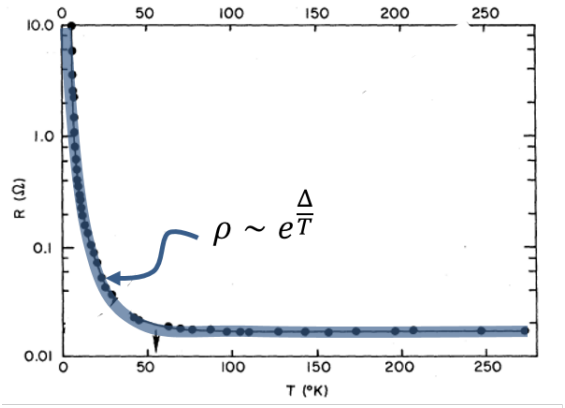

Figure 2.6: Reproduced from [25]. Resistivity as a function of temperature is measured for a bulk sample of SmB_6. Below $\sim$ 50K the resistivity grows exponentially.

been reached [32]. In a pristine SmB_6 the resistivity is extremely pressure dependent arguing in favor of an 'intrinsic' explanation of resistivity [32].

What do we know about SmB_6? We know that at high temperature it has unquenched magnetic moments because it exhibits Curie-Weiss-like magnetic susceptibility

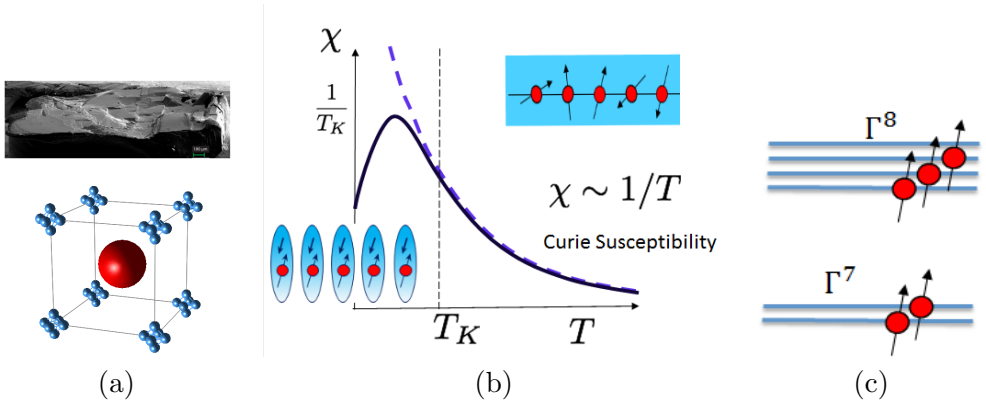

(a) (b) (c)

Figure 2.7: (a) Crystal structure of SmB_6 in one unit cell. Blue colored spheres denote Boron, red denotes Sm atoms, the photograph of the material is taken from [33] (b) The schematics of temperature dependence of susceptibility where insets show a decoupled magnetic moments for $T \gg T_K$ and fully formed Kondo Singlets at $T \ll T_K$, (c) shows a possible orientation of last five occupied levels at Γ point, the order might be reverse. Γ^7 and Γ^8 are symmetry notations

$$\chi(T) = \frac{\mu_{eff}^2}{3k_B(T - \theta_{CW})} \tag{2.19}$$

For SmB_6 $\chi(T)$ quickly drops once the spins start to quench and this signals the beginning of an bulk insulating regime. We also know its crystal structure: Sm atoms form a simple

cubic lattice separated by clusters of Boron octahedra. In case of band structure, it is close to impossible to resolve several the dispersion in f bands (meV scale), we are pretty sure what it is near Γ point ($\mathbf{k} = 0$). Static magnetic measurements show a moment that is consistent with $J = 5/2$.

We also know that the insulating gap is quite small (5-20 meV, equivalent to 50-200K) but quite robust to mechanical and electrical manipulations. Moving chemical potential by gating only had a significant effect around several volts. Under pressure, one has to reach 10 GPa to observe metal to insulator transition.

Some of these facts are summarized in the Fig. 2.7, showing a single unit cell in which the blue and red spheres denote Boron and Samarium atoms correspondingly; in (b) the schematics of temperature dependence of susceptibility is shown, with insets displaying a decoupled magnetic moments for $T \gg T_K$ and fully formed Kondo Singlets at $T \ll T_K$; (c) illustrates a possible crystal field level formed by $J = 5/2$ multiplet of Sm^{3+} ion at Γ point ($\mathbf{k} = 0$) in the cubic environment.

Recent experiments

To date over 20 experiments have been carried out that verify the surface conductivity in SmB_6, providing the appeal for the topological characteristic of the bulk insulator. Moreover, several see a hallmark feature of a topological insulators, such as the Dirac cone dispersion. In addition, at least one group observed spin polarization of the electrons – another unique property of topologically protected surface states. Below a selected few are chosen to summarize the experimental effort of 2013-2014 years.

One of the most naive experiments is to vary bulk contribution, by for example varying thickness of the sample. For the pure surface conductance one should expect that as the thickness goes down the ratio of $R(T)/R(300K)$ should go down as $R(T)/R(300K) = A \cdot d/\xi$ where A is a constant ratio of resistivities at high and low temperature, ξ is the penetration length (thickness of the conduction layer) and d is the thickness of the sample. assuming that $\xi \ll d$. This is exactly what is seen on Fig. 2.8, where the experiment from Paglione's group [34] is reproduced.

In the very first experiments the similar idea was used, but Walgast at al [35] used 8

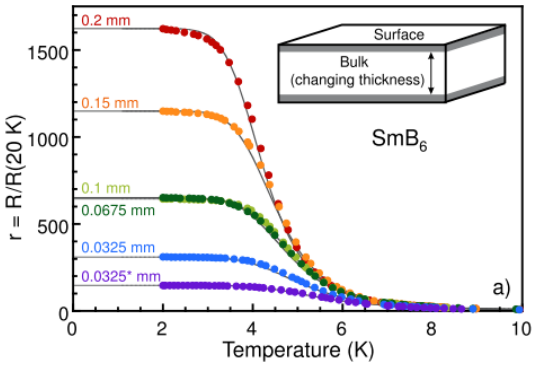

Figure 2.8: Reproduced from [34]. Dependence of SmB_6 resistivity as a function of thickness. For thinner samples the saturation happens at lower relative resistance.

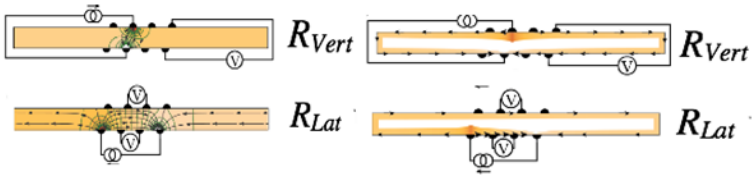

Figure 2.9: Reproduced from [35]. Setup of the Wolgast at al experiment. A cross-section of the sample along the electrical contacts. Arrows indicate current direction, green lines indicate equipotentials.

contact transport measurements on a several mm sized crystal see Fig. 2.9. For surface conduction one expects $R_{Lat} < R_{Vert}$ and for the bulk dominating conductance one expects the opposite relation $R_{Lat} < R_{Vert}$. Many more experiments follow, among them, magnetoresistance becomes surface like (two fold symmetric) as temperature lowered, Fig. 2.10a; effect of weak anti-localization (which should be present for spin locked particles) showing a topological structure Fig. 2.10b. The most direct observations of surface states are of course done by ARPES, and the first one is presented later in Fig. 5.2. Recently a more sophisticated spin resolved ARPES was done to show that spin is locked to momentum Fig. 2.10c.

Overall, there is overwhelming evidence that SmB_6 has topologically protected states and while standard methods (like DFT) fail to describe the correct band structure we will explore other possibilities to generalize and explain the topological properties of this material and hopefully pave the way to understand more materials from Kondo family and in a more broad sense - from strongly correlated family.

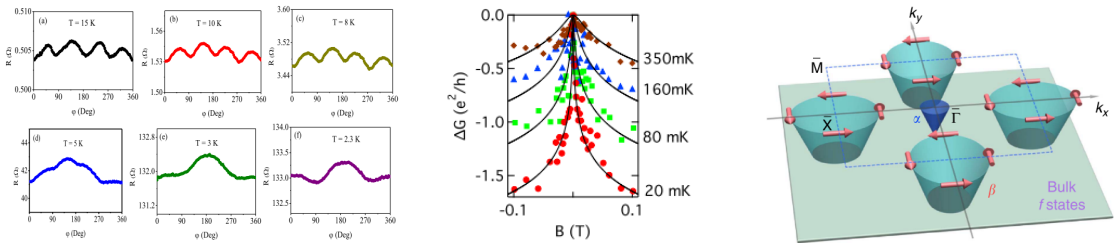

(a) (b) (c)

Figure 2.10: (a) Reproduced from [36]. The angular-dependent c-axis MR oscillations in 13 T at different temperature ranging from 15 K to 2.3 K. (b) Reproduced from [37]. Temperature evolution of weak Anti-localization effect. (c) Reproduced from [38]. Schematic of the spin-polarized surface state dispersion in the TKI SmB_6. The blue and green curved surfaces centered at the Γ and X points represent surface bands. The plane sitting below represents the bulk f states.

2.3 Quantum Critical Kondo metal

Quantum criticality refers to the state of matter at a zero temperature second-order phase transition. Such phase transitions are driven by quantum zero-point motion. In contrast to a classical critical point, in which the statistical physics is determined by spatial configurations of the order parameter, that of a quantum critical point involves configurations in space-time with a diverging correlation length and a diverging correlation time[39, 40, 41]. There is particular interest in the quantum criticality that develops in metals, where dramatic departures from conventional metallic behavior, described by Landau Fermi liquid theory[42, 43], are found to develop. Metals close to quantum criticality are found to develop a marked pre-disposition to the development of anisotropic superconductivity and other novel phases of matter[44, 45]. The strange metal phase of the optimally doped cuprate superconductors is thought by many to be a dramatic example of such phenomena[45].

Most of rare earth compounds are actually not insulators, instead they develop a heavy (slow) quasi-particles at lower temperature. Heavy fermions provide a very good playground for studying quantum criticality. On the Fig. 2.11 the generic phase diagram is shown and a very clean experiment is reproduced from ref. [46]. Superconductivity is often seen do develop in the vicinity of quantum critical points.

In quantum mechanics, the partition function can be rewritten as a Feynman path

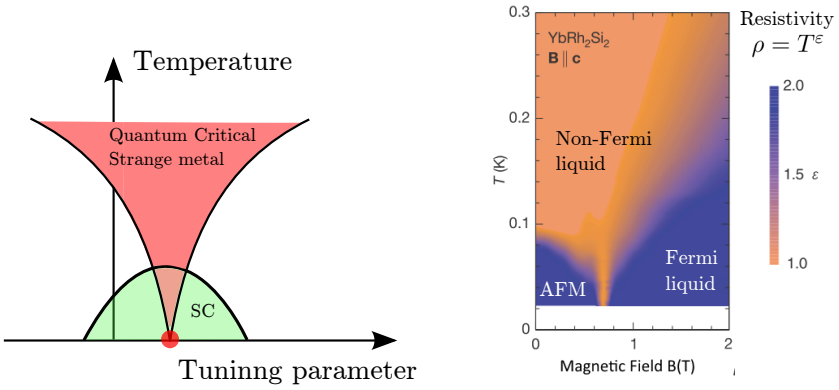

Figure 2.11: (left) Schematic phase diagram of a quantum critical point often believed to be hidden inside low energy ordered state, in this case it is superconducting dome. (Right) Reproduced form [46]. Resistivity color plot of heavy fermion rare earth compound YRh_2Si_2. The strong deviation from $\rho \sim T^2$ is observed as if it spreads from a point at zero temperature. (Quantum critical point)

integral over imaginary time.

$$Z = \mathrm{Tr}\left[e^{-\beta H}\right] = \int \mathcal{D}[\mathcal{O}] \exp\left[-\int_0^{\frac{\hbar}{k_B T}} d\tau L(\mathcal{O}, \tau)\right] \tag{2.20}$$

where L is the Lagrangian describing the interacting system and τ the imaginary time, runs from 0 to $\hbar/(k_B T)$. Inside the path integral, the physical fields $\mathcal{O}$ are periodic or anti-periodic over this interval. The path integral formulation indicates a new role for temperature: whereas temperature is a tuning parameter at a classical critical point, at a quantum critical point it plays the role of a boundary condition: a boundary condition in time[42]. When a classical critical system is placed in a box of finite extent, it acquires the finite correlation length set by the size of the box. In a similar fashion, one expects that when a quantum critical system with infinite correlation time is warmed to a small finite temperature, the characteristic correlation time becomes the "Planck time"

$$\tau_T \sim \frac{\hbar}{k_B T} \tag{2.21}$$

set by the periodic boundary conditions. This "naive scaling" predicts that dynamic correlation functions will scale as a function of $E/k_B T$. Neutron scattering measurements of the quantum critical spin correlations in the heavy fermion systems $CeCu_{6-x}Au_x$ and $UCu_{5-x}Pd_x$[47, 48] do actually show E/T scaling. The marginal Fermi liquid behavior of the cuprate metals that develops at optimal doping is also associated with such scaling. The

most direct approach to quantum criticality, pioneered by Hertz[40, 41], in which a Landau Ginzburg action is studied, adding in the damping effects of the metal. Unfortunately, the Hertz approach predicts that naive scaling would develop in antiferromagnets below two spatial dimensions. Today, the origin of E/T scaling in the cuprates and heavy fermion systems, and the many other anomalies that develop at quantum criticality constitutes an unsolved problem. A variety of novel schemes have been proposed to solve this problem, mostly based on the idea that some kind of local quantum criticality emerges [49, 50], but at the present time there is not yet an established consensus.

The hope is that there can be new methods that tackle the problem of quantum criticality, in this thesis I will explore one such possibility, called "holographic methods".

Chapter 3

Spin structure in a holographic metal

In this chapter I will present the holographic approach in a much more detailed way. Reader must note that this only scratches the surface of an enormous field that have had quickly developed several branches and many new levels of sophistication.

In this chapter we discuss two-dimensional holographic metals from a condensed matter physics perspective. We examine the spin structure of the Green's function of the holographic metal, demonstrating that the excitations of the holographic metal are "chiral", lacking the inversion symmetry of a conventional Fermi surface, with only one spin orientation for each point on the Fermi surface, aligned parallel to the momentum. While the presence of a Kramer's degeneracy across the Fermi surface permits the formation of a singlet superconductor, it also implies that ferromagnetic spin fluctuations are absent from the holographic metal, leading to a complete absence of Pauli paramagnetism. In addition, we show how the Green's function of the holographic metal can be regarded as a reflection coefficient in anti-de-Sitter space, relating the ingoing and outgoing waves created by a particle moving on the external surface.

In addition to the unconventional chiral properties at the Fermi Surface (which can be phenomenologically understood with Rashba type of interaction), holographic metals are even stranger deep below their chemical potential. We show that for the case of several Fermi surfaces the dispersion at small momenta does not look like Rashba, or any Spin-orbit type of interaction.

This chapter is primarily based on the paper with Piers Coleman [51][a].

[a] "Spin and holographic metals", published in Phys. Rev. B in 2012, editor's choice.

Early 2010's have seen a tremendous growth of interest in the possible application of "holographic methods", developed in the context of String theory, to Condensed matter

physics. Holography refers to the application of the Maldacena conjecture [52], which posits that the boundary physics of Anti-de-Sitter space describes the physics of strongly interacting field theories in one lower dimension. The hope is to use holography to shed light on the universal physics of quantum critical metals[53, 54, 55]. This chapter studies the spin character of the holographic metal, showing that its excitations are chiral in character, behaving as strongly spin-orbit coupled excitations with no inversion symmetry and spin aligned parallel to their momentum (see the end of this section).

Holographic approach

To understand the new approaches, we start with a discussion of the Maldacena conjecture, which proposes that the partition function of a quantum critical (conformally invariant) system can be re-written as a path integral for a higher dimensional gravity (or string theory) problem. In the "physical" system of interest the space-time dimension is d while in the gravity problem there is an extra coordinate r and the space time dimension is $D = d + 1$.

The Maldacena conjecture can be written as an identity between the generating functional of a d dimensional conformal field theory, and a $d + 1$ dimensional gravity problem, $Z_{\rm CFT}[j] = Z_{\rm grav}[\phi]$

$$\left\langle e^{-\int d^d x \; j(x)\,\mathcal{O}(x)} \right\rangle_{\rm CFT} = \int D[\phi] \; e^{-\int dr \int d^d x \mathcal{L}_{grav}[\phi]} \tag{3.1}$$

Here $j(x)$ is a source term coupled to the physical field $\mathcal{O}(x)$, corresponding for instance to a quasi-particle. The right hand side describes the "Gravity dual", where the gravity fields $\phi(x, r)$ must satisfy the boundary condition that they are equal to the source terms $j(x)$ on the boundary $\lim_{r\to\infty} \phi(x, r) = j(x)$. This condition establishes the relation between the variables of the d-dimensional field theory and the d+1 dimensional gravity problem in (3.1). The lower dimensional theory is conformally invariant, which implies that the state is critical in space time, i.e quantum critical. From a condensed matter perspective, the equality of the two sides implies that the physics of the quantum critical system of interest can be mapped onto the surface modes of a higher dimensional gravity problem (Fig. 3.1).

The notion that condensed matter near a quantum critical point might acquire a simpler

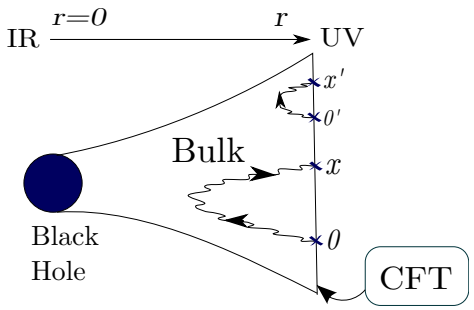

Figure 3.1: Illustrating the surface excitations "propagating" into the bulk. The vertical axis is the physical coordinate of the critical theory (CFT), while the horizontal axis is the AdS coordinate r. A physical picture for r is obtained as follows. Consider the injection and removal of a particle on the boundary of the AdS space, separated by a distance x, When the point of injection and removal are nearby, the Feynman paths connecting them will cluster near the boundary, probing *large* values of r. By contrast, when the two points are far apart, the Feynman paths connecting them will pass deep within the gravity well of the Anti-de-Sitter space, probing *small* values of r close to the black hole. In this way, the additional dimension tracks the evolution of the physics from the infra-red to the ultraviolet.

description when rewritten as a gravity dual seems at first surprising, especially considering that the higher dimensional dual is a "string theory" of quantum gravity. The essential simplification occurs in the large N limit. Here, most of the understanding derives from the particular case where the Maldacena conjecture has been most extensively studied and corroborated – a family of $SU(N)$ supersymmetric QCD models with two expansion parameters: a gauge coupling constant g and number of gauge fields N^2, as summarized in Fig. 3.2. The corresponding gravity dual, is a string theory with "string coupling constant" g_{str} and a characteristic ratio l_{str}/L between the string length l_{str} and the characteristic length of the space-time geometry where the string resides. While g_{str} controls the amplitude for strings to sub-divide, changing the genus of the world-sheet, l_{str} constrains the amplitude of string fluctuations. The correspondence implies

$$g \sim g_{str}, \quad gN \sim (L/l_{str})^4 \tag{3.2}$$

Each point of fig. 3.2 has a dual string description. For large N and small g (region **A**) the critical theory can be computed in perturbation series but a string description is extremely complicated. Some have even suggested this might be way of solving string theory by mapping it onto many body physics [56]. The focus of current interest in holographic methods is on region **B**, in the double limit $g, N \to \infty$, that corresponds to $l_{str} \to 0$ or just

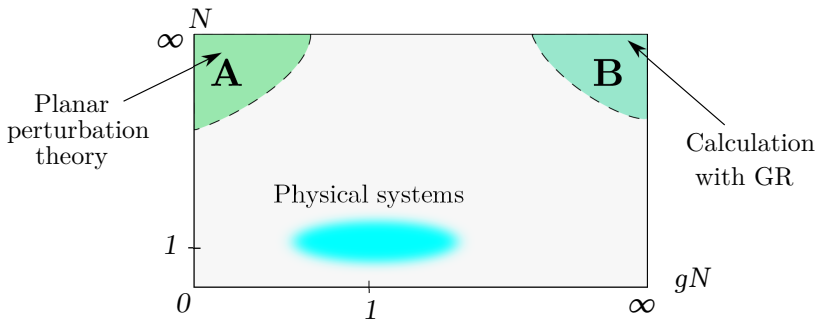

Figure 3.2: Schematic diagrams for the critical (CFT) theory. Region **A** can be computed perturbatively on CFT side but is highly non-trivial on the string theory side. This chapter is about region **B** where critical theory is strongly correlated but computable with GR. The real physical models have only $N = 1, 2$ and $g \sim 1$ and thus are in the center of the diagram.

classical gravity. In this sense then, the Maldacena conjecture, if true, provides a new way to carry out large N expansions for quantum critical systems. Since we don't yet have a working large N theory for quantum critical metals, this may be a useful way of proceeding. A similar philosophy has also been applied in the context of nuclear physics, as a way to place a theoretical limit on the viscosity of quark gluon plasmas [57].

The field is at an extraordinary juncture. On the one hand, it is still not known whether the Maldacena conjecture works for a much broader class of models, yet on the other, the assumption that it does so, has led to an impressive initial set of results. In particular, a charged black hole in Anti-de Sitter space appears to generate a strange metal [54, 53, 55], with a Fermi surface at the boundary of the space and novel anomalous exponents in the self-energy. A fascinating array of results for the strange metals have been obtained, including the demonstration of singlet pairing[58] and even the development of de Haas van Alphen oscillations in the magnetization in an applied field[59].

Motivation and results

This chapter describes our efforts to understand the ramifications of these developments. One of the motivating ideas was to develop a better physical picture of the strange metal. We were particularly fascinated by the attempt to describe high T_c superconductivity by Hartnoll at al [60, 61] (see [62] for review): in the presence of a charge condensate in the bulk, the boundary strange metal develops a singlet s-wave pair condensate [58]. The formation

of singlet s-wave pairs indicates that the strange fermions carry spin, motivating us to ask whether there is a paramagnetic spin susceptibility associated with the strange metal. This led us to examine the matrix spin-structure of fermion propagating in the strange metal.

Spin is a fundamentally three dimensional property of non-relativistic electrons, and in the absence of spin-orbit coupling it completely decouples from the kinetic degrees of freedom as an independent degree of freedom, a common situation in condensed matter physics. By contrast, in the holographic metals studied to date, the particles are intrinsically two dimensional. For these particles, derived from *two component* relativistic electron spinors, there is no spin. One way to see this is to look at two components of the fermion, which describe the electron and positron fields in two dimensions, leaving no room for spin. How then is it possible to form a spin-singlet superconductor from these fields, when there is no spin to form the singlet?

In this chapter, by examining the spin structure of holographic metals we contrast some important similarities and differences between holographic metals and real electron fluids. In our work we have two main results:

1. We show that the excitations of the strange metal are chiral[1] fermions, with spins orientated parallel to the particle momenta. Near the FS the Green's function becomes

$$G_{w\to 0} \quad = \frac{Z(w)}{\omega - v_F \boldsymbol{\sigma}\cdot\mathbf{k} + \Sigma(\omega)} + G_{\text{incoh}} \tag{3.3}$$

   The strong spin-momentum coupling generated by the term $\boldsymbol{\sigma}\cdot\mathbf{k}$ means that the Fermi surface preserves time-reversal symmetry, but violates inversion symmetry. In particular, a simple spin reversal at the Fermi surface costs an energy $2v_F k_F$, so that the spins are preferentially aligned parallel to the momenta to form chiral fermions. In this way, spin ceases to exist as an independent degree of freedom in two-dimensional holographic metals, as opposed to a spin degenerate interpretation (3.47). One of the immediate consequences of this result is that the most elementary property of metals, a Pauli susceptibility, is absent.

2. We identify an alternate interpretation of the holographic Green's functions[2] as the

[1] Here we use "chirality" in the sense adopted by condensed matter physics, to mean the helicity or handedness of a particle.

[2] We only use G to denote the retarded Green's function.

reflection coefficient of waves emitted into the interior of the Anti de Sitter space by the boundary particles, as they reflect off the black hole inside the anti-de Sitter bulk. Namely

$$G = M_k \mathcal{R}(\omega, \mathbf{k}) \tag{3.4}$$

where $\mathcal{R}$ is the reflection coefficient associated with the black hole and M_k is a known kinetic coefficient. For bosons $M_k = 1$ while for fermions $M_k = M(\omega, \mathbf{k})$ has more involved structure (3.42). The reflection $\mathcal{R}$ contains the information about the branch cuts and excitation spectra.

We discuss the full implications of these results in the last section.

3.1 Background Formalism

Our goal is to determine the holographic Green's functions using linear response theory. Here, for completeness we provide some of the background formal development[3]. For details, we refer the reader to extensive reviews[63, 64, 65, 66].

The main conjecture [52] connecting currents j in lower dimensional CFT and fields of the bulk gravity (as a limit from string theory)

$$Z_{\rm CFT}[j] = Z_{\rm grav}[\phi] \tag{3.5}$$

where ϕ and j are related by the boundary condition

$$j(x) = \lim_{r\to\infty} \phi(r; x) r^{d-\Delta} \tag{3.6}$$

the power of r reflects the scaling dimension of the source $\dim[j] = \Delta - d$. The source is coupled to the physical field, better thought as quasi particle, denoted by $\mathcal{O}(x)$. Δ is the conformal dimension of that field $\dim[\mathcal{O}] = \Delta$, namely

$$Z_{\rm CFT}[j] = \left\langle \exp\left[\int d^d x j(x)\mathcal{O}(x)\right]\right\rangle_{CFT}.$$

This generating functional determines the physics of the quantum system. The gravity part can be computed classically

$$Z_{\rm grav} = e^{-S_{\rm grav}}, \tag{3.7}$$

[3]Throughout the chapter all the quantities are dimensionless including e.g. temperature.

derivatives of the generating functional $Z[j]$ determine the Green's functions of the fields $\mathcal{O}$

$$\langle \mathcal{O} \rangle \equiv \left. \frac{\delta Z[j]}{\delta j} \right|_{j=0} = \lim_{r \to \infty} r^{\Delta - d} \frac{\delta S_{\text{grav}}[\phi]}{\delta \phi}, \tag{3.8}$$

The holographic Green's functions can be obtain from the quadratic components of the action. The equation of motion then has two independent solutions near the boundary

$$\phi = \underset{\text{in-going}}{A r^{\Delta - d}} + \underset{\text{out-going}}{B r^{-\Delta}} + \ldots, \qquad \text{as } r \to \infty \tag{3.9}$$

Usually the ingoing component A is referred as the "non-normalizable" mode, while the outgoing component B is the "normalizable" mode. Note how the exponents of r match the dimensions of the source and the response $\mathcal{O}$. In the absence of the source term j, the solution must vanish at infinity and the outgoing component vanishes. Once we turn on the source j, the Maldacena condition (3.6) that $\phi(r, x) \to j(x)$ enables us to identify A as the source

$$j \equiv A.$$

Accordingly, the outgoing mode corresponds to the response[4] $\langle \mathcal{O} \rangle$

$$\langle \mathcal{O} \rangle = const \cdot B$$

up to a numerical constant dependent on the particular theory at hand. For a free scalar $const = (2\Delta - d)$, for a fermion $const = i\gamma^t$. In a systematic treatment one needs to regulate the procedure by adding boundary terms, (see sec. 3.3).

Since the Green's function is the linear response to the source, it follows that up to a constant of proportionality

$$G = const \cdot B/A. \tag{3.10}$$

The procedure to extract the Green's function of a holographic metal is then:

1. Select a gravity Lagrangian, generally one allowing an asymptotic AdS solution with a black hole.

2. Select the bulk field content and Lagrangian.

[4] indeed, after substituting (3.9) into (3.8) and varying it w.r.t. source A (consequently setting source to zero) we are left with the term proportional to B.

3. Select one of the fields with the quantum numbers (spin, charge, etc) of the desired operator $\mathcal{O}$.

4. Solve the classical field equations in that background, including the backreaction on the gravity.

5. Find the asymptotics of the fields at the boundary. Find the Δ, outgoing (leading) and ingoing terms by comparing with (3.9).

6. The ingoing amplitude at the boundary represents the source, the outgoing amplitude gives the response, the Green's function is the ratio of the two.

Examples

We now sketch these steps for the scalar and fermion cases. The first step is to choose a background. One of the well known solutions of Einstein-Maxwell equations is the Reissner-Nordström (RN) black hole. This background involves a nontrivial electric field ($E_r = -\partial_r A_0$) and asymptotically AdS metric $g_{\mu\nu}$. In the units where horizon $r = 1$, the metric, fields and temperature T are

$$ds^2 = r^2(-f dt^2 + dx_i^2) + \tfrac{1}{r^2 f} dr^2, \tag{3.11}$$

$$f = 1 - \tfrac{Q^2+1}{r^3} + \tfrac{Q^2}{r^4}, \tag{3.12}$$

$$T = \tfrac{3-Q^2}{4\pi}, \qquad A_0 = \mu\left(1 - \tfrac{1}{r}\right). \tag{3.13}$$

Alternate solutions to the metric differ only in the profile function ("blackening factor") $f(r)$, and the horizons are defined by the zeros of $f(r)$ (as one approaches the horizon time coordinate becomes irrelevant). The solution (3.11) describes a black hole with electric charge Q in a space with negative cosmological constant. The negative cosmological constant causes the space-time to be asymptotically AdS and thus to have a boundary. The scalar potential A_0 at the boundary goes to a constant μ, the chemical potential of the boundary theory. Indeed, the RN black hole is a result of steps 1-4 for just one extra field in the bulk, gauge field A^μ, which is conjugate to the charge currant operator $\mathcal{J}^\mu$. A non-vanishing A_0 then corresponds to a finite source for $\mathcal{J}^0$, which is in fact, the chemical potential $\mu\mathcal{J}^0$.

• **Bosons**. We choose a bulk action

$$S = S_{GR} + S_{EM} + \int d^4x\sqrt{g}(-|D_\mu\varphi|^2 - m^2|\varphi|^2) \tag{3.14}$$

and the boundary term for a stable solution

$$S_{bnd} = (\Delta - d)\int_\partial d^3x\ |\varphi|^2, \tag{3.15}$$

where $S_{GR} + S_{EM}$ is Einstein-Maxwell action. (The term m^2 can sometimes be slightly negative[5]). The factor $\sqrt{g}$, where g is the determinant of the metric, makes the measure relativistically covariant. This action implies the Einstein-Maxwell equations, solved by the RN black hole background (3.11-3.13) and the Klein Gordon equation for the scalar ϕ in curved spacetime. For the boundary terms see sec. 3.3. The Klein Gordon equation in curved space is then

$$(D_\mu^2 + m^2)\varphi = 0, \tag{3.16}$$

where

$$\begin{aligned} D_\mu^2 \equiv D_\mu D^\mu = (\nabla_\mu - iqA_\mu)(\nabla^\mu - iqA^\mu) = \\ = \nabla_\mu\nabla^\mu - iq\nabla_\mu A^\mu - 2iqA^\mu\nabla_\mu - q^2A^\mu A_\mu. \end{aligned} \tag{3.17}$$

Here, the covariant derivative ∇_μ is defined in terms of the metric, for instance $\nabla^\mu\nabla_\mu\phi = \frac{1}{\sqrt{g}}\partial_\mu(\sqrt{g}\,\partial^\mu\phi)$, metric g is given in Equation (3.11). Using a little general relativity and the Fourier transformed $\varphi = \phi\ e^{-iwt+ikx}$ one can write (3.16) as (m=0)

$$\phi'' + \frac{(r^4f)'}{r^4f}\,\phi' + \frac{(\omega + qA_0)^2 - fk^2}{r^4f^2}\,\phi = 0. \tag{3.18}$$

Now we are to solve the equation to find the asymptotics and identify the ingoing and outgoing modes. Since it is a second order differential equation, the full solution can be found numerically, but the asymptotics at $r \to \infty$ are easily extracted analytically, using $f(r) \to 1$.

$$\phi'' + \frac{4}{r}\,\phi' = 0 \tag{3.19}$$

hence

$$\phi = A + Br^{-3}.$$

[5]So called BF bound [67] $m^2 \geq -9/4$ for AdS_4 with radius $L = 1$.

The leading ingoing term is a constant A, hence $\Delta = 3$, while the outgoing term should be $r^{-\Delta}$, cf. (3.9). To get the proportionality constant we use (3.8).

$$\langle \mathcal{O} \rangle = -3B, \tag{3.20}$$

so the retarded Green's function is

$$G = -3B/A \tag{3.21}$$

which is actually a $m = 0$ case for $G = (2\Delta - d)B/A$.

• **Fermions**. We can introduce the action

$$S = S_{GR} + S_{EM} + S_{\varphi} + \int d^4x\sqrt{g}\ \overline{\psi} i(\Gamma^{\mu} D_{\mu} - m)\psi \tag{3.22}$$

with $\overline{\psi} = \psi^{\dagger}\Gamma^{t}$, and Dirac gamma matrices Γ^{μ}. The boundary action

$$S_{bnd} = \int_{\partial} d^3x\ \overline{\psi}\psi. \tag{3.23}$$

A fermion in 4 dimensions has four components (e.g. spin up, spin down, electron, positron). By the nature of the duality, to incorporate the source and response at the boundary the number of boundary fermionic degrees of freedom is a half that in the bulk [68], and thus the boundary electrons have two components. In addition to the Einstein-Maxwell equation this action also implies the Dirac equation

$$(\Gamma^{\mu} D_{\mu} - m)\psi = 0 \tag{3.24}$$

The covariant derivative D_{μ} has spin connections, which can be conveniently accounted for by rescaling

$$\psi = \begin{pmatrix} \psi_+ \\ \psi_- \end{pmatrix} (g^{rr} g)^{1/4}\, e^{-i\omega t + i k_i x^i} \tag{3.25}$$

here $g_{\alpha\beta}$ are the components of the metric and $\psi_{\pm}$ are two upper and two lower components of ψ. Writing out (3.24) explicitly

$$(\sqrt{g^{rr}}\Gamma^{r}\partial_r - i\sqrt{g^{00}}\Gamma^{0} w + i\sqrt{g^{ii}}\Gamma^{i} k_i - m) \begin{pmatrix} \psi_+ \\ \psi_- \end{pmatrix}$$
$$\text{with:} \quad w = \omega + qA_0 \tag{3.26}$$

As in the scalar case, to determine Green's function, we examine the asymptotics boundary behavior, $r \to \infty$. In our basis[6]

$$\begin{pmatrix} m + r\partial_r & i\frac{\gamma^\mu k_\mu}{r} \\ i\frac{\gamma^\mu k_\mu}{r} & m - r\partial_r \end{pmatrix} \begin{pmatrix} \psi_+ \\ \psi_- \end{pmatrix} = 0, \tag{3.27}$$

here $k^\mu = (w, \mathbf{k})$. This is a 4×4 matrix equation with the following solution.

$$\psi \to r^{-\frac{3}{2}} \begin{pmatrix} \psi_+ \\ \psi_- \end{pmatrix}; \quad \begin{cases} \psi_+ = Ar^m + Dr^{-m-1} \\ \psi_- = Br^{-m} + Cr^{m-1} \end{cases} \tag{3.28}$$

From the four terms we choose in- and out-going modes in an analogous fashion to the scalar case, the leading term $Ar^{m-3/2}$ is in-going, while the term $Ar^{-m-3/2}$ is outgoing and the dimension is

$$\Delta = m + 3/2. \tag{3.29}$$

The other terms (C, D) are related to the first two. To determine this dependence we need to substitute the asymptotics back into the Dirac equation (3.24), which leads to

$$B = \frac{2m+1}{i\gamma^\mu k_\mu} D. \tag{3.30}$$

As in (3.21) the Green's function can be expressed in terms of A's and B's (note A and B are spinors):

$$GA = i\gamma^t B. \tag{3.31}$$

As before, we obtain the coefficient $i\gamma^t$ by taking a derivative of the action and γ^t is a part of the definition of $\overline{\psi}$. Armed with (3.30)

$$GA = \gamma^t \frac{2m+1}{\gamma^\mu k_\mu} D \equiv M_k D. \tag{3.32}$$

3.2 Reflection Approach

In the previous section we made use of the ingoing/outgoing terminology. In this section we identify these modes explicitly. Here we show how to redefine the problem in a form resembling the quantum mechanics of a reflected wave. This can be done by transforming

[6] In a special choice of basis, $\Gamma^r = \begin{pmatrix} 1 & 0 \\ 0 & -1 \end{pmatrix}$, $\Gamma^\mu = \begin{pmatrix} 0 & \gamma^\mu \\ \gamma^\mu & 0 \end{pmatrix}$, where $\gamma^0 = i\sigma^3$, $\gamma^x = \sigma^2$, $\gamma^2 = -\sigma^1$.

coordinates according to $ds = F(r)dr$ and rescaling the wave function as $\psi(r) = Z(r)\Psi(s)$ [69]. The original equation then becomes a zero energy scattering problem

$$(\partial_s^2 - V)\Psi(s) = 0, \tag{3.33}$$

with a complicated and non-unique function $V(s)$. (The retarded Green's function must be derived using an infalling boundary condition at the black hole horizon [70]. An advantage of this approach is that the infalling wave condition is derived as immediate consequence of the scattering problem.)

Bosons. Consider again the scalar probe Equation of motion (3.18) in the RN black hole geometry, defined in (3.11-3.13). The generalization to the full backreacting solution is straightforward. The rescaling of coordinates and fields $\varphi(r) \to \phi(s)$

$$ds = Fdr, \quad \varphi = Z\phi \tag{3.34}$$

leads to the following

$$(\partial_r^2 + D_1\partial_r + D_0)\varphi \to$$
$$(\partial_s^2 + \frac{D_1 + \frac{F'}{F} + \frac{2Z'}{Z}}{F}\partial_s + \frac{D_0 + \frac{Z''}{Z} + D_1\frac{Z'}{Z}}{F^2})\phi = 0.$$

There are an infinite number of ways to tune equation (3.18) to the form of the Schrodinger equation by canceling $\partial_s\phi$ term. We will choose the *non-unique* combination

$$F = i/fr, \qquad Z = 1/r^{3/2}. \tag{3.35}$$

This leads to the zero energy scattering problem $\partial_s^2\phi - V(s)\phi = 0$ with potential given by

$$V(r) = \frac{w^2 - k^2 f - m^2 f r^2}{r^2} - f^2\left(\frac{9}{4} + \frac{3f'}{2rf}\right) \tag{3.36}$$

It is useful to write the limiting values of this potential. It turns out that it goes to a constant on both the horizon and the boundary.

$$V(r \to \infty) = -m^2 - 9/4, \quad V(r \to \text{horizon}) = \omega^2 \tag{3.37}$$

Finally, we reformulate the Green's Function as a reflection coefficient. Namely

$$\phi(r \to \infty) = A\left(e^{is(\Delta - 3/2)} + \mathcal{R}e^{-is(\Delta - 3/2)}\right) \tag{3.38}$$

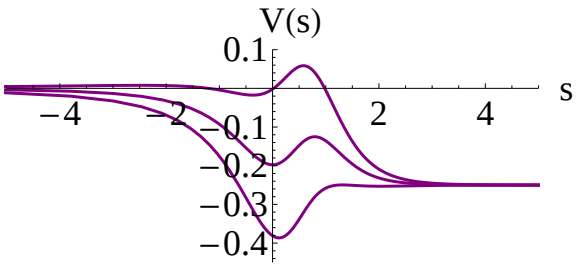

Figure 3.3: Typical Schrodinger potential $m^2 = -2,\ \ Q^2 = 3,\ k = 1, 1.6, 2,\ \omega = 0$ (from the top). The incoming wave propagates from the right with zero energy.

leading to

$$G(\omega, k) = \mathcal{R} \tag{3.39}$$

Fermions in this case the reflection coefficient becomes a matrix. We have already written the Dirac equation in the black hole background (3.27). One can "square' the first order 4×4 matrix equation to obtain a second order 2×2 equation. After rescaling the fields in the same fashion as in the scalar case, the potential acquires the same form as in the scalar case in fig. 3.3, but with the different limits

$$V(r \to \infty) = -(m + 1/2)^2, \quad V(r \to \text{horiz.}) = \omega^2. \tag{3.40}$$

As in (3.38) the solution is a superposition of incident and reflected waves:

$$\psi_+ \to \left(e^{is(m+\frac{1}{2})} + \mathcal{R}e^{-is(m+\frac{1}{2})}\right) A, \tag{3.41}$$

where the reflection coefficient $\mathcal{R}$ is now a *matrix*. The Green's function is proportional to $\mathcal{R}$ up to a kinematic factor M_k

$$G = M_k \mathcal{R} = \frac{2m + 1}{(\omega + q\mu) - \boldsymbol{\sigma} \cdot \mathbf{k}} \mathcal{R}. \tag{3.42}$$

Here we use equation (3.32). However suggestive the form of M_k is, its poles do not affect the physical non-analyticities of the Green's function G: it is $\mathcal{R}$ which contains all the relevant poles and branch cuts.

3.3 Boundary terms

The general idea of holographic renormalization [71] is to add boundary terms to the classical gravity action. This terms simply make sure that all sensible physical quantities are finite.

Good examples of such quantities are the total energy of the bulk (mass of a black hole inside) and the entropy. Those have nothing to do with duality and in some cases were introduces long before it, for instance by Hawking in 70's to actually make sense of his famous black hole temperature calculation. In AdSCFT it is useful to think about stability of a given AdS solution.

The Dirac action for fermions in the bulk is of the form

$$S = i \int d^{d+1}x\sqrt{g}\ \overline{\psi}(\gamma^\mu D_\mu - m)\psi \tag{3.43}$$

in the bulk ψ_+ and ψ_- are related through each other momenta, but the conjugate momenta for $\overline{\psi}_+$ is zero:

$$\Pi_+ = -\sqrt{\frac{g}{g_{rr}}}\psi_- \quad \text{but} \quad \overline{\Pi}_+ = 0 \tag{3.44}$$

Which is unphysical since we expect both momenta to represent a physical degree of freedom. The naive way to fix it which turns out to be the correct one is to change the bulk action by symmetrizing the kinetic term: split the derivative in half. One is acting to the left (represented by the arrow) and another is to the right.

$$S \to \frac{i}{2} \int d^{d+1}x\sqrt{g}\ \overline{\psi}(\gamma^\mu \overrightarrow{D}_\mu - \gamma^\mu \overleftarrow{D}_\mu - 2m)\psi \tag{3.45}$$

which is different from the original action by a boundary term

$$\delta S_{\text{bound}} = \int_\partial d^d x\ \sqrt{\frac{g}{g_{rr}}}\ \ \overline{\psi}_+\psi_- + h.c. \tag{3.46}$$

And we are back to equation (3.23). We refer to [68] for more details.

3.4 Spin structure

We now return to the question of the spin character of the holographic fermion. In quantum critical metals, the spin degree of freedom plays an essential role. For example, the application of a magnetic field, via the Zeeman coupling, allows one to tune the system through a quantum critical point. The presence of critical spin fluctuations is thought to play an important role in break-down of Landau Fermi liquid behavior. This then raises the question as to whether the holographic fermions obtained by mapping from four-dimensional anti-de-Sitter space, carry a spin quantum number. Furthermore, what is the nature of the

soft modes that drive the quantum criticality, and is it possible to gap these modes, driving a transition back into a Fermi liquid? The boundary fermions that form about a $D = 4$ anti-de-Sitter space are Dirac fermions described by a two component spinor. Faulkner at al [58] have shown that when a condensed Bose field [60] is introduced into the bulk gravity dual, pairing with s-wave symmetry is induced in the boundary fermions. This establishes that the boundary fermions do indeed carry spin. However, as we shall now show, this spin is "chiral"[1] and is aligned rigidly with the momentum of the excitation at the Fermi surface. There is no inversion symmetry, and at each point on the Fermi surface there is a single spin polarization. However, time reversal is not broken, and reversing the spin also implies reversing the momentum, so it is still possible to form pairs by combining fermions with opposite spin on opposite sides of the two dimensional Fermi surface.

It is often tacitly assumed that the excitations of holographic metals are *non*-relativistic fermions, with an independent spin degree of freedom. In this case the Green's function $G_{\alpha\beta} = \delta_{\alpha\beta} G$ would be proportional to the unit operator as in [72][7]

$$G_{\alpha\beta} = \delta_{\alpha\beta} \frac{1}{\omega - v_F(k - k_F) - g^2\Sigma} \tag{3.47}$$

Here we shall argue that this is not the case and the spin-orbit coupling remains very large in holographic metals despite the formation of a Fermi surface, forcing the spin to align with the momentum.

First consider the relativistic case without the black hole when the surface excitations are undoped and form a strongly interacting Dirac cone of excitations with Lorentz invariance. The corresponding Lorentz invariant correlation function is $\langle \mathcal{O}\bar{\mathcal{O}}\rangle^{-1} = \tilde{C} k_\mu \gamma^\mu$, where $\bar{\mathcal{O}} = \mathcal{O}^\dagger \gamma^0$ and $\tilde{C}$ is an arbitrary function of 3-momentum $k = \sqrt{\omega^2 - \mathbf{k}^2}$. For non-relativistic applications we are interested in $\langle \mathcal{O}\mathcal{O}^\dagger\rangle$ and we turn to a Hamiltonian formalism, treating time and space separately. The Green's functions takes the form $G^{Lor} = \langle \mathcal{O}\mathcal{O}^\dagger\rangle = -\langle \mathcal{O}\bar{\mathcal{O}}\rangle\gamma^0$

$$G^{Lor}(\omega, \mathbf{k}) = [\tilde{C}(k)(\mathbf{k}\cdot\boldsymbol{\sigma} - \omega)]^{-1}. \tag{3.48}$$

For the case of zero bulk fermion mass $\tilde{C}(k) = 1/k$. Here we have introduced the Pauli

[7] The effective model of "Semi-Holographic Fermi liquid" was proposed, with Lagrangian $\mathcal{L} = i[c^\dagger_{k,\alpha}(\omega - \epsilon_k + \mu)c_{k,\alpha} + \chi^\dagger \Sigma^{-1}\chi_\alpha + g c^\dagger_{k,a}\chi_\alpha + h.c.]$ leading to the Green's function (3.47) degenerate in α.

matrices $\sigma^i = \gamma^i\gamma^0$, for $i = 1, 2$. Eq. (3.48) describes two Dirac cones as depicted on fig.3.4-a, where upper and lower cones have the opposite chirality. There is only one spin orientation parallel to the momentum at any given energy.

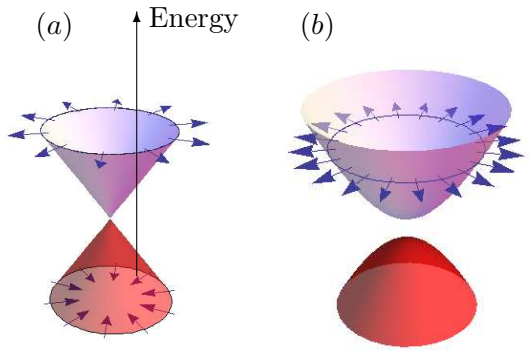

Figure 3.4: Typical dispersion and Fermi surface of Dirac fermion in 2+1 (a); and the holographic metal from fig.3.6-a (b).

Once we add a charged black-hole, the boundary excitations are "doped", acquiring a finite Fermi surface (and Fermi velocity v_F) that breaks the Lorentz invariance down to a simple rotational invariance. The only rotationally invariant way in which spin can enter, is in the form of a scalar product with the momentum $\mathbf{k} \cdot \boldsymbol{\sigma}$. The most general Green's function now takes the form

$$G(\omega, \mathbf{k}) = [C_1(\omega, k)\mathbf{k} \cdot \boldsymbol{\sigma} + C_2(\omega, k)]^{-1} \tag{3.49}$$

where C_1 and C_2 are two arbitrary functions which depend on the frequency ω and the magnitude of the non-relativistic momentum $k = |\mathbf{k}|$.

The physical properties of the theory depend on the form of the coefficients $C_{1,2}$. For example, if $C_1 = 0$, then the Fermi surface would be spin degenerate ($\boldsymbol{\sigma}$ independent). If C_1 is finite and purely real, the momentum becomes strongly coupled to the spin via $\mathbf{k} \cdot \boldsymbol{\sigma}$ (spin flip does change the ground state) and we are dealing with chiral excitations. One can interpret C_1 as a wave-function renormalization: $C_1 = v_F Z^{-1}$ and C_2 as a self energy: $C_2 = Z^{-1}(\omega + \Sigma - \mu)$. However, if C_1 has an imaginary part, while the chiral property remains, spin flips become highly incoherent in nature, so a standard decomposition of the quasiparticle along the lines of the electron phonon problem is not possible.

To bring out the chiral ($C_1 \neq 0$) properties we introduce the chirality projection operators

$$\Pi_\pm = \frac{1}{2}\left(1 \pm \frac{\mathbf{k}\cdot\boldsymbol{\sigma}}{k}\right), \tag{3.50}$$

which leads to

$$G = \Pi_+ G_{11} + \Pi_- G_{22}, \tag{3.51}$$

where G_{11} and G_{22} are the eigenvalues of the matrix G and $2kC_1 = G_{11}^{-1} - G_{22}^{-1}$, $2C_2 = G_{11}^{-1} + G_{22}^{-1}$.

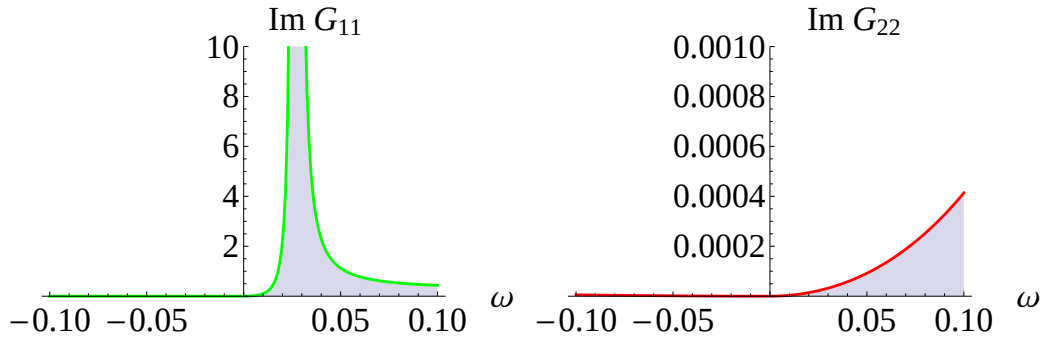

Figure 3.5: Typical behavior of a spectral function $\pi A(\omega, k) = \mathrm{Im}\, G_{11} + \mathrm{Im}\, G_{22}$ at fixed momentum $k = k_F + 10^{-2}$. $\mathrm{Im}\, G_{11}$ has a spike that sharpens for $k \to k_F$ and $\mathrm{Im}\, G_{22}$ is suppressed. Snapshot for RN black hole with $q = 2$, $m = -1/5$.

Fig. 3.5 illustrates a typical numerical solution for the eigenvalues. $\mathrm{Im}\, G_{ii}$ is plotted for fixed k close to the Fermi surface. One eigenvalue has a peak, which we interpret as the chiral quasiparticle component to the spectral function while the other, corresponding to the incoherent background created by flipping the spin anti-parallel to the momentum, lacks any sharp features and *goes to zero* at the Fermi surface. The spectral function $A(\omega, \mathbf{k}) = \frac{1}{\pi}\mathrm{Im}\,\mathrm{Tr} G$ is[2]

$$A(\omega, \mathbf{k}) = \frac{1}{\pi}\mathrm{Im}\left[G_{\mathrm{chiral}}(\omega, \mathbf{k}) + G_{\mathrm{incoh}}(\omega, \mathbf{k})\right], \tag{3.52}$$

where G_{chiral} refers to the coherent part of the resonance and G_{incoh} is the incoherent background.

To further emphasize the chiral structure we use an analytic form of the Green's function. Near $k = k_F$ and $\omega \to 0$ this can be obtained [73] by matching the infra-red 'inner' region

of the RN black hole to the asymptotic AdS 'outer' region.

$$G_{11} = \frac{z}{\omega - v_F(k - k_F) + c_1\omega^{2\nu}}, \tag{3.53}$$

where z, v_F are real and c_1 is a complex constant. The exponent $\nu \equiv \sqrt{m^2 + k_F^2 - q^2/2}/\sqrt{6}$ depends on the mass and the charge of the fermion. Armed with (3.51) we arrive to

$$G = \frac{z}{\omega - v_F(\mathbf{k}\cdot\boldsymbol{\sigma} - k_F) + c_1\omega^{2\nu}} + G_{incoh} \tag{3.54}$$

Finally it is interesting to find a dispersion for the quasi-particle: the line where the real part of the inverse G-function is zero, Re $G^{-1} = 0$. Since the imaginary part is zero only at $\omega = 0$, the Fermi surface is the intersection of the two lines. The results are illustrated in fig. 3.6. The case of a massless fermion is particularly interesting, we see that the dispersion relation actually follows a parabolic form $\sqrt{p^2 + (m^*)^2}$ showing that the holographic fermion running around the doped black hole has developed a finite effective mass m^*. The dispersion at the Fermi surface is very similar to the linear dispersion of chiral fermion.

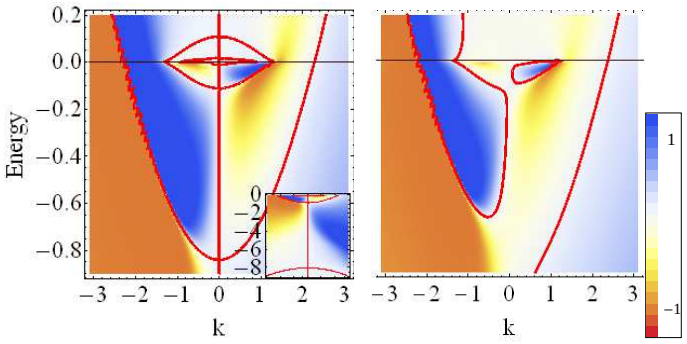

(a) $m = 0$ (b) $m = -1/10$

Figure 3.6: Density plot of Re G^{-1}. The zeros of the inverse Green's function represent the quasi-particle dispersion and are depicted by the red line (the wavy line indicates discontinuities). Left panel: $m = 0$. Right panel: $m = -0.1$. The dispersion crosses through the Fermi wavevector at zero energy. (The inset: lower energy range is shown. As in fig.3.4-b, there is a dispersion branch with a different effective mass m^*)

Summarizing the main points:

(a) The Fermi Surface is rotationally invariant and has a single non-degenerate fermionic excitation at every momenta,

(b) The spin of the coherent excitations lies parallel to the momentum as shown in figure 3.4, giving rise to chiral quasi-particle interpretation,

(c) The incoherent background is generated by a spin-flip of a coherent chiral quasiparticle.

3.5 Discussion

The possible application of holographic methods to condensed matter physics AdSCMT is based in part on a dream of a deep universality: the idea that the scale-invariance of quantum criticality in metals might enjoy the same level of universality seen in statistical physics.

Nevertheless, there is still a huge gulf to be crossed. From a String theory perspective, there is still a need to show that semi-classical gravity metric used in the theories emerges as a consistent truncation[74, 75, 76] of string theory on a certain "brane" configuration. From a condensed matter perspective, we lack a systematic method to constructing an AdS dual: one encouraging direction may be to map the renormalization group flows of the quantum theory onto a higher dimension [77].

Against this backdrop, the field has taken a more pragmatic approach of simply exploring the holographic consequences of anti-de-Sitter space, assuming that all is well. One can not fail to be impressed by the discovery that a charged black hole nucleates a strange metal on its surface, with properties that bear remarkable similarities to condensed matter systems: the emergence of a critical Fermi surface with quantum oscillations, the presence of E/T scaling, Pomeranchuk instabilities [78] and even the phase diagram of type II superconductors [79].

Our interest in the field was sparked by a naive impression that progress in holography resembles the history of condensed matter physics "running in reverse"! Rather than starting with the simple Pauli paramagnetic metal and building up to an understanding of Fermi liquids and ultimately quantum criticality, holography appears to start with the critical Fermi surface, working backwards to the most basic elements of condensed matter physics. This led us to ask, whether one calculate the most elementary property of all, the

Pauli susceptibility in response to a Zeeman splitting.

Our work has provided a interpretation of the holographic Green's function as a momentum and frequency dependent reflection coefficient of waves emitted by surface particles, reflected off the horizon of the interior black hole. We have also shown that the excitations of the strange metal are intrinsically chiral, with spins locked parallel to the momentum by a strong spin-orbit coupling with no inversion symmetry. The situation is reminiscent to the surface of 3D topological insulator.

This observation means in fact, that there is no Pauli susceptibility of the two dimensional holographic metal: the Fermi sea is already severely polarized by the relativistic coupling between momentum and spin. Indeed, from a physical perspective, the strange metallic behavior seen in these systems would appear to be a consequence of soft charge or current fluctuations rather than spin fluctuations. In recent work [58], Faulkner et al have discovered that when a charge gap is introduced by condensing a boson in the AdS bulk, the holographic metal develops sharp Fermi-liquid-like quasiparticles. This is consistent with this interpretation.

Spin plays a major role in the quantum criticality of condensed matter. In many systems, the application of a field, via the Zeeman splitting is the method of choice for tuning through criticality [46, 80]. Clearly, this part of the physics is inaccessible to the current approach. The absence of a Zeeman-splitting in holographic metals was first observed by adding a monopole charge to the black hole [81, 82].

Various authors have explored the possibility of introducing spin as an additional quantum number. The simplest example is the "magnetically charged" black hole, with an "up" and a "down" charge to simulate the Zeeman splitting, coupling to the fermions via a "minimal coupling" (a spin-dependent vector potential)[83]. By construction, this procedure does produce an explicit "Zeeman" splitting of the Fermi surface, however the infra-red character of the problem, described by the interior geometry of the gravity dual, is unchanged and the strange metal physics of the "up" and "down" Fermi surfaces are essentially unaffected by the magnetic field.

An alternative approach might be to introduce the Zeeman term to the holographic metals by invoking a non-minimal coupling to electromagnetic field, akin to the anomalous

magnetic coupling of a neutron or proton. A number of recent papers have considered the effect of such terms in the absence of a magnetic field, where they play the role of anomalous dipole coupling terms[84, 85]. At strong coupling these terms have been found to inject a gap into the fermionic spectrum interpreted as a Mott gap[85]. However, when a monopole charge is added to the black hole to generate a magnetic coupling to these same terms, we find they do not generate a splitting of the chiral Fermi surface, nor do they change the interior geometry of the gravity dual. The construction of a holographic metal with non-trivial spin physics may require considering 3-dimensional holographic metals projected out of 4+1 dimensional gravity dual [86], where the additional dimensionality permits four-component fermionic fields with both left and right-handed chiralities.

3.6 Evolution of the dispersion curves

Note: Shortly before posting our paper [51], a related work by Hertzog and Ren[87] appeared with results that complement those derived here. These authors concentrate on the behavior of gravity duals with a large black-hole charge and a non-zero fermion mass, a limit where the holographic metal contains multiple Fermi surfaces. They find that in this limit, in addition to a Rashba component $\boldsymbol{\sigma} \cdot (\hat{z} \times \mathbf{k})$ the dispersion of the holographic metal also develops a quadratic spin-independent dispersion reminiscent of more weakly spin-orbit coupled fermions. The Rashba term $\boldsymbol{\sigma} \cdot (\hat{z} \times \mathbf{k})$ obtained by Herzog and Ren is equivalent to the helicity term $\boldsymbol{\sigma} \cdot \mathbf{k}$ described in our paper after a rotation of spin axes. In the limit of small black-hole charge considered here, with a single Fermi surface, the helicity term in the Hamiltonian entirely dominates the spectrum.

In response to and motivated by the results of Hertzog and Ren [87] we tried to investigate the addition of more Fermi surfaces (by 'doping' more excitations) and the interaction between them. So far we established the spin character of the holographic fermion for a small doping μ.

If the doping μ is increased, we find (in accordance to previous works) multiple co-centric Fermi surfaces, as schematically plotted on the fig. 3.7. The circles are approximately evenly

spaced and the spin character alternates. We can assume for concreteness that the largest Fermi surface is right handed (spin is aligned with momentum).

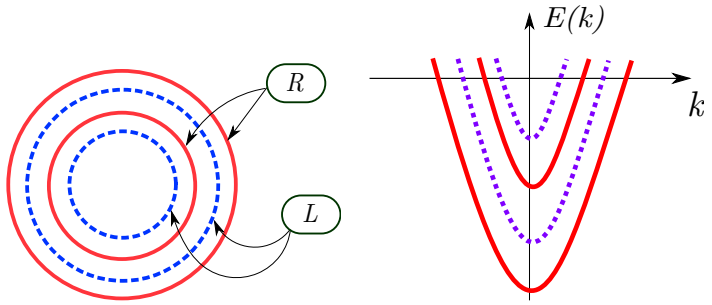

Figure 3.7: Left: Illustrating the multiple Fermi surface Of the holographic metals at high doping. The horizontal and vertical axes are k_x and k_y. Right: same picture but dispersion is shown. Dashed and solid lines are for the left and right handed fermions correspondingly.

It will sufficient to focus only on the two largest Fermi surfaces. We plot numerical result of dispersion is in fig. 3.8. The dispersion is defined as the zeros of the real part of the inverse Green's function. Here we use the same gravity setup of a near-extreme AdS Reissner-Nordström (RN) black hole. The RN setup is characterized by three parameters: temperature T, chemical potential μ and mass of the bulk fermionic field m. In fig. 3.8 the mass is zero, the stress of this section is on the non-zero mass.

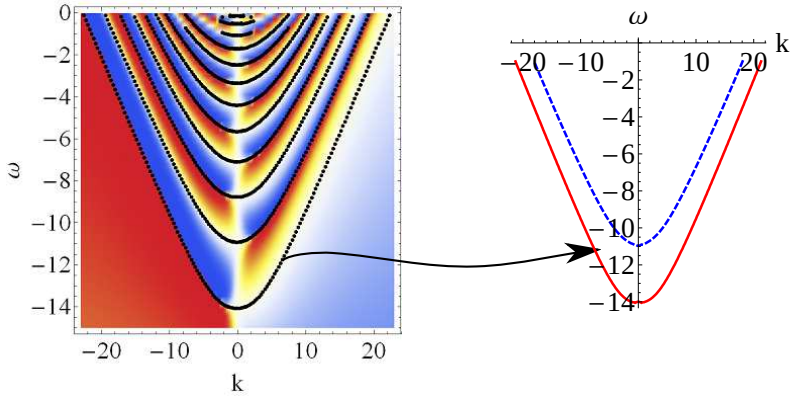

Figure 3.8: The density plot of the real part of G^{-1} for m=0. The quasi-particle dispersion curves are depicted by the solid black lines. The two lowest lines are shown separately, with the notations as in fig. 3.7. The other parameters are: $\mu/T = 300$, bulk fermion charge is $q = 17.5$

To construct the dispersion from the density plot of the $\mathrm{Re}\, G^{-1}$ (see fig. 3.8) we use the fact that system is time reversal invariant: we can first numerically find the zeros

(corresponding to the white color in the density plot) with vanishingly small numerical error. Then reflect the dispersion around the Vertical axis. The black solid curves on the top fig. 3.9 shows the result of this action for the dispersion. We only focus on the two largest dispersion curves.

Close to the Fermi energy ($\omega = 0$) the behavior is sometimes possible to extract analytically [73] . In the RN case it is [51]

$$G = \frac{z}{\omega - v_F(\mathbf{k}\cdot\boldsymbol{\sigma} - k_F) + h\omega^{2\nu}} + G_{incoh} \tag{3.55}$$

where z, v_F are real and h is a complex constants defined by numerics, $\boldsymbol{\sigma} = (\sigma^x, \sigma^y)$ are the two Pauli matrices; the exponent ν

$$\nu = \sqrt{m^2 + k_F^2 - q^2/2}/\sqrt{6} \tag{3.56}$$

depends on the mass and the charge of the fermion. two comments are in order here:

- The scattering rate is defined as $\mathrm{Im}\,[h\omega^{2\nu_2}]$, from (3.56) the exponent ν grows linear in k_f for large values of k_F. For the usual parameters at large doping, the exponent is of order 20.
- When the exponent ν crosses 1/2 the quasi particles become unstable, so that all small Fermi surfaces should not be considered.

Unfortunately to see more than one Fermi surface at low temperature one has to use high doping and hence all the Fermi surfaces would have very large exponents.

3.6.1 A non-zero mass

Through eq. (3.56) that mass changes the infra-red (IR) exponent of the field theory but as we show below it actually has a more interesting consequences. In fig. 3.9 we plot the result for $m \neq 0$. At any non-zero value of m one can see two curves reach each other on the midway. Very interestingly, when the mass is large enough the curves look like two shifted "parabolas" as it is common for the Rashba term except the spin independent part in Rashba Hamiltonian is k^2.

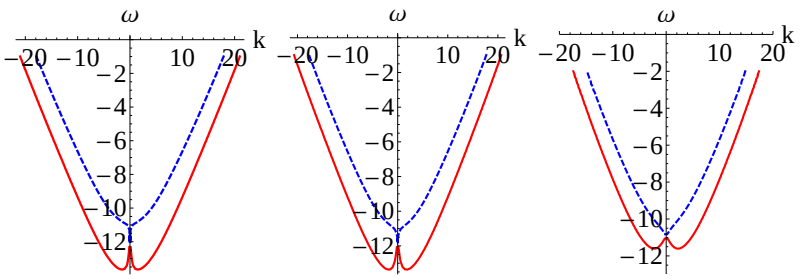

Figure 3.9: Only the two lowest dispersion curves are shown for non-zero mass: $m = 0.1, 0.2, 0.5$. The other parameters are: $\mu/T = 300$, bulk fermion charge is $q = 17.5$

It was noticed before in the paper by Herzog and Ren [87] where they studied the spectral function for the same parameters and found multiple sets of the curves like in fig 3.9. They were the first to point out the similarity with Rashba Hamiltonian

3.6.2 Effective model

Each Fermi surface can be thought of a separate species of fermions with different k_F and Consequently exponent ν. for the two largest Fermi-surfaces we can write two copies of such a Green's function and corresponding effective Hamiltonian would take the (matrix) form:

$$H_0 = \sum_{k,\sigma} c_1^\dagger \left[v(k)\mathbf{k}\cdot\boldsymbol{\sigma} + h_1\omega^{2\nu_1} - \mu_1 \right] c_1 + \sum_{k,\sigma} c_2^\dagger \left[v(k)\mathbf{k}\cdot\boldsymbol{\sigma} + h_2\omega^{2\nu_2} - \mu_2 \right] c_2 \tag{3.57}$$

to reproduce the relativistic dispersion we assume that $v(k) = \frac{1}{k}\sqrt{k^2 + m_*^2}$

It follows that from fig. 3.9 that the mass mixes two "bands" only at the small momenta. It is natural to propose the effective mixing term proportional to the mass

$$H = H_0 + i\sum_{k,\sigma}[V(k)c_1^\dagger c_2 + h.c.] \tag{3.58}$$

$$V(k) = m\frac{\mu_1 - \mu_2}{2\sqrt{m^2 + k^2}} \tag{3.59}$$

Where the k^2 in the denominator is the consequence of the dispersion in the free Hamiltonian (3.57). Hybridization $V(k)$ thus has very singular dependence near small mass and small momenta. Fig. 3.10 shows the dispersion relations after diagonalizing the full Hamiltonian $H = H_0 + H_V$.

$$E_\pm(k) = \frac{1}{2}[2v(k)k - \mu_1 - \mu_2 \pm \sqrt{(\mu_1 - \mu_2)^2 - 4V(k)^2}] \tag{3.60}$$

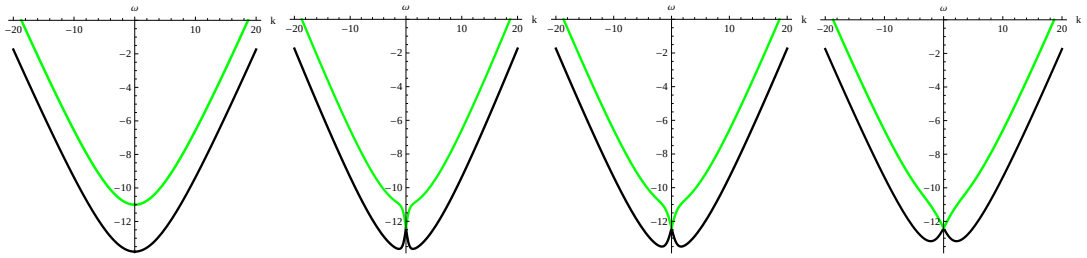

Figure 3.10: The hybridization described by the effective mixing term for $m = (0,\ 0.1,\ 0.2,\ 0.5)$.

Conclusions

In this additional section an interesting behavior of the hybridization $V(k)$ (simple non-physical fit of the dispersion) was shown. It paves the way to argue that observation by Hertzog and Ren[87] is clouded by the choice of their parameters and in fact this band structure does not look like Rashba coupling (near the bottom of the band) - unless large value of m is chosen. Conventionally non-zero hybridization V produces avoided crossings of two intersecting bands, but here we see the opposite. Furthermore, this "hybridization" is not smooth in the fermionic mass m, that is one of the parameters of the gravity dual.

We note however, that the features far away from chemical potential should not affect any physics of the Fermi surface. It would be interesting to analyze the same dispersion curves for different holographic metals.

Chapter 4

Cubic Kondo Topological Insulator

Current theories of Kondo insulators employ the interaction of conduction electrons with localized Kramers doublets originating from a **tetragonal** crystalline environment, yet all Kondo insulators are cubic. Here we develop a theory of **cubic** topological Kondo insulators involving the interaction of Γ_8 spin quartets with a conduction sea. The spin quartets greatly increase the potential for strong topological insulators, entirely eliminating the weak-topological phases from the diagram. We show that the relevant topological behavior in cubic Kondo insulators can only reside at the lower symmetry X or M points in the Brillouin zone, leading to a three Dirac cones with heavy quasiparticles.

Another important difference between cubic and tetragonal symmetries is that in the later case the limit of integer valence was predicted *not* to support topological property. On the other hand, cubic symmetry allows for the topological order to "extend" all the way to integer valence. Thus providing a good basis for considering various Kondo-like (integer valent) models to study topology of relevant cubic Kondo insulators. The last point is the essential link to my work in chapters 5 and 6.

This chapter is based on my paper with Piers Coleman and Maxim Dzero [88][a]

[a] "Cubic Topological Kondo Insulators", published in Phys. Rev. Letters in 2013

4.1 Review the model with tetragonal crystal symmetry

Earlier in 2010 seminal paper by Maxim Dzero, Kai Sun, Piers Coleman, Victor Galitski started a stream of activity which turns out quite fruitful for the community. The main prediction of this paper is that in spite of all the difficulties in correlated materials and some ambiguities, some of Kondo insulators can be topological and thus can have conducting

surfaces.

To simplify matters they assumed tetragonal symmetry, so that it is possible to focus on a doublet for f-electron, that will hybridize in ll direction (L= 1/2).

4.2 Motivation for my study

Our classical understanding of order in matter is built around Landau's concept of an order parameter. The past few years have seen a profound growth of interest in topological phases of matter, epitomized by the quantum Hall effect and topological band insulators, in which the underlying order derives from the non-trivial connectedness of the quantum wave-function, often driven by the presence of strong spin-orbit coupling [17, 12, 89, 90, 91, 92, 93, 94, 95].

One of the interesting new entries to the world of topological insulators, is the class of heavy fermion, or "Kondo insulators" [22, 23, 96, 97, 98, 99, 100]. The strong-spin orbit coupling and highly renormalized narrow bands in these intermetallic materials inspired the prediction [96] that a subset of the family of Kondo insulators will be Z_2 topological insulators. In particular, the oldest known Kondo insulator SmB_6[25] with marked mixed valence character, was identified as a particularly promising candidate for a strong topological insulator (STI): a conclusion that has since also been supported by renormalized band-theory[97, 100]. Recent experiments [101, 102, 103] on SmB_6 have confirmed the presence of robust conducting surfaces, large bulk resistivity and a chemical potential that clearly lies in the gap providing strong support for the initial prediction.

However, despite these developments, there are still many aspects of the physics in these materials that are poorly understood. One of the simplifying assumptions of the original theory [96] was to treat the f-states as Kramer's doublets in a tetragonal environment. In fact, the tetragonal theory predicts that strong topological insulating behavior requires large deviations from integral valence, while in practice Kondo insulators are much closer to integral valence [23]. Moreover, all known Kondo insulators have cubic symmetry, and this higher symmetry appears to play a vital role, for all apparent "Kondo insulators" of lower symmetry, such as CeNiSn[104] or $CeRu_4Sn_6$[105] have proven, on improving sample

quality, to be semi-metals. One of the important effects of high symmetry is the stabilization of magnetic f-quartets. Moreover, Raman[106] experiments and various band-theory studies[107, 108] that it is the Kondo screening of the magnetic quartets that gives rise to the emergence of the insulating state.

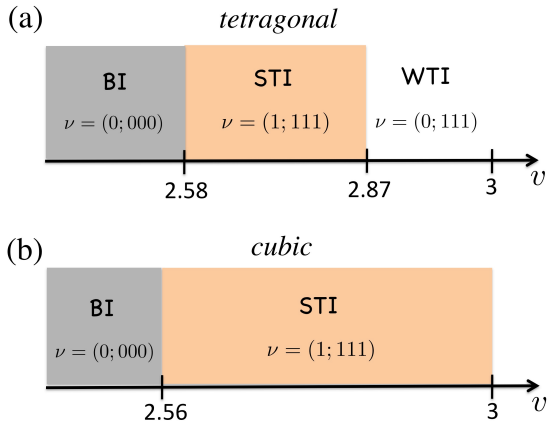

Figure 4.1: Contrasting the phase diagram of tetragonal [28] and cubic topological Kondo insulators. Cubic symmetry extends the STI phase into the Kondo limit. For SmB_6 $v = 3 - n_f$ gives the valence of the Sm ion, while n_f measures the number of f-holes in the filled $4f^6$ state, so that $n_f = 1$ corresponds to the $4f^5$ configuration.

Motivated by this observation, here we formulate a theory of cubic topological Kondo insulators, based on a lattice of magnetic quartets. We show that the presence of a spin-quartet greatly increases the possibility of strong topological insulators while eliminating the weak-topological insulators from the phase diagram, Fig. 4.1. We predict that the relevant topological behavior in simple cubic Kondo insulators can only reside at the lower point group symmetry X and M points in the Brillouin zone (BZ), leading to a three heavy Dirac cones at the surface. One of the additional consequences of the underlying Kondo physics, is that the coherence length of the surface states is expected to be very small, of order a lattice spacing.

While we outline our model of cubic Kondo insulators with a particular focus on SmB_6, the methodology generalizes to other cubic Kondo insulators. SmB_6 has a simple cubic structure, with the B_6 clusters located at the center of the unit cell, acting as spacers which mediate electron hopping between Sm sites. Band-theory [108] and XPS studies [109] show that the 4f orbitals hybridize with d-bands which form electron pockets around the X points.

In a cubic environment, the $J = 5/2$ orbitals split into a Γ_7 doublet and a Γ_8 quartet, while the fivefold degenerate d-orbitals are split into double degenerate e_g and triply degenerate t_{2g} orbitals. Band theory and Raman spectroscopy studies [106] indicate that the physics of the $4f$ orbitals is governed by valence fluctuations involving electrons of the Γ_8 quartet and the conduction e_g states, $e^- + 4f^5(\Gamma_8^{(\alpha)}) \rightleftharpoons 4f^6$. The $\Gamma_8^{(\alpha)}$ ($\alpha = 1, 2$) quartet consists of the following combination of orbitals: $|\Gamma_8^{(1)}\rangle = \sqrt{\frac{5}{6}}\left|\pm\frac{5}{2}\right\rangle + \sqrt{\frac{1}{6}}\left|\mp\frac{3}{2}\right\rangle$, $|\Gamma_8^{(2)}\rangle = \left|\pm\frac{1}{2}\right\rangle$. This then leads to a simple physical picture in which the Γ_8 quartet of f-states hybridizes with an e_g *quartet* (Kramers plus orbital degeneracy) of d-states to form a Kondo insulator.

To gain insight into how the cubic topological Kondo insulator emerges it is instructive to consider a simplified one-dimensional model consisting of a quartet of conduction d-bands hybridized with a quartet of f-bands (Fig. 4.2a). In one dimension there are two high symmetry points: Γ ($k = 0$) and X ($k = \pi$), where the hybridization vanishes [96, 98, 28]). Away from the zone center Γ, the $f-$ and $d-$ quartets split into Kramers doublets. The Z_2 topological invariant ν_{1D} is then determined by the product of the parities $\nu_{1D} = \delta_\Gamma \delta_X$ of the occupied states at the Γ and X points. However, the f-quartet at the Γ point is equivalent to two Kramers doublets, which means that $\delta_\Gamma = (\pm 1)^2$ is always positive, so that $\nu_{1D} = \delta_X$ and a one-dimensional topological insulator only develops when the f and d bands invert at the X point.

Generalizing this argument to three dimensions we see that there are now four high symmetry points Γ, X, M and R. The f-bands are fourfold degenerate at both Γ and R points which guarantees that $\delta_\Gamma = \delta_R = +1$ (Fig. 4.2b). Therefore, we see that the 3D topological invariant is determined by band inversions at X or M points only, $\nu_{3D} = (\delta_X \delta_M)^3 = \delta_X \delta_M$. If there is a band inversion at the X point, we get $\nu_{3D} = \delta_X \delta_M = -1$. In this way the cubic character of the Kondo insulator and, specifically, the fourfold degeneracy of the f-orbital multiplet protects the formation of a strong topological insulator.

4.3 The model

We now formulate our model for cubic topological Kondo insulators. At each site, the quartet of f and d -holes is described by an orbital and spin index, denoted by the combination

$\lambda \equiv (a, \sigma)$ ($a = 1, 2$, $\sigma = \pm 1$). The fields are then given by the eight component spinor

$$\Psi_j = \begin{pmatrix} d_\lambda(j) \\ X_{0\lambda}(j) \end{pmatrix} \tag{4.1}$$

where $d_\lambda(j)$ destroys an d-hole at site j, while $X_{0\lambda}(j) = |4f^6\rangle\langle 4f^5, \lambda|$ is the the Hubbard operator that destroys an f-hole at site j. The tight-binding Hamiltonian describing the hybridized f-d system is then

$$H = \sum_{i,j} \Psi^\dagger_\lambda(i) h_{\lambda\lambda'}(\mathbf{R}_i - \mathbf{R}_j) \Psi_{\lambda'}(j) \tag{4.2}$$

in which the nearest hopping matrix has the structure

$$h(\mathbf{R}) = \begin{pmatrix} h^d(\mathbf{R}) & V(\mathbf{R}) \\ V^\dagger(\mathbf{R}) & h^f(\mathbf{R}) \end{pmatrix}, \tag{4.3}$$

where the diagonal elements describe hopping within the d- and f- quartets while the off-diagonal parts describe the hybridization between them, while $\mathbf{R} \in (\pm\hat{\mathbf{x}}, \pm\hat{\mathbf{y}}, \pm\hat{\mathbf{z}})$ is the vector linking nearest neighbors. The various matrix elements simplify for hopping along the z-axis, where they become orbitally and spin diagonal:

$$h^l(\mathbf{z}) = t^l \begin{pmatrix} 1 & \\ & \eta_l \end{pmatrix}, \qquad V(\mathbf{z}) = iV \begin{pmatrix} 0 & \\ & \sigma_z \end{pmatrix}. \tag{4.4}$$

where $l = d, f$ and η_l is the ratio of orbital hopping elements. In the above, the overlap between the $\Gamma_8^{(1)}$ orbitals, which extend perpendicular to the z-axis is neglected, since the hybridization is dominated by the overlap of the the $\Gamma_8^{(2)}$ orbitals, which extend out along the z-axis. The hopping matrix elements in the $\mathbf{x}$ and $\mathbf{y}$ directions are then obtained by rotations in orbital/spin space (see Section 4.4.1). so that $h(\mathbf{x}) = U_y h(\mathbf{z}) U_y^\dagger$ and $h(\mathbf{y}) = U_{-x} h(\mathbf{z}) U_{-x}^\dagger$ where U_y and U_{-x} denote 90° rotations about the y and negative x axes, respectively.

The Fourier transformed hopping matrices $h(\mathbf{k}) = \sum_{\mathbf{R}} h(\mathbf{R}) e^{-i\mathbf{k}\cdot\mathbf{R}}$ can then be written in the compact form

$$h^l(\mathbf{k}) = t^l \begin{pmatrix} \phi_1(\mathbf{k}) + \eta_l \phi_2(\mathbf{k}) & (1-\eta_l)\phi_3(\mathbf{k}) \\ (1-\eta_l)\phi_3(\mathbf{k}) & \phi_2(\mathbf{k}) + \eta_l \phi_1(\mathbf{k}) \end{pmatrix} + \epsilon^l, \tag{4.5}$$

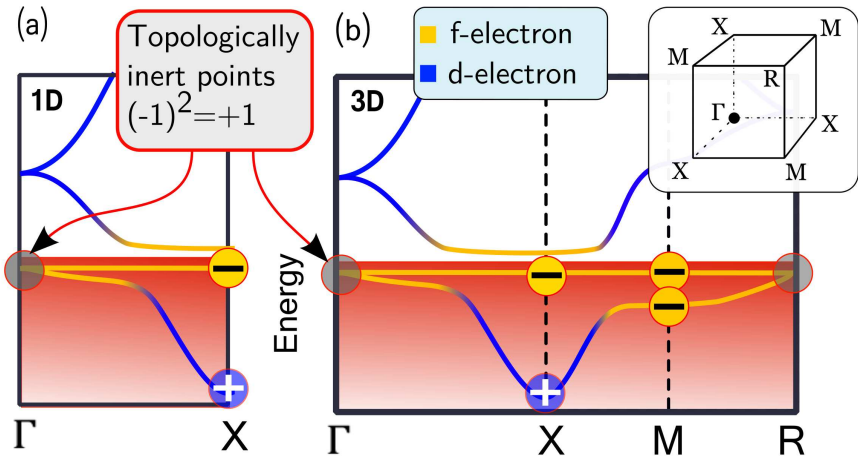

Figure 4.2: Schematic band structure illustrating (a) 1D Kondo insulator with local cubic symmetry and (b) 3D cubic Kondo insulator. Hybridization between a quartet of d-bands with a quartet of f-bands leads to a Kondo insulator. The fourfold degeneracy of the f- and d-bands at the high symmetry Γ and R points of the Brillouin zone guaranties that the 3D topological invariant is determined by the band inversions at the X and M points only.

where $l = d, f$. Here ϵ^l are the bare energies of the isolated d and f-quartets, while $\phi_1(\mathbf{k}) = c_x + c_y + 4c_z$, $\phi_2(\mathbf{k}) = 3(c_x + c_y)$ and $\phi_3(\mathbf{k}) = \sqrt{3}(c_x - c_y)$ ($c_\alpha \cos k_\alpha, \alpha = x, y, z$). The hybridization is given by

$$V(\mathbf{k}) = \frac{1}{6}\begin{pmatrix} 3(\bar{\sigma}_x + i\bar{\sigma}_y) & \sqrt{3}(\bar{\sigma}_x - i\bar{\sigma}_y) \\ \sqrt{3}(\bar{\sigma}_x - i\bar{\sigma}_y) & \bar{\sigma}_x + i\bar{\sigma}_y + 4\bar{\sigma}_z \end{pmatrix} \tag{4.6}$$

where we denote $\bar{\sigma}_\alpha = \sigma_\alpha \sin k_\alpha$. Note how the hybridization between the even parity d-states and odd-parity f-states is an odd parity function of momentum $V(\mathbf{k}) = -V(-\mathbf{k})$.

To analyze the properties of the Kondo insulator, we use a slave boson formulation of the Hubbard operators, writing $X_{\lambda 0}(j) = f^\dagger_\lambda(j) b_j$, where $f^\dagger_\lambda|0\rangle \equiv |4f^5, \lambda\rangle$ creates an f-hole in the Γ^8 quartet while $b^\dagger|0\rangle \equiv |4f^6\rangle$ denotes the singlet filled $4f$ shell, subject to the constraint $Q_j = b^\dagger_j b_j + \sum_\lambda f^\dagger_{j\lambda} f_{j\lambda} = 1$ at each site.

We now analyze the properties of the cubic Kondo insulator, using a mean-field treatment of the slave boson field b_i, replacing the slave-boson operator $\hat{b}_i$ at each site by its expectation value: $\langle \hat{b}_i \rangle = b$ so that the f- hopping and hybridization amplitude are renormalized: $t_f \to b^2 t_f$ and $V_{df} \to b V_{df}$. The mean-field theory is carried out, enforcing the constraint $b^2 + \langle n_f \rangle = 1$ on the average. In addition, the chemical potentials ϵ_d and ε_f for both d-electrons and f-holes are adjusted self-consistently to produce a band insulator,

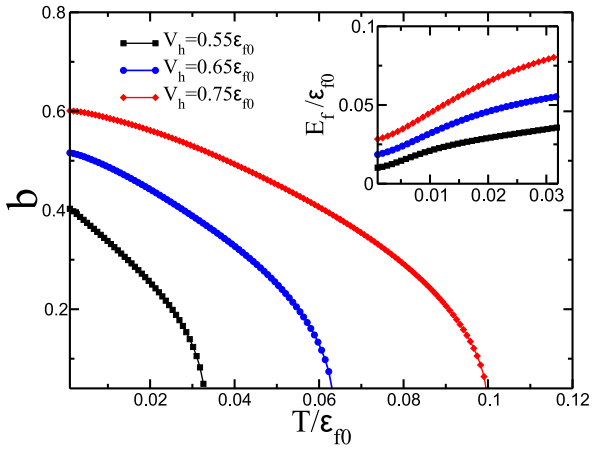

Figure 4.3: Temperature dependence of the hybridization gap parameter b and the renormalized f-level position (inset) for various values of the bare hybridization (see Section 4.4.2 for more details).

$n_d + n_f = 4$. This condition guarantees that four out of eight doubly degenerate bands will be fully occupied. The details of our mean-field calculation are given in the technical Section 4.4.2. Here we provide the final results of our calculations.

In Fig. 4.3 we show that the magnitude b reduces with temperature, corresponding to a gradual rise in the Sm valence, due to the weaker renormalization of the f-electron level. The degree of mixed valence of Sm^+ is given then by $v = 3 - \langle n_f \rangle$. In our simplified mean-field calculation, the smooth temperature cross-over from Kondo insulating behavior to local moment metal at high temperatures is crudely approximated by an abrupt second-order phase transition.

Fig. 4.4 shows the computed band structure for the cubic Kondo insulator obtained from mean-field theory, showing the band inversion between the d- and f-bands at the X points that generates the strong topological insulator. Moreover, as the value of the bare hybridization increases, there is a maximum value beyond which the bands no longer invert and the Kondo insulator becomes a conventional band insulator.

One of the interesting questions raised by this work concerns the many body character of the Dirac electrons on the surface. Like the low-lying excitations in the valence and conduction band, the surface states of a TKI involve heavy quasiparticles of predominantly f-character. The characteristic Fermi velocity of these excitations $v_F^* = Zv_F$ is renormalized

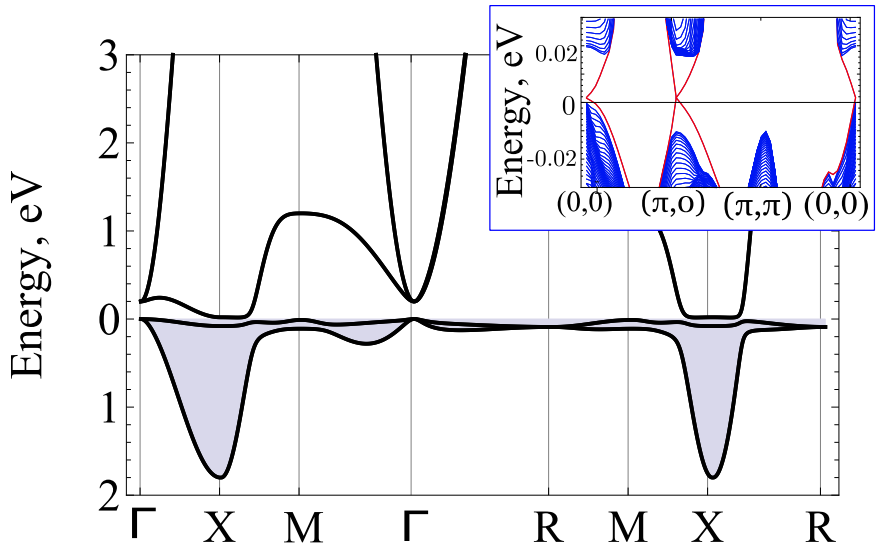

Figure 4.4: Band structure consistent with PES and LDA studies of SmB_6 computed with the following parameters: $n_f = 0.48$ (or $b = 0.73$), $V = 0.05$ eV,$t_d = 2$ eV, $\mu_d = 0.2$ eV , $\eta = \eta' = -.3$, $\epsilon_f = -0.01$ eV ($\epsilon_{f0} = -0.17$ eV), $t_f = -.05$ eV, $T = 10^{-4}$ eV and the gap is $\Delta = 12$ meV. Shaded region denotes filled bands. Inset shows the ground-state energy computed for a slab of 80 layers to illustrate the three gapless surface Dirac excitations at the symmetry points $\hat{\Gamma}, \hat{X}' and \hat{X}''$.

with respect to the conduction electron band group velocities, where $Z = m/m^*$ is the mass renormalization of the f-electrons. In a band topological insulator, the penetration depth of the surface states $\xi \sim v_F/\Delta$, where Δ is the band-gap, scale that is significantly larger than a unit-cell size. Paradoxically, even though the Fermi velocity of the Dirac cones in a TKI is very low, we expect the characteristic penetration depth ξ of the heavy wavefunctions into the bulk to be of order the lattice spacing a. To see this, we note that $\xi \sim \frac{v_F^*}{\Delta_g}$, where the indirect gap of the Kondo insulator Δ_g is of order the Kondo temperature $\Delta_g \sim T_K$. But since $T_K \sim ZW$, where W is the width of the conduction electron band, this implies that the penetration depth of the surface excitations $\xi \sim v_F/W \sim a$ is given by the size a of the unit cell. Physically, we can interpret the surface Dirac cones as a result of broken Kondo singlets, whose spatial extent is of order a lattice spacing. This feature is likely to make the surface states rather robust against the purity of the bulk.

Various interesting questions are raised by our study. Conventional Kondo insulators are most naturally understood as a in the strong-coupling limit of the Kondo lattice, where local singlets form between a commensurate number of conduction electrons and localized

moments. What then is the appropriate strong coupling description of topological Kondo insulators, and can we understand the surface states in terms of broken Kondo singlets? A second question concerns the temperature dependence of the hybridization gap. Experimentally, the hybridization gap observed in Raman and transport studies [106, 110] is seen to develop in a fashion strongly reminiscent of the mean-field theory. Could this close resemblance to the mean-field theory indicate that fluctuations about mean-field theory are weaker in a fully gapped Kondo lattice than in its metallic counterpart?

To summarize, we have studied the cubic topological Kondo insulator, incorporating the effect of a fourfold degenerate f-multiplet. There are two main effects of the quartet states: first, that the quarter filling of the quartet allows the fractional filling of the band favorable to strong topological insulating behavior to occur in the almost integral valent environment of the Kondo insulator. The second effect is to double the degeneracy of the band-states at the high-symmetry Γ and R points in the Brillouin zone, so that their net parity is always positive, effectively removing these points from the calculation of the Z_2 topological invariant so that the only important crossing must take place at the X or M points. For the cubic topological Kondo insulators, this immediately leads to a prediction that three heavy Dirac cones will form on the surfaces [97, 100].

We would like to thank A. Ramires, V. Galitski, K. Sun, S. Artyukhin and J. P. Paglione for stimulating discussions related to this work. This work was supported by the Ohio Board of Regents Research Incentive Program grant OBR-RIP-220573 (M.D.), DOE grant DE-FG02-99ER45790 (V. A & P. C.), the U.S. National Science Foundation I2CAM International Materials Institute Award, Grant DMR-0844115.

Note added in proof: After the submission of this paper, several groups [111, 112, 113] have reported angular-resolved photoemission spectroscopy (ARPES) results that support the presence of surface states predicted by this, and earlier papers [97, 100]. In addition, torque magnetometry measurements [114] have observed de-Haas van Alphen oscillations associated with the surface states of SmB_6 that are consistent with a two dimensional Dirac spectrum. The masses of the excitations seen in both sets of experiments are however, significantly smaller than expected in the current theory. Lastly, experimental observations of weak-antilocalization signatures in conductivity [115] as well as induced-localization of

the metallic surface states with an addition of magnetic impurities [116] provide strong circumstantial evidence that the the surface quasiparticles are spin-polarized, as expected in a topological insulator.

4.4 Some additional details on the mean field

- details of the derivation of the tight-binding Hamiltonian for a cubic Kondo insulator.
- derivation of the mean-field theory for the infinite U limit
- derivation of the mean-field equations.

4.4.1 Rotation matrices

To construct the Hamiltonian, we evaluate the hopping matrices along the z-axis, and then carry out a unitary transformation to evaluate the corresponding quantities for hopping along the x and y axes.

Consider a general rotation operator

$$\mathcal{R} = R\Lambda, \tag{4.7}$$

where R and Λ describe rotations about a principle axis of the crystal in real and spin space respectively. The Hamiltonian in a cubic environment is invariant under these transformations: $H = \mathcal{R}H\mathcal{R}^\dagger$. We now write the directional dependence of the Hamiltonian explicitly. Consider a tight-binding Hamiltonian of the form

$$\hat{H} = \sum_{\mathbf{X},\mathbf{r}\in\{\pm\hat{\mathbf{x}},\pm\hat{\mathbf{y}},\pm\hat{\mathbf{z}}\}} \Psi^\dagger(\mathbf{X}+\mathbf{r})h(\mathbf{r})\Psi(\mathbf{X}) \tag{4.8}$$

where $\mathbf{X}$ are the positions of atoms and $\mathbf{r}$ the relative positions. Under a rotation, the fields transform as

$$\Psi^\dagger(\mathbf{X}) \to \Psi^\dagger(R\mathbf{x})\Lambda \tag{4.9}$$

so that the Hamiltonian transforms as follows,

$$\hat{H} \quad \to \quad \sum_{\mathbf{X},\mathbf{r}\in\{\pm\hat{\mathbf{x}},\pm\hat{\mathbf{y}},\pm\hat{\mathbf{z}}\}} \Psi^\dagger(R(\mathbf{X}+\mathbf{r}))\Lambda h(\mathbf{r})\Lambda^\dagger\Psi(R\mathbf{X})$$

$$= \sum_{\mathbf{X},\mathbf{r}\in\{\pm\hat{\mathbf{x}},\pm\hat{\mathbf{y}},\pm\hat{\mathbf{z}}\}} \Psi^\dagger(\mathbf{X}+\mathbf{r})\Lambda h(R^{-1}\mathbf{r})\Lambda^\dagger\Psi(\mathbf{X}) = H, \tag{4.10}$$

from which we deduce that the tight-binding matrix elements satisfy

$$h(R\mathbf{r}) = \Lambda h(\mathbf{r})\Lambda^\dagger, \tag{4.11}$$

Now we employ a right-handed rotation $\mathcal{R}$ around the (1,1,1) direction through angle $2\pi/3$, which cyclically rotates the unit vectors as follows: $\hat{x} \to \hat{y} \to \hat{z} \to \hat{x}$, so that $\hat{x} = R\hat{z}$ and $\hat{y} = R^{-1}\hat{z}$. It follows that the hopping matrix elements along the $\hat{\mathbf{x}}$ and $\hat{\mathbf{y}}$ directions can be determined as follows

$$h(\hat{\mathbf{x}}) = \Lambda h(\hat{\mathbf{z}})\Lambda^\dagger, \qquad h(\hat{\mathbf{y}}) = \Lambda^\dagger h(\hat{\mathbf{z}})\Lambda. \tag{4.12}$$

In the above expression, the rotation in the counter-clockwise direction R^{-1} is accomplished by noting that $\Lambda^{-1} = \Lambda^\dagger$. Provided we are dealing with simply nearest neighbor hopping, then in momentum space, the 3D tight-binding Hamiltonian must take the following form

$$H_{3D}(\mathbf{k}) \equiv H_{3D}(k_x, k_y, k_z) = \mathcal{H}_{1D}(k_z) + \Lambda\mathcal{H}_{1D}(k_x)\Lambda^\dagger + \Lambda^\dagger\mathcal{H}_{1D}(k_y)\Lambda, \tag{4.13}$$

where

$$\mathcal{H}_{1D}(k_z) = h(\hat{\mathbf{z}})e^{-ik_z} + h(-\hat{\mathbf{z}})e^{ik_z} \tag{4.14}$$

is the one-dimensional tight-binding Hamiltonian for hopping along the z-axis. To proceed further we need an explicit form of Λ,

$$\Lambda = e^{-i\alpha J_z}e^{-i\beta J_y}e^{-i\gamma J_z}. \tag{4.15}$$

Here, the rotation operator Λ is written in the "ZYZ" convention, corresponding to a rotation around the z-axis, followed by a rotation around the y-axis, and then the new z-axis. The matrix elements of this operator are given by Wigner D-functions

$$\begin{aligned} D^j_{m'm} &= \langle jm'|\Lambda|jm\rangle = e^{-im'\alpha - im\gamma}d(j,m',m,\beta). \\ d(j,m',m,\beta) &= \textstyle\sum_k (-1)^{k+m'-m}\frac{\sqrt{(j+m)!(j-m)!(j+m')!(j-m')!}}{(j-m'-k)!(j+m-k)!(k+m'-m)!k!} \\ &\quad \left(\cos\tfrac{\beta}{2}\right)^{2j+m-m'-2k}\left(\sin\tfrac{\beta}{2}\right)^{m'-m+2k} \end{aligned}$$

For $J = 5/2$ we obtain $\Lambda^{(j=5/2)} = D^{5/2}_{mm'}(0,\pi/2,\pi/2)$, and for d-states $(L,s) = (2,\frac{1}{2})$, $\Lambda^{(j=2)} = D^2_{mm'} \otimes D^{1/2}_{mm'}(0,\pi/2,\pi/2)$. One can now obtain the transformation matrices for

a given multiplet (e_g, t_{2g}, Γ_8 etc) by taking inner product $M_{ij} = \langle i|\Lambda_x|j\rangle$. For example e_g multiplet $|j\rangle = |e_g : m\rangle \equiv \left\{|d_{x^2-y^2}\uparrow\rangle, |d_{x^2-y^2}\downarrow\rangle, |d_{z^2}\uparrow\rangle, |d_{z^2}\downarrow\rangle\right\}$

$$M^d_{nm} = \langle e_g : n|\Lambda|e_g : m\rangle. \tag{4.16}$$

Similarly for the Γ_8 quartet. In the end of the day the rotation is performed by the same matrix M_{mn}. This is due to the similar symmetry of Γ_8 and e_g,

$$M^d_{mn} = M^f_{mn} = e^{\frac{-i\pi}{4}} \frac{1}{2\sqrt{2}} \begin{pmatrix} -1 & -i & \sqrt{3} & i\sqrt{3} \\ 1 & -i & -\sqrt{3} & i\sqrt{3} \\ -\sqrt{3} & -i\sqrt{3} & -1 & -i \\ \sqrt{3} & -i\sqrt{3} & 1 & -i \end{pmatrix}. \tag{4.17}$$

Note that the rotation cyclically exchanges $x \to y \to z \to x$, thus applying it three times gives overall "-1" due to fermionic statistics.

$$\Lambda = \begin{pmatrix} M_{mn} & \\ & M_{mn} \end{pmatrix} \quad \text{and} \quad \Lambda^3 = -1. \tag{4.18}$$

Now , we can use (4.18) in (4.13) to derive the Hamiltonian defined in *(5)* and *(6)* of the main paper. The tight-binding matrix element for hopping along the z-axis is given by

$$H_{1D}(k) = \begin{pmatrix} \mathcal{H}^d_{1D}(k) & V_{1D}(k) \\ V_{1D}(k) & \mathcal{H}^f_{1D}(k) \end{pmatrix} \tag{4.19}$$

$$\mathcal{H}^l_{1D}(k) = \begin{pmatrix} 2t^l \cos k + \frac{\epsilon^l}{3} & \\ & \eta_l 2t^l \cos k + \frac{\epsilon^l}{3} \end{pmatrix}, \qquad (l = d, f) \tag{4.20}$$

$$V_{1D}(k) = V \begin{pmatrix} 0 & \\ & \sigma_z \end{pmatrix} \sin k \tag{4.21}$$

where the ϵ^l are the bare energies of the isolated d and f-quartets, and the factor of $1/3$ is chosen so that when we sum over 1D Hamiltonians in the x, y and z directions we get ϵ^l. Notice also the odd-parity in the hybridization.

Carrying out the Unitary transformations on the hybridization, we obtain where we have introduced the short-hand $\bar{\sigma}_\alpha = \sigma_\alpha \sin k_\alpha$, so that $\bar{\sigma}_z \equiv \sigma_z \sin k_z$ The rotation to the x

and y-axis then gives

$$M^\dagger V_{1D}(k_x) M = \frac{V}{4} \begin{pmatrix} -3\bar{\sigma}_x & \sqrt{3}\bar{\sigma}_x \\ \sqrt{3}\bar{\sigma}_x & -\bar{\sigma}_x \end{pmatrix}, \tag{4.22}$$

$$M V_{1D}(k_y) M^\dagger = \frac{V}{4} \begin{pmatrix} -3\bar{\sigma}_y & -\sqrt{3}\bar{\sigma}_y \\ -\sqrt{3}\bar{\sigma}_y & -\bar{\sigma}_y \end{pmatrix}. \tag{4.23}$$

so that

$$V_{3D}(\mathbf{k}) = V_{1D}(k_z) + M^\dagger V_{1D}(k_x) M + M V_{1D}(k_y) M^\dagger = \tag{4.24}$$

$$= \frac{V}{4} \begin{pmatrix} -3(\bar{\sigma}_y + \bar{\sigma}_x) & \sqrt{3}(\bar{\sigma}_x - \bar{\sigma}_y) \\ \sqrt{3}(\bar{\sigma}_x - \bar{\sigma}_y) & -(\bar{\sigma}_y + \bar{\sigma}_x) + 4\bar{\sigma}_z \end{pmatrix} \tag{4.25}$$

and similarly,

$$\mathcal{H}^l_{3D}(\mathbf{k}) = \mathcal{H}^l_{1D}(k_z) + M^\dagger \mathcal{H}^l_{1D}(k_x) M + M \mathcal{H}^l_{1D}(k_y) M^\dagger = \tag{4.26}$$

$$= \frac{t^l}{2} \begin{pmatrix} \phi_1(\mathbf{k}) + \eta_l \phi_2(\mathbf{k}) & (1-\eta_l)\phi_3(\mathbf{k}) \\ (1-\eta_l)\phi_3(\mathbf{k}) & \phi_2(\mathbf{k}) + \eta_l \phi_1(\mathbf{k}) \end{pmatrix} + \epsilon^l, \tag{4.27}$$

with $\phi_1(\mathbf{k}) = c_x + c_y + 4c_z$, $\phi_2(\mathbf{k}) = 3(c_x + c_y)$ and $\phi_3(\mathbf{k}) = \sqrt{3}(c_x - c_y)$ ($c_\alpha = \cos k_\alpha, \alpha = x, y, z$).

4.4.2 Details of the mean-field theory

The full Hamiltonian for the problem also contains a term describing the local Hubbard interaction between the f-electrons:

$$H_f = U \sum_i \sum_{\alpha=1}^{4} \sum_{\beta \neq \alpha} f^\dagger_{i\alpha} f_{i\alpha} f^\dagger_{i\beta} f_{i\beta} \tag{4.28}$$

Consider the limit $U \to \infty$. In this limit we can project out all states with occupation number larger than one by replacing the bare f-electron fields by Hubbard operators, which we represent using a slave boson representation, as follows:

$$f^\dagger_{i\alpha} \to X_{\alpha 0}(i) = f^\dagger_{i\alpha} b_i, \quad f_{i\alpha} \to X_{0\alpha}(i) = b^\dagger_i f_{i\alpha}, \tag{4.29}$$

supplemented by a constraint of no more than one f-electron per each site ($U = \infty$):

$$\sum_{\alpha=1}^{4} f^\dagger_{i\alpha} f_{i\alpha} + b^\dagger_i b_i = 1. \tag{4.30}$$

The partition function corresponding to the model Hamiltonian $H = H_c + H_f + H_{hyb}$ above and with constraint condition (4.30) reads :

$$Z = \int_{-\pi/\beta}^{\pi/\beta} \frac{\beta d\lambda}{\pi} \int \mathcal{D}(b, b^\dagger, f, f^\dagger, c, c^\dagger) \exp\left(- \int_0^\beta L(\tau) d\tau \right), \tag{4.31}$$

where Lagrangian $L(\tau)$ is

$$\begin{aligned} L = & \sum_i b_i^\dagger \frac{d}{d\tau} b_i + \sum_{ij} \sum_{\alpha,\beta=1}^{4} f_{i\alpha}^\dagger \left[\delta_{ij}\delta_{\alpha\beta} \left(\frac{d}{d\tau} + \varepsilon_f \right) + b_i t_{ij,\alpha\beta}^{(f)} b_j^\dagger \right] f_{j\beta} \\ & + \sum_{\mathbf{k}\sigma} \sum_{a,b=1}^{2} c_{a\mathbf{k}\sigma}^\dagger \left(\frac{d}{d\tau} + \varepsilon_{ab}^{(d)}(\mathbf{k}) \right) c_{b\mathbf{k}\sigma} \\ & + \frac{1}{2} \sum_{\langle ij \rangle} \sum_{\mathbf{k}\sigma} \sum_{a=1}^{2} \sum_{\beta=1}^{4} \left(V_{ia\sigma,j\beta} c_{ai\sigma}^\dagger b_i^\dagger f_{j\alpha} + \text{h.c.} \right) + \sum_j i\lambda_j \left(\sum_{\alpha=1}^{4} f_{j\alpha}^\dagger f_{j\alpha} + b_j^\dagger b_j - 1 \right) \end{aligned} \tag{4.32}$$

Mean-field (saddle-point) approximation corresponds to the following values of the bosonic fields:

$$b_{\mathbf{q}}(\tau) = b\delta_{\mathbf{q},0}, \quad i\lambda_{\mathbf{q}}(\tau) = (E_f - \varepsilon_f)\delta_{\mathbf{q},0}, \tag{4.33}$$

where both a and ε_f are τ-independent. In the mean-field theory we choose a "radial" gauge where the the phase of the b-field has been absorbed into the f-electron fields. Also, for an insulator, we need a filled quartet of states at each site, so that

$$n_c + n_f = 4. \tag{4.34}$$

Note, the parameter b also renormalizes the f-hopping elements. Indeed, it follows that when $i \neq j$, $f_{i\alpha}^\dagger f_{j\beta} \to X_{\alpha 0}(i) X_{0\beta}(j) = f_{i\alpha}^\dagger b_i b_j^\dagger f_{j\beta}$. However, the on site occupancy is unrenormalized by the slave boson fields, since in the infinite U limit, the on site occupancy $X_{\alpha\alpha}(i) = f_{i\alpha}^\dagger f_{i\alpha}$.

The first three terms together with the last term in the Lagrangian (4.32) can be written using the new fermionic basis and (4.33). It follows:

$$\begin{aligned} L_0(\tau) = (b^2 - 1)(E_f - \varepsilon_f) + & \sum_{\mathbf{k}\alpha} \sum_{n=1}^{2} \tilde{f}_{n\mathbf{k}\alpha}^\dagger \left(\frac{d}{d\tau} + E_{n\mathbf{k}}^{(f)} \right) \tilde{f}_{n\mathbf{k}\alpha} + \\ & + \sum_{\mathbf{k}\sigma} \sum_{a=1}^{2} d_{a\mathbf{k}\sigma}^\dagger \left(\frac{d}{d\tau} + E_{a\mathbf{k}}^{(d)} \right) d_{a\mathbf{k}\sigma} \end{aligned} \tag{4.35}$$

where the renormalized f-electron dispersion is

$$E^{(f)}_{n\mathbf{k}} = E_f + 2t_f b^2 \left(c_x + c_y + c_z + (-1)^n \sqrt{c_x^2 + c_y^2 + c_z^2 - c_x c_y - c_y c_z - c_z c_x} \right), \quad n = 1, 2. \tag{4.36}$$

Correspondingly, the hybridization matrix in the new fermionic basis can be obtained via unitary transformation with the matrix

$$\mathcal{U}_{\mathbf{k}} = \begin{pmatrix} u_{\mathbf{k}} & 0 & v_{\mathbf{k}} & 0 \\ 0 & u_{\mathbf{k}} & 0 & v_{\mathbf{k}} \\ -v_{\mathbf{k}} & 0 & u_{\mathbf{k}} & 0 \\ 0 & -v_{\mathbf{k}} & 0 & u_{\mathbf{k}} \end{pmatrix}, \quad \mathcal{U}^{-1}_{\mathbf{k}} = \begin{pmatrix} u_{\mathbf{k}} & 0 & -v_{\mathbf{k}} & 0 \\ 0 & u_{\mathbf{k}} & 0 & -v_{\mathbf{k}} \\ v_{\mathbf{k}} & 0 & u_{\mathbf{k}} & 0 \\ 0 & v_{\mathbf{k}} & 0 & u_{\mathbf{k}} \end{pmatrix} \tag{4.37}$$

Thus we need to calculate the elements of the matrix

$$\widetilde{H}_V = iV_{df} \frac{b}{2} \sum_{\mathbf{k}} \hat{d}^{\dagger}_{\mathbf{k}} \mathcal{U}^{-1}_{\mathbf{k}} H_{hyb}(\mathbf{k}) \mathcal{U}_{\mathbf{k}} \tilde{f}_{\mathbf{k}} + \text{h.c.} \tag{4.38}$$

We can use the following relations

$$u^2_{\mathbf{k}} - v^2_{\mathbf{k}} = \frac{c_x + c_y - 2c_z}{2R_{\mathbf{k}}}, \quad u_{\mathbf{k}} v_{\mathbf{k}} = \frac{\sqrt{3}}{4R_{\mathbf{k}}}(c_x - c_y). \tag{4.39}$$

In our subsequent discussion it will be convenient to write $\widetilde{H}_V(\mathbf{k})$ in a more compact form. To derive the corresponding expression we first recall that H_{hyb} can be written as follows

$$\begin{aligned} H_{hyb}(\mathbf{k}) &= iV_{df} \frac{b}{2} \left[\hat{\phi}^x(\mathbf{k}) \otimes \hat{\sigma}_x + \hat{\phi}^y(\mathbf{k}) \otimes \hat{\sigma}_y + \hat{\phi}^z(\mathbf{k}) \otimes \hat{\sigma}_z \right], \quad \hat{\phi}_\alpha = \phi_0^\alpha \hat{\tau}_0 + \phi_1^\alpha \hat{\tau}_z + \phi_2^\alpha \hat{\tau}_x, \\ \vec{\phi}_0 &= \frac{2}{3}(\sin k_x, -\sin k_y, \sin k_z), \quad \vec{\phi}_1 = \frac{1}{3}(\sin k_x, -\sin k_y, -2\sin k_z), \\ \vec{\phi}_2 &= +\frac{1}{\sqrt{3}}(\sin k_x, \sin k_y, 0). \end{aligned} \tag{4.40}$$

Again, note the change from minus sign to plus sign in front of $\vec{\phi}_2$ term. This yields the agreement with the hybridization Hamiltonian obtained from the rotations method. We also have

$$\hat{\mathcal{U}}_{\mathbf{k}} = u_{\mathbf{k}} \hat{\tau}_0 \otimes \hat{\sigma}_0 + i v_{\mathbf{k}} \hat{\tau}_y \otimes \hat{\sigma}_0, \quad \hat{\mathcal{U}}^{-1}_{\mathbf{k}} = u_{\mathbf{k}} \hat{\tau}_0 \otimes \hat{\sigma}_0 - i v_{\mathbf{k}} \hat{\tau}_y \otimes \hat{\sigma}_0, \tag{4.41}$$

After some algebra I find

$$\begin{aligned} &\hat{\mathcal{U}}^{-1}_{\mathbf{k}} (\hat{\tau}_0 \otimes \hat{\sigma}_x) \hat{\mathcal{U}}_{\mathbf{k}} = \hat{\tau}_0 \otimes \hat{\sigma}_x, \\ &\hat{\mathcal{U}}^{-1}_{\mathbf{k}} (\hat{\tau}_z \otimes \hat{\sigma}_x) \hat{\mathcal{U}}_{\mathbf{k}} = (u^2_{\mathbf{k}} - v^2_{\mathbf{k}})(\hat{\tau}_z \otimes \hat{\sigma}_x) + 2u_{\mathbf{k}} v_{\mathbf{k}} (\hat{\tau}_x \otimes \hat{\sigma}_x), \\ &\hat{\mathcal{U}}^{-1}_{\mathbf{k}} (\hat{\tau}_x \otimes \hat{\sigma}_x) \hat{\mathcal{U}}_{\mathbf{k}} = (u^2_{\mathbf{k}} - v^2_{\mathbf{k}})(\hat{\tau}_x \otimes \hat{\sigma}_x) - 2u_{\mathbf{k}} v_{\mathbf{k}} (\hat{\tau}_z \otimes \hat{\sigma}_x). \end{aligned} \tag{4.42}$$

These results become much more transparent if we express $u_{\mathbf{k}}$ and $v_{\mathbf{k}}$ in terms of the angle $\theta_{\mathbf{k}}$:

$$u_{\mathbf{k}} = \cos(\theta_{\mathbf{k}}/2), \quad v_{\mathbf{k}} = \sin(\theta_{\mathbf{k}}/2). \tag{4.43}$$

Then we see that

$$\hat{\mathcal{U}}_{\mathbf{k}}^{-1}\left(\hat{\phi}^x(\mathbf{k})\otimes\hat{\sigma}_x\right)\hat{\mathcal{U}}_{\mathbf{k}} = \hat{\Phi}^x(\mathbf{k})\otimes\hat{\sigma}_x, \tag{4.44}$$

where now

$$\hat{\Phi}^x = \Phi_0^x\hat{\tau}_0 + \Phi_1^x\hat{\tau}_z + \Phi_2^x\hat{\tau}_x, \quad \Phi_0^x = \phi_0^x, \quad \begin{pmatrix}\Phi_1^x\\ \Phi_2^x\end{pmatrix} = \begin{bmatrix}\cos\theta_{\mathbf{k}} & -\sin\theta_{\mathbf{k}}\\ \sin\theta_{\mathbf{k}} & \cos\theta_{\mathbf{k}}\end{bmatrix}\begin{pmatrix}\phi_1^x\\ \phi_2^x\end{pmatrix} \tag{4.45}$$

Similarly, we find

$$\begin{aligned}
&\hat{\mathcal{U}}_{\mathbf{k}}^{-1}\left(\hat{\phi}^y(\mathbf{k})\otimes\hat{\sigma}_y\right)\hat{\mathcal{U}}_{\mathbf{k}} = \hat{\Phi}^y(\mathbf{k})\otimes\hat{\sigma}_y, \quad \hat{\mathcal{U}}_{\mathbf{k}}^{-1}\left(\hat{\phi}^z(\mathbf{k})\otimes\hat{\sigma}_z\right)\hat{\mathcal{U}}_{\mathbf{k}} = \hat{\Phi}^z(\mathbf{k})\otimes\hat{\sigma}_z,\\
&\hat{\Phi}^y = \Phi_0^y\hat{\tau}_0 + \Phi_1^y\hat{\tau}_z + \Phi_2^y\hat{\tau}_x, \quad \Phi_0^y = \phi_0^y, \quad \begin{pmatrix}\Phi_1^y\\ \Phi_2^y\end{pmatrix} = \begin{bmatrix}\cos\theta_{\mathbf{k}} & \sin\theta_{\mathbf{k}}\\ -\sin\theta_{\mathbf{k}} & \cos\theta_{\mathbf{k}}\end{bmatrix}\begin{pmatrix}\phi_1^y\\ \phi_2^y\end{pmatrix},\\
&\hat{\Phi}^z = \Phi_0^z\hat{\tau}_0 + \Phi_1^z\hat{\tau}_z + \Phi_2^z\hat{\tau}_x, \quad \Phi_0^z = \phi_0^z, \quad \begin{pmatrix}\Phi_1^z\\ \Phi_2^z\end{pmatrix} = \begin{bmatrix}\cos\theta_{\mathbf{k}} & -\sin\theta_{\mathbf{k}}\\ \sin\theta_{\mathbf{k}} & \cos\theta_{\mathbf{k}}\end{bmatrix}\begin{pmatrix}\phi_1^z\\ \phi_2^z\end{pmatrix}.
\end{aligned} \tag{4.46}$$

Thus, we can re-write (4.38) as follows

$$\widetilde{H}_V = iV_{df}\frac{b}{2}\sum_{\mathbf{k}}\hat{d}_{\mathbf{k}\alpha}^{\dagger}[\hat{\Phi}_{\mathbf{k}}]_{\alpha\beta}\tilde{f}_{\mathbf{k}\beta} + \text{h.c.}, \quad \hat{\Phi}_{\mathbf{k}} = \hat{\Phi}^x(\mathbf{k})\otimes\hat{\sigma}_x + \hat{\Phi}^y(\mathbf{k})\otimes\hat{\sigma}_y + \hat{\Phi}^z(\mathbf{k})\otimes\hat{\sigma}_z \tag{4.47}$$

Next we derive the mean-field equations.

4.4.3 Derivation of the mean-field equations

To derive the mean field equations we first integrate out d-electrons by making the following change of variables in the path integral:

$$\begin{aligned}
&\hat{d}_{\mathbf{k}}^{\dagger} \to \hat{d}_{\mathbf{k}}^{\dagger} + \hat{f}_{\mathbf{k}}^{\dagger}\hat{\Phi}_{\mathbf{k}}^{\dagger}\hat{G}_d(i\omega,\mathbf{k}), \quad \hat{d}_{\mathbf{k}} \to \hat{d}_{\mathbf{k}} + \hat{G}_d(i\omega,\mathbf{k})\hat{\Phi}_{\mathbf{k}}\hat{f}_{\mathbf{k}},\\
&\hat{G}_d^{-1}(i\omega,\mathbf{k}) = \begin{pmatrix} i\omega - E_{1\mathbf{k}}^{(d)} & 0 & 0 & 0\\ 0 & i\omega - E_{1\mathbf{k}}^{(d)} & 0 & 0\\ 0 & 0 & i\omega - E_{2\mathbf{k}}^{(d)} & 0\\ 0 & 0 & 0 & i\omega - E_{2\mathbf{k}}^{(d)}\end{pmatrix}
\end{aligned} \tag{4.48}$$

Then the resulting action is Gaussian and the f-electrons can be integrated out. This yield the effective action of the form

$$S_{eff} = (b^2-1)(E_f - \varepsilon_f) - T\sum_{i\omega}\sum_{\mathbf{k}} \log\det\left[\hat{G}_{ff}^{-1}(i\omega,\mathbf{k})\right], \tag{4.49}$$

$$\hat{G}_{ff}^{-1} = \hat{G}_{f}^{-1}(i\omega,\mathbf{k}) - (V_{df}\frac{b}{2})^2 \hat{\Phi}_{\mathbf{k}}^{\dagger}\hat{G}_{d}(i\omega,\mathbf{k})\hat{\Phi}_{\mathbf{k}} \tag{4.50}$$

The renormalized f-electron correlation function $\hat{G}_{ff}^{-1}$ has a block diagonal form:

$$\hat{G}_{ff}^{-1} = \frac{(V_{df}b)^2}{4}\times \tag{4.51}$$
$$\begin{pmatrix}
\mathcal{G}_{1f}^{-1}(i\omega,\mathbf{k})\frac{4}{(V_{df}b)^2} & 0 & -\frac{\Delta_{1\mathbf{k}}}{i\omega-E_{1\mathbf{k}}^{(d)}} - \frac{\Delta_{2\mathbf{k}}}{i\omega-E_{2\mathbf{k}}^{(d)}} & -\frac{\widetilde{\Delta}_{1\mathbf{k}}}{i\omega-E_{1\mathbf{k}}^{(d)}} - \frac{\widetilde{\Delta}_{2\mathbf{k}}}{i\omega-E_{2\mathbf{k}}^{(d)}} \\
0 & \mathcal{G}_{1f}^{-1}(i\omega,\mathbf{k})\frac{4}{(V_{df}b)^2} & \frac{\widetilde{\Delta}_{1\mathbf{k}}^{*}}{i\omega-E_{1\mathbf{k}}^{(d)}} + \frac{\widetilde{\Delta}_{2\mathbf{k}}^{*}}{i\omega-E_{2\mathbf{k}}^{(d)}} & -\frac{\Delta_{1\mathbf{k}}^{*}}{i\omega-E_{1\mathbf{k}}^{(d)}} - \frac{\Delta_{2\mathbf{k}}^{*}}{i\omega-E_{2\mathbf{k}}^{(d)}} \\
-\frac{\Delta_{1\mathbf{k}}^{*}}{i\omega-E_{1\mathbf{k}}^{(d)}} - \frac{\Delta_{2\mathbf{k}}^{*}}{i\omega-E_{2\mathbf{k}}^{(d)}} & \frac{\widetilde{\Delta}_{1\mathbf{k}}}{i\omega-E_{1\mathbf{k}}^{(d)}} + \frac{\widetilde{\Delta}_{2\mathbf{k}}}{i\omega-E_{2\mathbf{k}}^{(d)}} & \mathcal{G}_{2f}^{-1}(i\omega,\mathbf{k})\frac{4}{(V_{df}b)^2} & 0 \\
-\frac{\widetilde{\Delta}_{1\mathbf{k}}^{*}}{i\omega-E_{1\mathbf{k}}^{(d)}} - \frac{\widetilde{\Delta}_{2\mathbf{k}}^{*}}{i\omega-E_{2\mathbf{k}}^{(d)}} & -\frac{\Delta_{1\mathbf{k}}}{i\omega-E_{1\mathbf{k}}^{(d)}} - \frac{\Delta_{2\mathbf{k}}}{i\omega-E_{2\mathbf{k}}^{(d)}} & 0 & \mathcal{G}_{2f}^{-1}(i\omega,\mathbf{k})\frac{4}{(V_{df}b)^2}
\end{pmatrix},$$

where the diagonal elements are given by

$$\begin{aligned}
\mathcal{G}_{1f}^{-1}(i\omega,\mathbf{k}) &= i\omega - E_{1\mathbf{k}}^{(f)} - (V_{df}\frac{b}{2})^2\left[\frac{\Phi_{1\mathbf{k}}^{(+)}}{i\omega-E_{1\mathbf{k}}^{(d)}} + \frac{\Phi_{2\mathbf{k}}}{i\omega-E_{2\mathbf{k}}^{(d)}}\right], \\
\mathcal{G}_{2f}^{-1}(i\omega,\mathbf{k}) &= i\omega - E_{2\mathbf{k}}^{(f)} - (V_{df}\frac{b}{2})^2\left[\frac{\Phi_{2\mathbf{k}}}{i\omega-E_{1\mathbf{k}}^{(d)}} + \frac{\Phi_{1\mathbf{k}}^{(-)}}{i\omega-E_{2\mathbf{k}}^{(d)}}\right]
\end{aligned} \tag{4.52}$$

and we have introduced the following functions

$$\begin{aligned}
&\Phi_{1\mathbf{k}}^{(\pm)} = (\Phi_0^x \pm \Phi_1^x)^2 + (\Phi_0^y \pm \Phi_1^y)^2 + (\Phi_0^z \pm \Phi_1^z)^2, \quad \Phi_{2\mathbf{k}} = (\Phi_2^x)^2 + (\Phi_2^y)^2 + (\Phi_2^z)^2, \\
&\Delta_{1\mathbf{k}} = \Phi_2^z(\Phi_0^z + \Phi_1^z) + (\Phi_2^x + i\Phi_2^y)[\Phi_0^x + \Phi_1^x - i(\Phi_0^y + \Phi_1^y)], \\
&\Delta_{2\mathbf{k}} = \Phi_2^z(\Phi_0^z - \Phi_1^z) + (\Phi_2^x - i\Phi_2^y)[\Phi_0^x - \Phi_1^x + i(\Phi_0^y - \Phi_1^y)], \\
&\widetilde{\Delta}_{1\mathbf{k}} = (\Phi_2^x - i\Phi_2^y)(\Phi_0^z + \Phi_1^z) - \Phi_2^z[\Phi_0^x + \Phi_1^x - i(\Phi_0^y + \Phi_1^y)], \\
&\widetilde{\Delta}_{2\mathbf{k}} = \Phi_2^z[\Phi_0^x - \Phi_1^x - i(\Phi_0^y - \Phi_1^y)] - (\Phi_2^x - i\Phi_2^y)(\Phi_0^z - \Phi_1^z)
\end{aligned} \tag{4.53}$$

Then the determinant of the matrix $\hat{G}_{ff}$ is

$$\begin{aligned}
\det\left[\hat{G}_{ff}^{-1}(i\omega,\mathbf{k})\right] = \Big\{ &\mathcal{G}_{1f}^{-1}(i\omega,\mathbf{k})\mathcal{G}_{2f}^{-1}(i\omega,\mathbf{k}) \\
&-(V_{df}\frac{b}{2})^4\left(\frac{\Delta_{1\mathbf{k}}}{i\omega-E_{1\mathbf{k}}^{(d)}} + \frac{\Delta_{2\mathbf{k}}}{i\omega-E_{2\mathbf{k}}^{(d)}}\right)\left(\frac{\Delta_{1\mathbf{k}}^{*}}{i\omega-E_{1\mathbf{k}}^{(d)}} + \frac{\Delta_{2\mathbf{k}}^{*}}{i\omega-E_{2\mathbf{k}}^{(d)}}\right) \\
&-(V_{df}\frac{b}{2})^4\left(\frac{\widetilde{\Delta}_{1\mathbf{k}}}{i\omega-E_{1\mathbf{k}}^{(d)}} + \frac{\widetilde{\Delta}_{2\mathbf{k}}}{i\omega-E_{2\mathbf{k}}^{(d)}}\right)\left(\frac{\widetilde{\Delta}_{1\mathbf{k}}^{*}}{i\omega-E_{1\mathbf{k}}^{(d)}} + \frac{\widetilde{\Delta}_{2\mathbf{k}}^{*}}{i\omega-E_{2\mathbf{k}}^{(d)}}\right)\Big\}^2.
\end{aligned} \tag{4.54}$$

Furthermore, we find that

$$|\Delta_{1\mathbf{k}}|^2+|\widetilde{\Delta}_{1\mathbf{k}}|^2=\Phi_{1\mathbf{k}}^{(+)}\Phi_{2\mathbf{k}},\quad |\Delta_{2\mathbf{k}}|^2+|\widetilde{\Delta}_{2\mathbf{k}}|^2=\Phi_{1\mathbf{k}}^{(-)}\Phi_{2\mathbf{k}} \tag{4.55}$$

so that certain terms in the expression (4.54) will cancel. Therefore, to derive the mean field equation we will need to find a minimum of the following effective action:

$$S_{eff}=(b^2-1)(E_f-\varepsilon_f)-2T\sum_{i\omega}\sum_{\mathbf{k}}\log[P_{4\mathbf{k}}(i\omega;E_f,a)],\quad P_{4\mathbf{k}}(i\omega)=\prod_{i=1}^{4}(i\omega-\varepsilon_{i\mathbf{k}}). \tag{4.56}$$

where we have introduced the polynomial:

$$\begin{aligned}
&P_{4\mathbf{k}}(i\omega)=(i\omega-E_{1\mathbf{k}}^{(f)})(i\omega-E_{2\mathbf{k}}^{(f)})(i\omega-E_{1\mathbf{k}}^{(d)})(i\omega-E_{2\mathbf{k}}^{(d)})+(V_{df}\frac{b}{2})^4\gamma_{\mathbf{k}}^4-\\
&-(V_{df}\frac{b}{2})^2\left\{[\Phi_{2\mathbf{k}}(i\omega-E_{1\mathbf{k}}^{(f)})+\Phi_{1\mathbf{k}}^{+}(i\omega-E_{2\mathbf{k}}^{(f)})](i\omega-E_{2\mathbf{k}}^{(d)})\right\}\\
&-(V_{df}\frac{b}{2})^2\left\{[\Phi_{2\mathbf{k}}(i\omega-E_{2\mathbf{k}}^{(f)})+\Phi_{1\mathbf{k}}^{-}(i\omega-E_{1\mathbf{k}}^{(f)})](i\omega-E_{1\mathbf{k}}^{(d)})\right\},\\
&\gamma_{\mathbf{k}}^4=\Phi_{1\mathbf{k}}^{+}\Phi_{1\mathbf{k}}^{-}+\Phi_{2\mathbf{k}}^2-\Delta_{1\mathbf{k}}\Delta_{2\mathbf{k}}^{*}-\Delta_{1\mathbf{k}}^{*}\Delta_{2\mathbf{k}}-\widetilde{\Delta}_{1\mathbf{k}}\widetilde{\Delta}_{2\mathbf{k}}^{*}-\widetilde{\Delta}_{1\mathbf{k}}^{*}\widetilde{\Delta}_{2\mathbf{k}}.
\end{aligned} \tag{4.57}$$

Thus, two of the three mean field equations are formally given by

$$\frac{\partial S_{eff}}{\partial E_f}=0,\quad \frac{\partial S_{eff}}{\partial a}=0. \tag{4.58}$$

We have

$$b^2-1+2\sum_{i=1}^{4}\sum_{\mathbf{k}}\frac{f(\varepsilon_{i\mathbf{k}})n_F(\varepsilon_{i\mathbf{k}})}{\prod_{l\neq i}(\varepsilon_{i\mathbf{k}}-\varepsilon_{l\mathbf{k}})}=0,\quad n_F(x)=\frac{1}{e^{\beta x}+1}, \tag{4.59}$$

where the function $f(\varepsilon)$ is:

$$\begin{aligned}
f(\lambda)&=2\lambda^3-\lambda^2[2(E_{1\mathbf{k}}^{(d)}+E_{2\mathbf{k}}^{(d)})+E_{1\mathbf{k}}^{(f)}+E_{2\mathbf{k}}^{(f)}]\\
&+\lambda[2E_{1\mathbf{k}}^{(d)}E_{2\mathbf{k}}^{(d)}+(E_{1\mathbf{k}}^{(d)}+E_{2\mathbf{k}}^{(d)})(E_{1\mathbf{k}}^{(f)}+E_{2\mathbf{k}}^{(f)})-(V_{df}\frac{b}{2})^2(\Phi_{1\mathbf{k}}^{+}+\Phi_{1\mathbf{k}}^{-}+2\Phi_{2\mathbf{k}})]\\
&+(V_{df}\frac{b}{2})^2[(\Phi_{2\mathbf{k}}+\Phi_{1\mathbf{k}}^{-})E_{1\mathbf{k}}^{(d)}+(\Phi_{2\mathbf{k}}+\Phi_{1\mathbf{k}}^{+})E_{2\mathbf{k}}^{(d)}]-E_{1\mathbf{k}}^{(d)}E_{2\mathbf{k}}^{(d)}(E_{1\mathbf{k}}^{(f)}+E_{2\mathbf{k}}^{(f)})
\end{aligned} \tag{4.60}$$

The derivation of the last mean-field equation can be compactly written as follows:

$$8(E_f-\varepsilon_f)+2\sum_{i=1}^{4}\sum_{\mathbf{k}}\frac{\partial\varepsilon_{i\mathbf{k}}}{\partial E_f}n_F(\varepsilon_{i\mathbf{k}})=0. \tag{4.61}$$

Chapter 5

End states of 1D Kondo topological Insulator

In this chapter we will begin the effort to solve one of the mysteries of the first Kondo topological insulator, SmB_6. Recent measurements unambiguously show that the Dirac (crossing) point is not located in the bulk but buried deep in the valence band. Conventionally the crossing should be in the gap and velocity is controlled by the ratio of hybridization strength and the conduction electron bandwidth. This ratio is small for all Kondo materials. Yet experimentally the velocity is very large.

In order to understand SmB_6 we studied a much simpler, one dimensional model. The hope is to find a interacting regime which explains anomalous behavior. Here we present the phase diagram of the model, where we can clearly see the large enhancement of surface velocity and penetration depth. Our study is of course limited to large N approximation and could be very specific for one dimension.

One of the effects to emerge in our treatment is a reconstruction of the Kondo screening process near the boundary of the material, "Kondo band bending" (KBB). This process takes into account the effect of interactions. In the mean field theory approach KBB is equivalent to inhomogeneities in the renormalized mean field constants: fluctuations that grow as one approaches the boundary.

This chapter is in part based on my paper with Piers Coleman [117] that is currently accepted for publication in Phys. Rev. B[a].

[a] It can be found online as a preprint: arXiv:1403.6819

5.1 "Too-fast" surface states

As observed in the laboratory, the velocity of the surface states of SmB_6 is that of a conduction electron. This is going against all the predictions originating from numerical modeling

and mean field theory approximation.

Conventionally the Dirac (crossing) point of surface states is located inside the gap. Up to a numerical factor of order unity we can simply estimate the surface state velocity $v_{ss} = \partial E(k)/\partial k$ (assuming nearly linear generic dispersion of surface state $E(k)$) as the ratio of the gap (Δ_g) and $2k_F$, where the Fermi momentum k_F is defined before the gap opens, at for instance higher temperatures. It is safe to approximate k_F as a half-Brillouin zone. The final estimate simply looks like

$$v_{ss} \sim a\Delta_g/\pi \tag{5.1}$$

where a is a lattice constant. For concreteness let us plug in the typical numbers: the gap is of order 10meV and a is of order 5Å

$$\text{(for SmB}_6\text{)} \quad v_{ss} \sim 0.05 \text{ eV Å} \tag{5.2}$$

Note that units are not m/s, but eV Å, 6 eV Å$= 10^6$ m/s is equal to the speed of conduction electron in most materials.

$$6 \text{ eV Å} = 10^6 \text{ m/s}$$

I depict this situation in Fig. 5.1a.

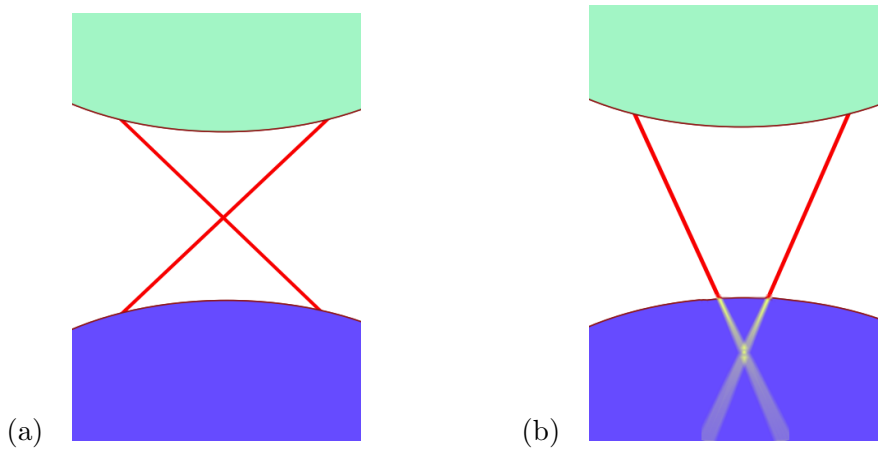

Figure 5.1: Schematic representation of a valence and conduction bands (in solid green and blue color) and surface state (solid red color). (a) Usual crossing point and (b) unusual crossing point outside the gap. In the unusual case (b) yellow color indicates that the states are not observable as they are mixed with delocalized states of the bulk.

However the only way for the observed velocity to be high is to originate from a Dirac (crossing) point well below Fermi energy, in the conduction or valence band. This situation

is depicted in Fig. 5.1b. The solid red color represents a localized surface state. Note that once the surface state dips into the valence band the localized electron are mixed with delocalized conduction electrons and one looses the definition of surface state altogether (depicted with a blurred out yellow color).

5.1.1 Experiments

There are numerous angle resolved photoemission (ARPES) experiments become available recently. One of the result of the first ARPES [118] is reproduced in Fig. 5.2, in the experiment the measured velocity is of order 0.3 eVÅ.

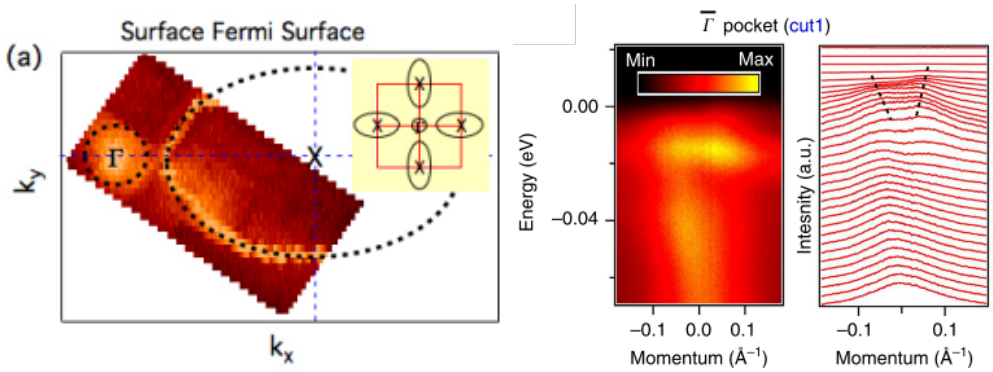

Figure 5.2: Reproduced from [118]. (left) A Fermi surface map of bulk insulating SmB_6 using a 7 eV laser source at a sample temperature of 6K, which captured all the low energy states between 0 and 4 meV binding energies. The dashed lines around X and Γ points are guides to the eye. Inset shows a schematic of Fermi surface. (right) Dispersion of the low-lying states and the corresponding momentum distribution curves near the Γ pocket

Another experiment was done by analyzing quantum oscillation pattern. Magnetic measurement allow to identify the size of the Fermi pockets and dispersion. I reproduced the results form the original paper [114] in Fig. 5.3. The results for surface mode velocity were even more drastically different from predictions. G. Li at al found velocity to be in the range of 3 to 6 evÅ, another order of magnitude higher than ARPES measurement.

5.2 One dimensional model

To gain further insight into the properties of interacting topological insulators, we study a one-dimensional model of topological Kondo insulators which can be

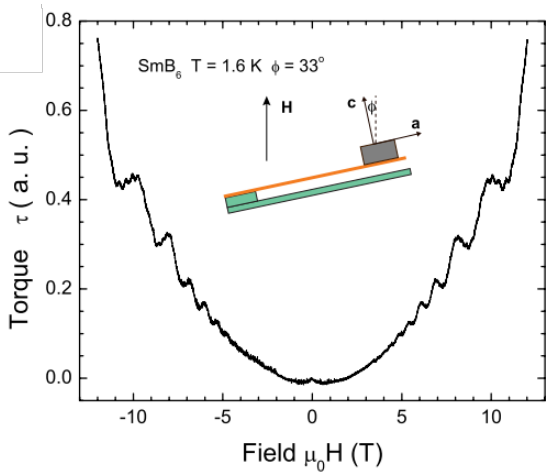

Figure 5.3: The field dependence magnetic torque τ for SmB_6. The $\tau(H)$ curve is overall quadratic, reflecting the paramagnetic state of samples. Oscillating patterns are observed in magnetic field larger than 6T. The inset is the sketch of the measurement setup. The sample stage is rotated to tilt magnetic field H in the crystalline a c plane. The magnetic field is applied to the sample with a tilt angle ϕ relative to the crystalline c axis.

regarded as the strongly interacting limit of the Tamm-Shockley model. Treating the model in a large N expansion, we find a number of competing ground-state solutions, including topological insulating and valence bond ground-states. One of the effects to emerge in our treatment is a reconstruction of the Kondo screening process near the boundary of the material ("Kondo band bending"). Near the boundary for localization into a valence bond state, we find that the conduction character of the edge state grows substantially, leading to states that extend deeply into the bulk. We speculate that such states are the one-dimensional analog of the light f-electron surface states which appear to develop in the putative topological Kondo insulator, SmB_6.

5.3 Goals

Topological insulators [119, 11, 14, 120, 17, 121, 6, 7, 12, 122, 123] have attracted great attention as a new class of band insulator with gapless surface or edge states, robustly protected by combination of time-reversal symmetry and the non-trivial topological winding of the occupied one-particle wavefunctions. The surface states of a topological insulator are "massless" excitations carried by an odd number of Dirac cones in the Brillouin zone.

Various proposals have been made for strongly correlated electron analogues[124, 96, 125, 126, 127, 128, 129, 9] of topological band insulators. To date the best candidate strongly correlated topological insulator is SmB_6, a local moment metal which transforms into a Kondo insulator, once the moments are screened at low temperatures ($< 70K$) [25]. This material was first predicted to be a topological Kondo insulator [96] and recently shown to exhibit conducting in-gap surface states, which develop below 4K [101, 102, 103]. While these results are consistent with a topological Kondo insulator, a definitive observation of Dirac cone excitations with polarized quasiparticles has not yet been reported. However, tentative data of the Dirac cone surface states have become available in both quantum oscillation [130] and ARPES measurements[118, 131, 132, 133]. One of the unexpected features of these measurements is the presence of "light", high-velocity surface quasiparticles, with the Dirac point far outside the gap. These tentative results are puzzling, because their group velocities appear 10 to 100 times larger than that expected in a heavy fermion band [134, 88].

These results provide motivation for the current chapter. Here we introduce a simple one dimensional "p-wave Kondo lattice" which gives rise to a topological Kondo insulator that can be studied by a variety of methods. In this initial study we carry out the simplest mean-field treatment of our model, an approach which is technically exact in the large N limit, using it to gain insight into the nature of the edge states and to propose variational ground-states for the model. This work is also an important warm-up exercise for a three dimensional model. The model is schematically depicted in Fig. 5.4. It can be regarded as a strongly interacting limit of the Tamm-Shockley model [135, 10, 136].

A second goal of this work is to gain insight into the impact of the boundary on the Kondo effect, a phenomenon we refer to as "Kondo band bending". In the conventional Kondo insulator model, the hybridization between local moments and conduction electrons is local and the strong-coupling ground state involves a Kondo singlet at every site, with minimal boundary effects. In the case of non-trivial topology the Kondo singlets are non-local objects [137, 138, 139] (Fig. 5.4) which are partially broken at the boundary. We seek to understand how this influences the Kondo effect and the character of the edge states at the boundary.

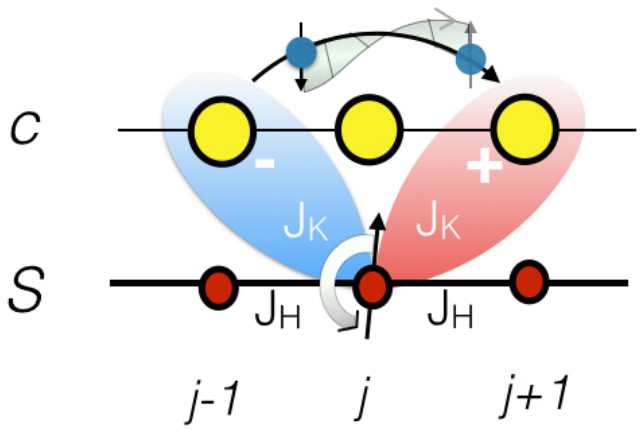

Figure 5.4: Schematic illustration of the 1D p-wave Kondo insulator Hamiltonian (5.3). The model contains a chain of Heisenberg spins coupled by an antiferromagnetic nearest neighbor Heisenberg coupling, plus a tight-binding chain of conduction electrons (c). Each localized moment is coupled to the conduction sea via a Kondo "cotunneling" term that exchanges spin between a localized moment at site j and a p-wave combination of conduction electron states formed between neighboring sites $j-1$ and $j+1$.

.

5.4 The model

Our model describes a conduction electron fluid interacting with an antiferromagnetic Heisenberg spin chain via a Kondo co-tunneling term with p-wave character. The Hamiltonian is given by

$$H = H_c + H_H + H_K, \tag{5.3}$$

where

$$H_c = -t\sum_{j\sigma}(c^\dagger_{j+1\sigma}c_{j\sigma} + \text{H.c}), \tag{5.4}$$

$$H_H = J_H\sum_i \mathbf{S}_j\cdot\mathbf{S}_{j+1}, \tag{5.5}$$

$$H_K = \sum_{j,\alpha\beta}\frac{J_K(j)}{2}\mathbf{S}_j\cdot p^\dagger_{j\alpha}\boldsymbol{\sigma}_{\alpha\beta}p_{j\beta}. \tag{5.6}$$

Here the site index runs over the length of the chain, $j\in[1,L]$, t is the nearest neighbor hopping matrix element, J_H is a nearest neighbor Heisenberg coupling and $J_K(j)$ is the Kondo coupling at site j. The chemical potential of the conduction electrons has been set to zero, corresponding to a half-filled conduction band. In contrast to the conventional 's-wave' Kondo model, here the Kondo effect is non-local. In particular, the electron Wannier

states that couple to the local moment have p-wave symmetry

$$p_{j\sigma} \equiv c_{j+1\sigma} - c_{j-1\sigma}. \tag{5.7}$$

The Kondo coupling now permits the process of "co-tunneling" whereby an electron can hop across a spin as it flips it. The odd-parity co-tunneling terms are a consequence of the underlying hybridization with localized p-wave orbitals. When this hybridization is eliminated via a Schrieffer-Wolff transformation, the resulting Kondo interaction contains an odd-parity form factor.

The boundary spins have a lower connectivity, giving rise to a lower Kondo temperature which tends to localize them into a magnetic state. To examine these effects in greater detail, we take the Kondo coupling $J_K(j) = J_K$ to be uniform in the bulk, but to have strength αJ_K at the boundary,

$$J_K(j) = \begin{cases} \alpha J_K & \text{endpoints } \ (j = 1 \text{ or } L), \\ J_K & \text{bulk } (j \in [2, L-1]). \end{cases} \tag{5.8}$$

By allowing the end couplings to be enhanced by a factor α we can crudely compensate for the localizing effect of the reduced boundary connectivity. In real 3D Kondo insulators, this surface enhancement effect ("Kondo band-bending") would occur in response to changes in the valence of the magnetic ions near the surface. For Sm and Yb Kondo insulators, the valence of the surface ions is expected to shift to a more mixed valent configuration, enhancing α, while in Ce Kondo insulators, the opposite effect is expected.

To formulate the model as a canonical field theory, we rewrite the spin $\mathbf{S}_j$ using Abrikosov pseudo-fermions $f_{j\sigma}$, as

$$\mathbf{S}_j = \sum_{\sigma\sigma'} f^\dagger_{j\sigma} \boldsymbol{\sigma}_{\sigma\sigma'} f_{j\sigma'}, \tag{5.9}$$

with the associated "Gutzwiller" constraint $n_{f,j} = 1$ at each site. After applying the completeness relations for the Pauli matrices in (5.6) we obtain the Coqblin-Schrieffer form of the Kondo interaction,

$$H_K = -\sum_{j\alpha\beta} J_K(j) \left(f^\dagger_{j\alpha} p_{j\alpha} \right) \left(p^\dagger_{j\beta} f_{j\beta} \right), \tag{5.10}$$

where we have imposed the constraint. In an analogous fashion, the local moment interaction (5.5) can be re-written as

$$H_H = -J_H \sum_{j\alpha\beta} (f^\dagger_{j+1\alpha} f_{j\alpha})(f^\dagger_{j\beta} f_{j+1\beta}). \tag{5.11}$$

If we now cast the Hamiltonian inside a path integral, we can factorize the Kondo and Heisenberg interactions using a Hubbard-Stratonovich decoupling,

$$\begin{aligned} H \to H_c &+ \sum_{j\sigma} \left[\bar{V}_j (c^\dagger_{j+1\sigma} - c^\dagger_{j-1\sigma}) f_{j\sigma} + \text{H.c.} + \frac{|V_j|^2}{J_K(j)} \right] \\ &+ \sum_{j\sigma} \left[\Delta_j f^\dagger_{j+1\sigma} f_{j\sigma} + \text{H.c.} + \frac{|\Delta_j|^2}{J_H} \right] \\ &+ \sum_j \lambda_j (n_{f,j} - 1), \end{aligned} \tag{5.12}$$

with the understanding that auxiliary fields V_i, Δ_j and λ_j are fluctuating variables, integrated within a path integral. The last term imposes the constraint $n_{f,j} = 1$ at each site.

In this formulation of the problem V_i determines the Kondo hybridization on site i and Δ_i is the order parameter for resonating valence bond (RVB)-like state formed on the link i between local moments. In translating our mean-field results back into the physical subspace of spins and electrons it is important to realize that the f-electron operators (which are absent in the original spin formulation of the model) represent composite fermions that result from the binding of spin flips to conduction electrons as part of the Kondo effect. By comparing (10) with (4), we see that the f-electron represents the following (three-body) contraction between conduction and spin operators:

$$\begin{aligned} \overbrace{\mathbf{S}_j \cdot \boldsymbol{\sigma}_{\alpha\beta} p_{j\beta}} &\equiv \left(\frac{2\bar{V}}{J_K} \right) f_{j\alpha}, \\ \overbrace{p^\dagger_{j\beta} \boldsymbol{\sigma}_{\beta\alpha} \cdot \mathbf{S}_j} &\equiv \left(\frac{2V}{J_K} \right) f^\dagger_{j\alpha}. \end{aligned} \tag{5.13}$$

At low energies, these bound-state objects behave as independent electron states, injected into the conduction sea to form a filled band and create a Kondo insulator.

5.4.1 Homogeneous mean field approximation

In the homogeneous mean field treatment of the Hamiltonian (5.12) we assume that the bulk fields V_j, Δ_j and λ_j are constants. The saddle-point Hamiltonian then becomes a translationally invariant tight binding model. For periodic boundary conditions, taking $\Delta_j = \Delta$, $V_j = V$, we obtain

$$H = H_{TB} + L\left(\frac{|V|^2}{J_K} + \frac{|\Delta|^2}{J_H} - \lambda\right). \tag{5.14}$$

H_{TB} can be written in momentum space as

$$H_{TB} = \sum_k (c^\dagger_{k\sigma}, f^\dagger_{k\sigma}) \overbrace{\begin{pmatrix} -2t\cos k & -2i\bar{V}\sin k \\ 2iV\sin k & 2\Delta\cos k + \lambda \end{pmatrix}}^{H(k)} \begin{pmatrix} c_{k\sigma} \\ f_{k\sigma} \end{pmatrix}. \tag{5.15}$$

This model is represented schematically in Fig. 5.5(a).

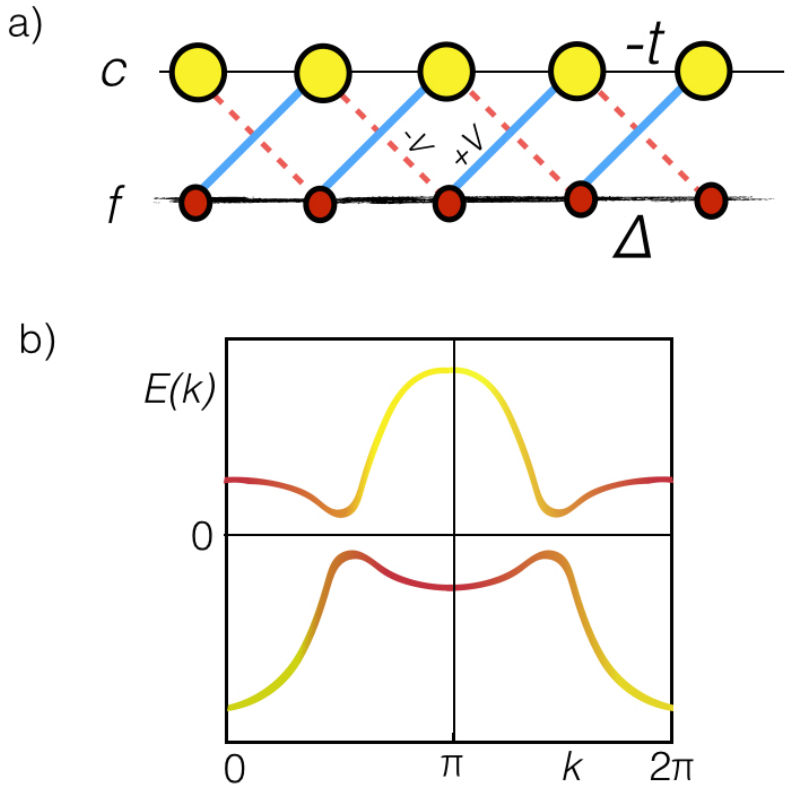

Figure 5.5: Illustrating the tight-binding model. (a) Real space structure. (b) Dispersion of quasiparticles, showing band inversion at $k = \pi$(5.15)

5.4.2 Large N limit

The mean-field treatment replaces the hard constraint $n_f = 1$ by an average $\langle n_f \rangle = 1$ at each site. This replacement becomes asymptotically exact in a large N extension of the model, in which the fermions have N possible spin flavors, $\sigma \in [1, N]$. Provided all terms in the Hamiltonian grow extensively with N, the path integral can be rewritten with an effective Planck constant $\hbar_{\text{eff}} = 1/N$ which suppresses quantum fluctuations as $N \to \infty$ and $\hbar_{\text{eff}} \to 0$. To scale the model so that the Hamiltonian grows extensively with N, we replace

$$J_H \to J_H/N, \qquad J_K \to J_K/N, \tag{5.16}$$

$$\sum_j \lambda(n_{f,j} - 1) \to \sum_j \lambda(n_{f,j} - Q). \tag{5.17}$$

where the last term imposes $n_{f,j} = Q$ rather than unity at each site. We shall examine the case where $Q = N/2$, corresponding to a particle-hole symmetric Kondo lattice. We shall restrict our attention to solutions where $\lambda = 0$, which gives rise to an insulating state in which both the conduction and f-bands are half-filled.

5.4.3 Topological class D

The mean-field Hamiltonian (5.15) can be classified according to the periodic table of free fermion topological phases[140, 123, 141]. The particle hole symmetry $\Xi : \Xi H(k)\Xi^\dagger = -H^T(k)$ is equivalent to the transformation $c_k \to c^\dagger_{\pi-k}$, $f_k \to f^\dagger_{\pi-k}$. In the two band basis of Hamiltonian (5.15) $\Xi = \tau_z$, where τ denotes a Pauli matrix acting in orbital space. According to the periodic table, symmetric Ξ corresponds to class D.

One way to see the non-trivial topology is to observe the evolution of the Hamiltonian throughout the Brillouin zone by writing it as a vector in three dimensional space: $H(k) = \vec{h}(k) \cdot \vec{\tau} + \epsilon_0(k)$ with $\epsilon_0(k) = (\Delta - t)\cos k$. For real V,

$$\vec{h}(k) = \begin{bmatrix} 0 \\ 2V \sin k \\ -(\Delta + t)\cos k \end{bmatrix}.$$

At $k = 0$ and $k = \pi$, the vector $\vec{h}(k)$ aligns along the $\hat{z}$ axis: if the sign of the scalar product

$\vec{h}(0) \cdot \vec{h}(\pi)$ of the two vectors is positive, vector $\vec{h}(k)$ traces a simply-connected path on the 2-sphere that may be contracted to a point, so the phase is topologically trivial. By contrast, a negative sign corresponds to a topologically non-trivial path that connects the poles of the sphere, indicating the topological phase. This can be summarized as

$$(-1)^{\nu} = \text{sign}(\vec{h}(0) \cdot \vec{h}(\pi)), \tag{5.18}$$

where $\nu = 0$ for trivial and $\nu = 1$ for topological phases. In our model $\vec{h}(0) \cdot \vec{h}(\pi) = -(t+\Delta)^2$ and hence $\nu = 1$ for any uniform solution with finite V.

The consequence of the topological invariance can be seen in the non-zero electric polarization P. A particle-hole transformation reverses the polarization, and since the Hamiltonian is invariant under this transformation it follows that $\Xi P \Xi^{\dagger} = -P$, allowing only two possible values of polarization: $P = 0$ or $P = e/2$ since P is defined modulo e. This is in fact the topological index of the chain. P can be computed via the Berry connection $A_k = i\langle u_k|\partial_k|u_k\rangle$[142] of the occupied bands, defined via periodic part of the Bloch function, u_k.

$$P = e\int_0^{2\pi} \frac{dk}{2\pi} A_k = \begin{cases} e/2 & \text{topological} \\ 0 & \text{trivial} \end{cases} . \tag{5.19}$$

The validity of this relation depends on the use of a *smooth* Berry connection A_k, which usually requires that we carry out a gauge transformation on the raw eigenstates. For example, consider the special case where $t = \Delta = V$. The negative energy eigenstates then take the form $\psi_k = (\cos(k/2), -i\sin(k/2))e^{i\phi(k)}$: choosing $\phi(k) = k/2$, the eigenstates then become continuous. If the orbital basis is centro-symmetric, the Berry phase only depends on ψ_k: $A_k = i\langle u_k|\partial_k|u_k\rangle = i\psi_k^{\dagger}\partial_k\psi_k$. Computing the Berry connection, we obtain

$$\begin{aligned} A_k &= ie^{-ik/2}\left(\cos\tfrac{k}{2}, i\sin\tfrac{k}{2}\right)\partial_k \begin{pmatrix} \cos(k/2) \\ -i\sin(k/2) \end{pmatrix} e^{ik/2} \\ &= \tfrac{1}{2}(\cos^2(k/2) + \sin^2(k/2)) = \tfrac{1}{2} \end{aligned}$$

so that

$$P = e\int_0^{2\pi} \frac{dk}{2\pi} A_k = \frac{e}{2},$$

resulting in a non-trivial half integer charge (per spin component) on the edge.

5.4.4 Edge states

The key property of topological insulators and superconductors is that at the particle-hole symmetric point, they develop zero energy edge states. A single non-degenerate state at zero energy can not be shifted up (or down) because particle-hole symmetry would then require at least two states with opposite energies, developing out of the single zero energy mode.

Though our ultimate goal is to consider non-uniform mean field solutions, we begin by examining the form of the topologically protected edge states for the mean-field Kondo lattice (5.15) with constant bond parameters. There is an interesting relationship with the topological Kitaev model[143], which we now bring out. The Kitaev model involves the formation of a "canted" valence-bond solid between nearest neighbor Majorana fermions, formed from symmetric and antisymmetric combinations of particles and holes, as shown in Fig. 5.6a. The edge states are then the Majorana fermions that are unable to form bonds. We shall show that at the special point where the all bond strengths are equal, the mean-field Kondo model involves the formation of a similar canted valence bond structure between antisymmetric and symmetric combinations of f and conduction electrons as shown in Fig. 5.6b.

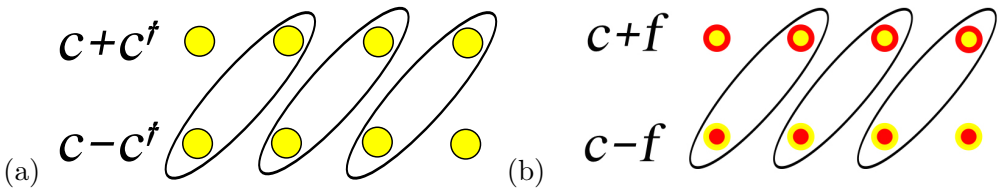

Figure 5.6: (a) Majorana decomposition of Kitaev model; (b) $t = \Delta = V$ limit of the tight binding model (5.15)

To demonstrate the edge state wave function we can choose f and c hopping to be equal $t = \Delta$, keeping the hybridization as a free parameter. The Hamiltonian (5.15) can be rewritten in the following simple form:

$$\begin{aligned} H_{(\Delta=t)} &= (\Delta + V)\sum_{j\sigma}(s^{\dagger}_{j+1\sigma}a_{j\sigma} + \text{H.c.}) \\ &+ (\Delta - V)\sum_{j\sigma}(s^{\dagger}_{j-1\sigma}a_{j\sigma} + \text{H.c}), \end{aligned} \tag{5.20}$$

where

$$a_{j\sigma} = (f_{j\sigma} - c_{j\sigma})/\sqrt{2}, \tag{5.21}$$

$$s_{j\sigma} = (f_{j\sigma} + c_{j\sigma})/\sqrt{2}. \tag{5.22}$$

The two terms in Hamiltonian (18) correspond to "right facing" and "left facing" bonds between a chain of "a" and "s" sites. In the particular limit that $\Delta = V$, the Hamiltonian consists entirely of right-facing bonds, as illustrated in Fig. 3b, with edge on the left and right composed of symmetric and antisymmetric combinations of conduction and f electrons. Note that at first glance this model breaks inversion symmetry, but in fact there is an additional $U(1)$ gauge invariance for f electrons: the phase of f can be rotated, effectively interchanging between antisymmetric a_j and symmetric s_j operators.

For all values of V and Δ, the zero-mode ψ_0 can be found solving $H_{(\Delta=t)}\psi_0 = 0$ with the ansatz

$$\psi_0 = \sum_j v_j s_j^\dagger + u_j a_j^\dagger. \tag{5.23}$$

Solving for $\{u_j, v_j\}$ in the case of $(V\Delta) > 0$ we can find left and right edge solutions. The left-hand edge state is given by

$$\begin{aligned} u_j &= 0, \\ v_j &= \begin{cases} \left(\frac{V+\Delta}{V-\Delta}\right)^{(j-1)/2} & \text{odd} \\ 0 & \text{even} \end{cases}. \end{aligned} \tag{5.24}$$

Hence, unless hybridization V or effective hopping Δ is zero the decay is exponential. The fact that $v_{even} = 0$ is due to particle hole symmetry: one can show that the zero-mode of bipartite lattice is defined only on one sublattice in a one-dimensional finite chain.

5.5 Mean field solution

We now consider a finite slab of material, examining the departures in V and Δ which develop in the vicinity of the boundaries a phenomenon we refer to as "Kondo band-bending". The allowed values of V_j and Δ_j are determined by the self-consistency equations

$$\begin{aligned} V_j &= -J_K(j) \left\langle (c_{j+1\sigma} - c_{j-1\sigma})^\dagger f_{j\sigma} \right\rangle, \\ \Delta_j &= -J_H \left\langle f_{j\sigma}^\dagger f_{j+1\sigma} \right\rangle. \end{aligned} \tag{5.25}$$

These equations derive from the requirement that the acton is stationary with respect to V_j and Δ_j at each site. The phase diagram is determined by the values of J_H, J_K and the edge parameter α. To explore the parameter space we carried out a series of a numerical calculations in which we seeded inhomogeneous order parameters V_j and Δ_j, iterating the self-consistency conditions until a convergent solution was found.

To examine the bulk properties, we began by imposing periodic boundary conditions. Using this procedure, we identified two bulk phases: a Kondo insulator and a metallic valence bond solid. The results of mean field calculations with periodic boundary conditions are presented in Fig. 5.7. The bulk phase diagram is of course independent of the edge parameter α.

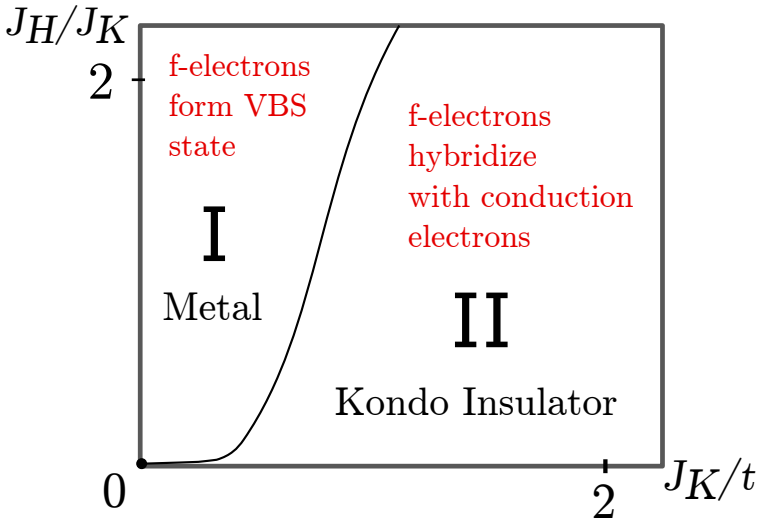

Figure 5.7: Schematic phase diagram of the bulk ground state contains a metallic phase (I) and an insulating phase (II). Phase II can be further divided depending on the properties of its surface states see Fig. 5.10.

We proceed with open boundary conditions and examine the nature of the bound states solutions that develop at the ends where the mean field parameters depart from the bulk values.

5.5.1 Phase I: Metallic VBS state

In this phase the RVB order parameter Δ_j becomes an alternating function of space, while V_j is zero. Consequently, the f-electrons form a valence bond solid (VBS) state, co-existing

with the unperturbed conduction sea. Dispersionless "spinon" bands above and below the Fermi energy, as shown in Fig. 5.8b. The gap between f-states is provided by the amplitude of Δ_j (justifying the notation) which is in turn equal to $J_H/4$. The metallic VBS phase is summarized in Fig. 5.8a,b.

The metallic phase does not have surface states and behaves the same way for open and closed boundary conditions. We found VBS state to be the lowest energy configuration in the left part of phase diagram as shown in Fig. 5.7.

Since there are two degenerate configurations of the VBS, one of the important classes of excitation of this state is a domain-wall soliton formed at the interface of the two degenerate vacua. In an isolated VBS, such as the ground-state of the Majumdar Ghosh model, or the Su-Schrieffer-Heeger model, such solitons are spin-1/2 excitations. However, in the 1D Kondo lattice, the Kondo interaction is expected to screen such isolated spins, forming a p-wave Kondo singlet exciton. In the metallic VBS, these solitonic excitons will be gapped excitations. However, as the Kondo coupling grows, at some point the excitons will condense, and at this point the VBS melts, forming a topological Kondo insulator.

5.5.2 Phase II: Kondo insulator

In the Kondo insulating phase the hopping Δ_j and V_j are both finite in the bulk and generally suppressed at the ends of the chain. This gapped heavy Fermi liquid is stabilized by large Kondo coupling as shown in Fig. 5.8(c,d). We find that the Kondo insulating phase exhibits two different kinds of boundary behavior. In the mean field theory, we can characterize these two phases by the fractional conduction electron character $n_c \in [0, 1]$ of the edge state. The first is adiabatically connected to the "Kitaev point" (see below) in which conduction electrons and composite f-electrons hybridize to form the a surface state with $n_c > 0$. In the second state, the edge state is a purely localized spin, unhybridized with the conduction electrons ($n_c = 0$).

"Kitaev" point

For general values of $\{J_K, J_H, \alpha\}$ there is no analytic solution. However at the point where $\{J_K, J_H, \alpha\} = \{2, 4, 2\}$ $\Delta_j = V_j = t$ are constants in space. We now show that at this point

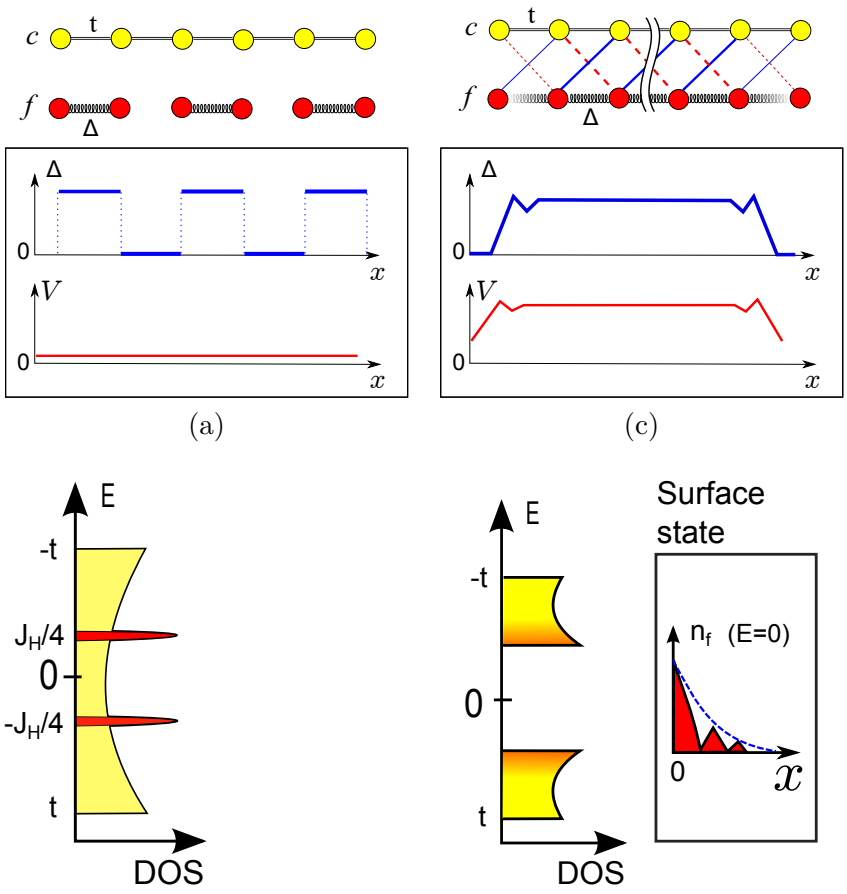

Figure 5.8: Cartoon representation of two distinct phases in Fig. 5.7. We plot spatial dependence of V_j and Δ_j and density of states (DOS). Phase I (a and b): Metallic states with suppressed hybridization. It does not support surface states. Phase II (c and d): Kondo topological insulator that support surface states. Inset in d is the profile of a typical surface state decaying into the bulk as a function of distance.

each spin component of the mean-field theory corresponds to a two copies of the Kitaev chain, with a single fermionic zero mode at each boundary, as can be seen from the form of the wave function in equation (5.24). We refer to this particular point in the phase diagram as the 'Kitaev point'.

At this point, following (5.20), the mean-field Hamiltonian takes the form

$$H_{(\Delta=t)} = 2t \sum_{j=1}^{L-1} \sum_{\sigma} (s^{\dagger}_{j+1\sigma} a_{j\sigma} + \text{H.c.}), \tag{5.26}$$

where $s_{j\sigma}$ and $a_{j\sigma}$ are the symmetric and antisymmetric combination of states $\frac{1}{\sqrt{2}}(f_{j\sigma} \pm c_{j\sigma})$.

This Hamiltonian commutes with the zero modes

$$[H, s_{1\sigma}] = 0, \qquad [H, a_{L\sigma}] = 0 \tag{5.27}$$

so for each spin, there is one fermionic zero mode per edge, each involving a hybridized combination of conduction and f-electrons with $n_c = \frac{1}{2}$. To see the connection with the Kitaev model, we divide both $s_{j\sigma}$ and $a_{j\sigma}$ into two Majorana fermions as follows,

$$s_{j\sigma} = \frac{1}{\sqrt{2}}(\gamma^1_{j\sigma} + i\gamma^2_{j\sigma}), \qquad a_{j\sigma} = \frac{1}{\sqrt{2}}(\gamma^3_{j\sigma} - i\gamma^4_{j\sigma}). \tag{5.28}$$

Using (5.26), the Hamiltonian now splits into two independent components,

$$H_{(\Delta=t)} = -i2t \sum_{j=1}^{L-1} \sum_{\sigma} (\gamma^1_{j+1}\gamma^4_j + \gamma^2_{j+1}\gamma^3_j), \tag{5.29}$$

corresponding to a pair of Kitaev chains per spin component. This is natural, because each Kitaev chain has one Majorana zero mode per edge. Since a pair of Majoranas make one normal fermion, this corresponds to one fermionic zero mode per edge.

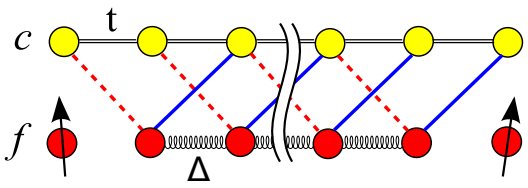

Figure 5.9: Magnetic phase (red color in Fig 5.10).

5.5.3 Magnetic Edge state.

In the magnetic edge state, the boundary spins do not undergo the Kondo effect, forming an unhybridized magnetic edge state. If the boundary parameter $\alpha = 1$, the Kondo temperature at the boundary is smaller than in the bulk, because the terminal boundary spins have only one nearest neighbor. This means on cooling, that the boundary Kondo interaction is unable to scale to strong coupling before a gap develops in the bulk, leading to an unquenched boundary spin. When $\alpha > 1$, the Kondo effect is able to develop at the boundary, occurs at the boundary, provided J_K is not at weak coupling. At smaller values of J_K, the decoupled magnetic phase develops, denoted by the red region in Fig. 7 (a). In this phase, there is no hybridization of the edge state with the bulk conduction electrons ($n_c = 0$), and the topological edge state disappears.

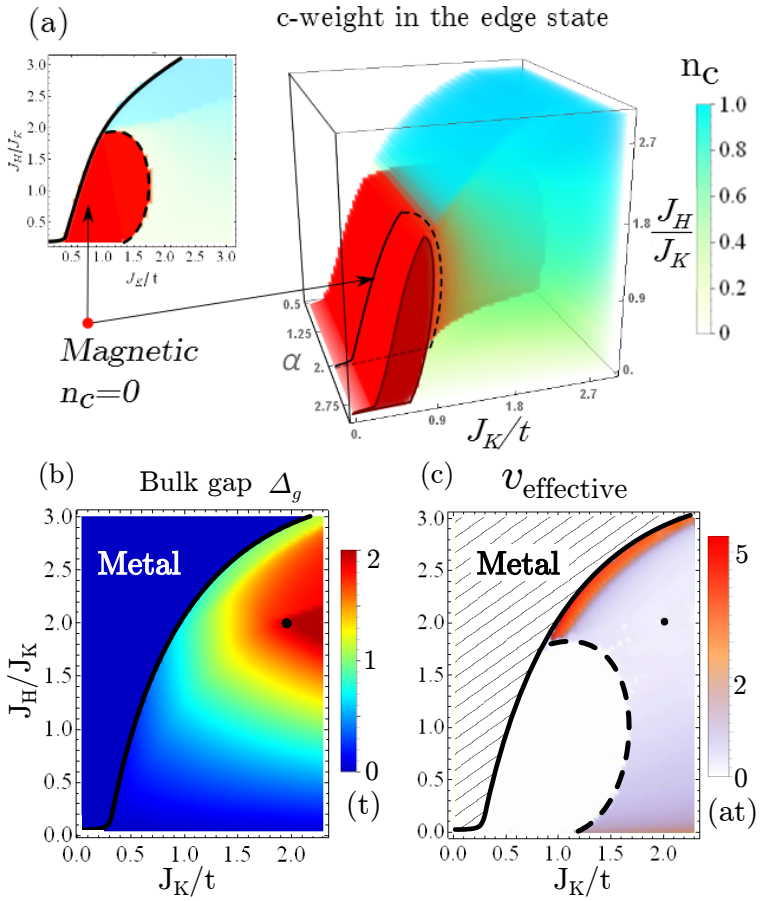

Figure 5.10: The surface phase diagram. With the addition of a renormalized Kondo coupling at the surface $\alpha = J_K^{boundary}/J_K$. (a) Red color represent pure f-states with no c-electron mixing, $n_c = 0$. Inset is the cut along $\alpha = 2$. (b) is the bulk gap Δ_g in units of t for $\alpha = 2$, identifying the "Kitaev point" as the black dot. (c) displays the inferred group velocity measured in units of at, derived from the numerically measured penetration depth of the edge states using $v = \Delta_g \xi$. The mean field calculations were done on a chain of 70 unit cells.

5.6 Results and Discussion

5.6.1 Where are the light surface states?

One of the interesting features of current experiments on the Kondo insulator SmB_6, is that the putative topological surface states seem to involve high-velocity quasiparticles, rather than the heavy, low-velocity particles predicted by current theories. Our mean-field results on the one-dimensional p-wave Kondo chain suggest that this may be because the change in character of the Kondo effect at the boundary leads to edge states with a large conduction electron component.

For a relatively high magnetic interaction, J_H, the one-dimensional edge states in our mean-field treatment develop majority conduction electron character, forming "light" edge states which penetrate deeply into the bulk.

In a non-interacting topological insulator, the transition to a topologically trivial phase occurs via a quantum phase transition in which the bulk gap closes. In this case, the penetration depth grows with inverse proportion to the bulk gap Δ_g.

$$\xi = v_F/\Delta_g. \tag{5.30}$$

However, in the p-wave Kondo chain, the transition to a metallic VBS is a first order transition at which the bulk gap remains finite. In this case, the rapid growth in the penetration depth of the edge state is associated with an increase in the conduction character, driving the enhanced group-velocity of the edge-states (5.30). This is a novel and interesting consequence of the response of the Kondo effect to the boundary - "Kondo band-bending".

To demonstrate this behavior, we have carefully examined the properties of the edge states in our model. The phase diagram showing the evolution in the conduction character of the end states is shown in Fig. 5.10a. Within the bulk topological insulator phase, the character of the edge states varies dramatically, ranging from equal f- and c- character to edge states of predominantly conduction electron character near the first order boundary. Fig. 5.10b shows the dependence of the insulating gap Δ_g, showing that it remains finite at the first order phase boundary to the VBS metal.

We can estimate the effective velocity of the edge states by combining the numerically measured coherence length of the edge state and the bulk gap, according to

$$v_{\text{effective}} = \Delta_g \xi. \tag{5.31}$$

This quantity is found to increase dramatically near the first order boundary into the metallic VB state (see Fig. 5.10c), unlike a non-interacting topological insulator, here the increase in ξ is due to a rapidly increasing amount of conduction character in the edge-states, and is not accompanied by a gap closure, so that the effective velocity of the edge states $v_{\text{effective}}$ rises considerably.

5.6.2 Strong-coupling ground state wave function

An alternative way to understand a Kondo insulator is through the character of its strong-coupling wavefunction. In an conventional Kondo insulator, the strong coupling ground-state is an array of Kondo singlets. If we write

$$A_j^\dagger = \sum_{\sigma=\pm\frac{1}{2}} f_{j\sigma}^\dagger c_{j,-\sigma}^\dagger \mathrm{sign}(\sigma), \tag{5.32}$$

then the strong coupling ground-state of the s-wave Kondo insulator is simply a valence bond solid of Kondo singlets:

$$\begin{aligned} |KI\rangle &= \prod_{j=1}^{L} A_j^\dagger |0\rangle \\ &= \end{aligned} \tag{5.33}$$

where a line denotes a valence bond between a conduction electron (open circle) and a local moment (closed circle).

What then is the corresponding ground-state for the topological Kondo insulator? We can construct variational wavefunctions for the topological Kondo insulator by applying a Gutzwiller projection to the mean-field ground-state. Unlike the s-wave Kondo chain, to preserve the topological ground-state, we need to consider large values for both the Kondo and the Heisenberg coupling. An interesting point to consider is the Kitaev point, where the singlet structure of the mean-field ground-state becomes highly local. By projecting the mean-field ground-state we obtain

$$|TKI\rangle = P_G \prod_j Z_j |0\rangle, \tag{5.34}$$

where

$$Z_j = \sum_{\sigma=\pm\frac{1}{2}} a_{j\sigma}^\dagger s_{j+1,-\sigma}^\dagger \mathrm{sign}\sigma \tag{5.35}$$

with $a_{j\sigma}^\dagger = (f_{j\sigma}^\dagger + c_{j\sigma}^\dagger)/\sqrt{2}$ and $s_{j\sigma}^\dagger = (f_{j\sigma}^\dagger - c_{j\sigma}^\dagger)/\sqrt{2}$ as before, whereas $P_G = \prod_j (n_{f\uparrow}(j) - n_{f\downarrow}(j))^2$. Now the valence bond-creation operator

$$Z_j^\dagger = \frac{1}{2}\sum_\sigma (f_{j\sigma}^\dagger f_{j-\sigma}^\dagger + f_{j\sigma}^\dagger c_{j+1,-\sigma}^\dagger$$

$$- \quad c^\dagger_{j\sigma} f^\dagger_{j+1,-\sigma} - c^\dagger_{j\sigma} c^\dagger_{j+1,-\sigma}) \mathrm{sign}(\sigma) \tag{5.36}$$

is non-local. The projected wavefunction of the topological Kondo insulator (TKI) now involves a multitude of configurations forming a one-dimensional resonating valence bond (RVB) state between the local moments and conduction electrons. Schematically,

$$|TKI\rangle = \sum$$ 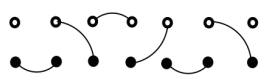 , (5.37)

where we associate a minus sign with left-facing Kondo singlets and conduction electron pairs. In this picture, the edge-states correspond to unpaired spins or conduction electrons at the boundary.

$$\begin{aligned} |\mathrm{edge}, \sigma\rangle &= P_G s^\dagger_{1\sigma} \prod_j Z^\dagger_j |0\rangle \\ &= \sum \\ &+ \sum \end{aligned} \tag{5.38}$$

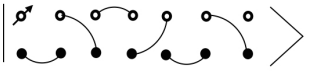

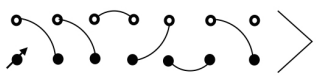 .

At the current time, except in the large N limit, we do not yet know if there is a particular combination of J_K, J_H and hopping t for which the short-range RVB wavefunction is an exact ground-state for the TKI.

5.6.3 Further outlook

One of the interesting unsolved questions is why different methods of growing SmB_6 sometimes suppress the topological surface states. On the one hand, when grown in Al flux, SmB_6 has robust surface states with a low temperature plateau conductivity, whereas the crystals produced with the floating zone method exhibit no plateau conductivity, even though the samples are thought to be cleaner [144]. Based on our simple one-dimensional model, we speculate that this may be because the ordered surface supports localized magnetic moments which in three dimensions, magnetically order. By contrast, for reasons not currently clear, the Al flux grown samples appear to sustain non-magnetic surface states, possibly due to a valence shift at the surface, giving rise to topological surface states. A

more detailed understanding of the situation awaits an extension of our current results to a three dimensional model along the lines of [136]. This is work that is currently underway.

Finally, we note that the model we have discussed in this chapter can also be engineered in a framework of ultracold atoms where a double well lattice potential is populated with mobile atoms in s and p orbitals[146]. This may provide a setting for a direct examination of the 1D edge states.

Chapter 6

Chapter 6: S-P Model

In this final chapter we will investigate some possible solutions for the large Fermi velocity of the surface states in Kondo insulators. Here our approach will change to a more phenomenological one and to higher dimensions. Chapter begins with current explanation (or the lack of thereof) of the mystery, then we study the "S-P" model which is as an extension of the model from chapter 5 to 2D and we leave 3D for future works.

In the one-dimensional model (Chapter 5) we faced with the problem that in the magnetic phase, where f-electron decoupled from the surface conduction electrons, the topological state disappeared. We believe now that this is an artifact of low dimensionality. *According to our preliminary results*, in higher dimensions the surface state still exists but becomes light. In one dimension it is only protected by particle-hole symmetry. However in two and three dimensions, the topological insulator isprotected by time reversal symmetry,

In the following we demonstrate that a highly renormalized chemical potential (extreme case of Kondo band banding – KBB) in the bulk can be physically thought as a breakdown of the Kondo singlet. It can be characterized as a phase shift in the surface state wave function. We will present solutions obtained to the (i) energy of the Dirac point, (ii) decay length of the wave function and (iii) surface state velocity as a function of the phase shift. We find that as a result of surface Kondo breakdown, the Dirac point sinks in the valance band along with the exceedingly light surface states in accord with experiments.

This chapter is based on work in progress with Piers Coleman and Onur Erten and there is no reference to date.

6.1 Current explanations of light surface states

Very few suggestions were put to the table to the date of this writing[1]. We are also aware of several undergoing ideas. Moreover, some argue that it is simply too complicated and surfaces are uniquely contaminated. To this point some still think that SmB_6has no protected surface states.

There are two related numerical studies that address this issue. In the first example, a similar to Samarium hexaboride compound SmP_6 with plutonium instead of boron is considered. This material have been treated with Dynamical Mean field theory (DMFT), which takes a good care of the interactions at every single site. The results [147] are reproduced in the Fig. 6.2a. In that figure it is clear that surface states are actually "dipped" into the valence band, so that the Dirac (crossing) point is not reachable experimentally as it mixes with a continuum.

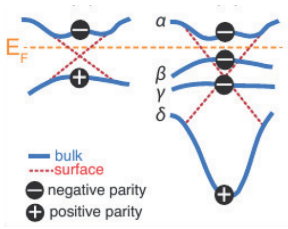

Figure 6.1: Reproduced from [148]. Schematic pictures showing (left) usual and (right) unusual band inversions. In SmB_6, parity-inverted bands are α and δ, but two more bands β and γ are located between them.

This idea was embraced in the following paper [148] and can be summarized in the Fig. 6.1. On the left there is a naive (usual) band inversion that would lead to a Dirac point in the gap and on the right the unusual inversion allows the Dirac point to sink. Although the later work is in the non-interacting density functional theory (DFT) approximation the claim is that interactions act in a very simple way by reducing (renormilizing) the scale by a factor of 10 which is supported by their DMFT study.

Is the question solved? Most likely not. Firstly, the velocity is still order of magnitude off from experimental as it gives ~ 0.06 eVÅ. In the process of deriving the band structure the authors rescaled the results of DFT by a factor of 10, but even without rescaling the

[1]To review the experimental observation of light surface states please see the first section of chapter 5.

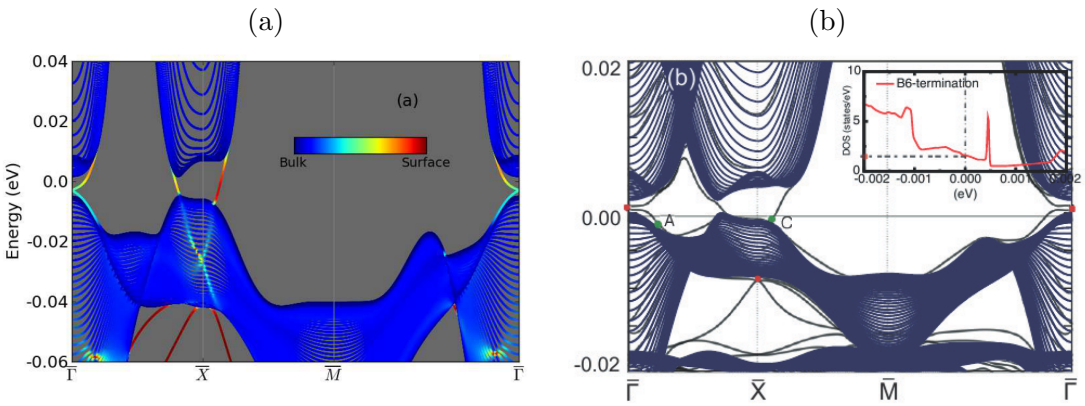

Figure 6.2: (a) Reproduced form [147]. Surface states of PuB_6 on (001) surface. The band structure is calculated with a tight-binding model for a 60-layer slab constructed from the effective topological Hamiltonian including Pu-d-e_g orbitals and Pu-f orbitals. The weight of surface state (the probability of each state in the first two layers on surface) are indicated by color, red means more weight on the surface, blue means more weight in the bulk. (b) Reproduced from [148]. DFT band structures of SmB_6 slabs with the B_6 -terminated surface. Note that the energy scales are reduced by 1/10. Blue shaded region represents the projection of SmB_6 bulk bands to the (001) surface BZ. Red dots represent the crossing (Dirac) points of metallic surface bands. Insets show the DOS (per Sm layer) of each surface termination.

DFT result would give .6 eVÅwhich still is around 10 times less than experimental (5 eV Å).

Secondly, following magnetic measurements one concludes that the g-factor of the nearest to Fermi energy multiplet is so small that it is more likely to have a doublet configuration in contrast to what density functional theory predicts. Finally, to open a gap in the unusual band inversion hybridization should be orders of magnitude higher. It is not unusual on itself but in this material, where the Kondo scale is ($T_K = 50$K) is quite low, one shouldn't expect a very high hybridization matrix element.

I will turn now to a quite simple example of a family of model Hamiltonians that would phenomenologically account for a faster surface states in a more or less tractable way. The band structure of SmB_6 is such that the band inversion is happening near X = $(0,0,\pi)$ point. I will instead consider a more transparent for presentation example of a band crossings around Γ point, leaving the straightforward modification for the paper in press.

6.2 2 band model with decoupled f-electron at the edges

We address this question in the context of surface Kondo breakdown where the Kondo effect shuts off on the surface layer, resulting in a change of valence of Sm on the surface which has indeed been observed by x-ray absorption spectroscopy experiments [144]. As a result the surface states are no longer compensated: they have more conduction electron character than local moment. Related with Luttenger sum rule, the removal of an electron leads to a large Fermi surface and the dominant conduction electron character gives rise to light surface states with large penetration depth in agreement with quantum oscillations[130] and ARPES[112, 118, 132, 113]. Large penetration depth implies that the surface states penetrate deeper in the bulk, thus much less affected by the surface disorder, providing an intuitive understanding for the quantum oscillations at large fields. We predict that the large penetration depth can be measured by thickness dependent transport measurements.

We start with the periodic Anderson model:

$$\begin{aligned} H &= \sum_{k,\sigma} \epsilon_k c^\dagger_{k\sigma} c_{k\sigma} + \tilde{V} \sum_k \phi(k)_{\sigma\sigma'} c^\dagger_{k\sigma} f_{k\sigma'} \\ &\quad + \sum_k \tilde{\epsilon}_{fk} f^\dagger_{k\sigma} f_{k\sigma} + U \sum_i n_{if\uparrow} n_{if\downarrow} \end{aligned} \tag{6.1}$$

where $c^\dagger (f^\dagger)$ are conduction electron (local moment) creation operators. ϵ_k are the conduction electron dispersion, $\tilde{V}$ and $\tilde{\epsilon}_{fk}$ are the bare (non-renormalized) hybridization and local moment dispersion; $\phi(k)_{\sigma\sigma'}$ is the form factor, $\phi_{\sigma\sigma'} = [\sigma_x \sin(k_x a) + \sigma_y \sin(k_y a) + \sigma_z \sin(k_z a)]$ (From now on we work units of $a = 1$). U is the onsite Coulomb repulsion on the f sites. The standard procedure is proceed is to introduce slave-bosons which project out the double occupancy on the f sites and do a saddle point approximation which gives rise to the mean-field equations[149].

That leaves us with a single particle Hamiltonian. In the following we introduce the phenomenological Hamiltonian to describe Kondo band bending. In two dimensions "S-P" Hamiltonian of a topological Kondo insulator can be written in a block diagonal form.

$$H = \sum_k \Psi^\dagger_k \begin{pmatrix} H_\uparrow & \\ & H_\downarrow \end{pmatrix} \Psi_k$$

in the four-dimensional basis $\Psi^T = \{c_\uparrow, f_\downarrow, c_\downarrow, f_\uparrow\}$. Where

$$H_\uparrow(k) = H_\downarrow(-k) = \begin{pmatrix} \epsilon_k - \mu_c & iV(\sin k_x + i \sin k_y) \\ iV(\sin k_x - i \sin k_y) & \epsilon_k^f + \lambda \end{pmatrix} \tag{6.2}$$

and

$$\epsilon_k = -2t(\cos k_x + \cos k_y) \tag{6.3}$$

$$\epsilon_k^f = 2t^f(\cos k_x + \cos k_y) \tag{6.4}$$

the Hamiltonian incorporates only the nearest neighbor hopping. μ_c and λ are relative chemical potentials of conduction electrons and localized f-electrons correspondingly; V is renormalized hybridization amplitude.

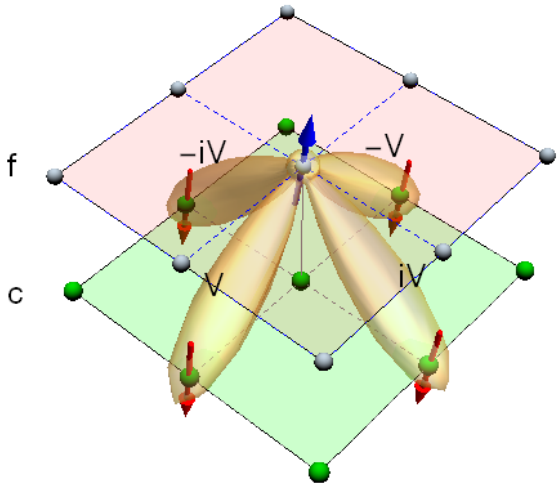

Figure 6.3: 2D schematic of the model presented on the xy plane. Due to the opposite parity of the orbitals, onsite hybridization vanishes, then the nearest neighbor local moment and conduction electron can hybridize with a spin dependent p-wave form factor, $\phi(k)_{\sigma\sigma'}$ as in eq. (6.1)

In other words, our topological Kondo insulators is based on spin-orbit coupled p orbital local moments and s-like conduction electrons. This model captures all the essential physics of SmB_6 where the hybridization is between f local moments and d conduction electrons.

6.2.1 Analytical consideration

Some typical examples of band structure for both zero and non-zero hybridization are plotted ofn Fig. 6.4. As was discussed before f-band has negative parity and the system opens the gap that protects band inversion. Assuming that chemical potential of the system is in the gap, Fig. 6.4 is an example of a topological insulator with one Dirac cone around the projected to the surface $\bar{\Gamma}$ point.

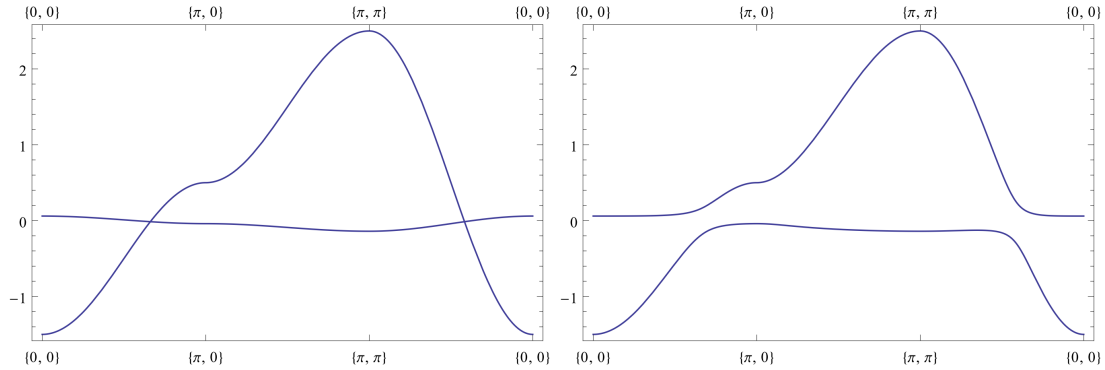

Figure 6.4: Two band "S-P" model. Band structure for the case of (left) no hybridization and (right) non-zero hybridization

Exact solution

It turns out that we can solve the Hamiltonian in the absence of KBB exactly. All the parameters are constant as functions of space. The key ingredient to find the exact solutions is to guess the ansatz.

The "S-P" Hamiltonian (6.2) is 4x4 Hamiltonian but solving only its 2x2 is sufficient. The new basis reads $\Psi'^T = \{c_\uparrow, f_\downarrow\}$ and the Hamiltonian (6.20) becomes

$$H'(k) = \begin{pmatrix} \epsilon_k - \mu_c & V(k) \\ \bar{V}(k) & -\alpha\epsilon_k + \lambda \end{pmatrix} \tag{6.5}$$

where I have introduced a parameter α as a (small for Kondo systems) ratio $t = \alpha t^f$. I also absorbed extra imaginary unit into definition of V, and $V(k) = V(\sin k_x + i \sin k_y)$. To set up the ground for the calculations let me introduce notations

$$\begin{aligned} c_x = \cos(k_x) \quad c = \cos(k_x) \quad \bar{c} = \cosh(k_x) \\ s_x = \cos(k_x) \quad s = \sin(k_x) \quad \bar{s} = \sinh(k_x) \end{aligned} \tag{6.6}$$

which leads to

$$H'(k) = \begin{pmatrix} -2t(c_x + c) - \mu_c & V(s_x + is) \\ V(s_x - is) & -\alpha(c_x + c) + \lambda \end{pmatrix} \tag{6.7}$$

We will assume the following solution

$$\Psi = \begin{pmatrix} \sqrt{\alpha} \\ 1 \end{pmatrix} e^{ik_x x + i(k_y + i\kappa)y} \tag{6.8}$$

the imaginary part of the exponent essentially performs analytically continuation of the eigenvalues in the complex plane. We will make sure that the energy stays in the real domain. Note that replacement of $k_y \to ky - i\kappa$ means that we will replace

$$\begin{aligned} c &\to c\bar{c} - is\bar{s} \\ s &\to s\bar{c} + ic\bar{s} \end{aligned} \tag{6.9}$$

We will now solve the eigenvalue equation $H'(k)\Psi = E(k)\Psi$

$$E(k) = \epsilon_k - \mu + \frac{1}{\sqrt{\alpha}} V(k) \tag{6.10}$$

$$E(k) = -\alpha\epsilon_k + \lambda + \sqrt{\alpha} V(k) \tag{6.11}$$

The *reality condition on energy* constrains κ. One can write imaginary part of eq. (6.10) as $2ts\bar{s} - Vs\bar{c} = 0$, and thus

$$\tanh \kappa = \frac{V}{2t\sqrt{\alpha}} \tag{6.12}$$

Combining both equation (6.10,6.11) one can write

$$\epsilon_k(\alpha + 1) - (\mu + \lambda) = \frac{\bar{V}(k)\alpha - V(k)}{\sqrt{\alpha}} \tag{6.13}$$

little manipulation with the use of κ from (6.12) one finds

$$cos(ky) = c = \frac{\sqrt{1 - \frac{V^2}{4\alpha t^2}}}{\left(\frac{V^2}{\alpha t} - 2t\right)} \left[\frac{\mu + \lambda}{\alpha + 1} + \frac{V}{\sqrt{\alpha}} s_x \frac{\alpha - 1}{\alpha + 1} + 2tc_x \right] \tag{6.14}$$

our final result is the dispersion for the surface state

$$\boxed{E(k) = 2\frac{V\sqrt{\alpha}}{\alpha + 1} s_x + \frac{\lambda - \alpha\mu}{\alpha + 1}} \tag{6.15}$$

We can compare it with the hybridization term $V(k) = V(\sin(k_x) + i\sin(ky))$ in the original Hamiltonian. Up to a factor $2\sqrt{\alpha}/(1 + \alpha)$ the boundary velocity is equal to hybridization

scale. This is important because exactly the same result can be obtained using small $|\mathbf{k}-\mathbf{k}_F| \to 0$, see for example Volovik calculation below (Eq. 6.16) or from topological insulator perspective [150][2].

So far, we have learned that in this model for arbitrary large parameters, hybridization V in the Hamiltonian (6.2) can be treated perturbatively, as if ratio V/t is vanishingly small. This is a surprising fact we are not quite sure why is that the case.

Perturbative calculation

We will now turn to a perturbative quantum mechanical calculation. It is convenient to first write the Hamiltonian up to a second order and introduce mass of the bands. "Heavy" band of f electrons (mass m_2) will have dispersion proportional to $\frac{k^2}{m_2}$. "Light" conduction band (mass m_1) has dispersion proportional to $\frac{k^2}{m_1}$.

$$H^{2nd} = \frac{1+\tau_3}{2}\frac{k^2-k_F^2}{2m_1} - \frac{1-\tau_3}{2}\frac{k^2-k_F^2}{2m_2} + \frac{V}{k_F}\tau_1(k_x\sigma_x + k_y\sigma_y) \tag{6.16}$$

We next expand the Hamiltonian (6.16) near the two point opposite on the Fermi surface:

$$k_1 = (k_x, k_F - k_y) \tag{6.17}$$

$$k_2 = (k_x, -k_F + k_y) \tag{6.18}$$

As was pointed out by Volovik [151] due to symmetry scattering between these two point can be thought as a reflection problem of a hard wall. We thus simply consider just the first point (6.17) in momentum space and hard boundary conditions. In the linearized version of Hamiltonian we first make a substitution $k_y \to -i\partial_y$ and split the Hamiltonian into

$$H^{2nd} = H^{(1)} + H^{(2)}, \tag{6.19}$$

where $H^{(2)}$ is a perturbation that is controlled by the smallness of the ratio V/k_F. Actually $H^{(2)}$ has already presented itself as the last term in eq. (6.16).

$$H^{(1)} = k_F\left(\frac{1+\tau_3}{2}\frac{i}{2m_1} - \frac{1-\tau_3}{2}\frac{i}{2m_2}\right)\partial_y - V\tau_1\sigma_y \tag{6.20}$$

$$H^{(2)} = \frac{V}{k_F}\tau_1\sigma_x k_x \tag{6.21}$$

[2]Most of reviews for topological insulators display similar calculation

As before we will resort to 2x2 Hamiltonian by choosing a different basis $\Psi'^T = \{c_\uparrow, f_\downarrow\}$ and the Hamiltonian (6.20) becomes

$$H'^{(1)} = i\frac{k_F}{m_1}\begin{pmatrix}1 & 0\\ 0 & -\alpha\end{pmatrix}\partial_y + \begin{pmatrix}-\mu & V\\ V & \lambda\end{pmatrix} \tag{6.22}$$

one can find the eigenfunction and eigenvalue of this Hamiltonian with hard boundary conditions (reflection of an infinite wall potential) and then calculate the perturbative energy by projecting $H'^{(2)}$ onto the ground state of $H'^{(1)}$

$$\Psi = \begin{pmatrix}\sqrt{\alpha}\\ 1\end{pmatrix}\exp\left[ik_x x + \frac{m_1}{\alpha k_F}\left(i\frac{\lambda\alpha}{1+\alpha}y - \sqrt{\alpha}Vy\right)\right] \tag{6.23}$$

Comparing with the exact solution in eq. (6.12) one can observe the exact matching of the decaying part of the wave function (for small V, $\tanh x \simeq x$), bearing in mind that $k_F \simeq 2tm_1$. The oscillatory part is not at all close, but as it turns out the energy dispersion is independent of the oscillatory part: when calculating projection, the oscillating integrals will vanish.

The result for energy, after projecting is identical to the exact formula (6.15). Namely

$$E(k) = \left\langle \psi_1 | H'^{(2)} | \psi_1 \right\rangle = 2\frac{V\sqrt{\alpha}}{\alpha+1}k_x + \frac{\lambda - \alpha\mu}{\alpha+1} \tag{6.24}$$

this is small k expansion of the exact result, but $\sin k_x$ can be simply restored as if $H'^{(2)}$ itself were kept at all orders in k_x. Once again I stress, that while it seems important to keep the small parameter V/k_F sufficiently small, the result seems to be independent of it. This can partially justify consideration of larger k_x in the next part, where KBB is introduced and the exact solution can no longer be obtained.

In conclusion, we are mostly interested in the case where chemical potential for f-electrons is not a constant in space, but the exact solution will not likely to be available. However as I showed above, the Volovik solution matches precisely to the exact solution, so might be able to use Volovik approach for the part where exact solution is not available.

Phase shift and KBB

Physically, we would like to account for the effective valence change of the samarium electrons. Similar to heavy fermion formation of a small Fermi surface, where valence changes

by one we would like to see similar valence shift which would push surface states away, move the Dirac point down and greatly increase the Fermi velocity

Kondo band bending (KBB) can be described by sudden change of chemical potential for localized f-electrons λ. To model this effect we suggest to introduce a phase shift. So instead of putting the wave function like (6.8) I will force the bottom part of the spinor (the f-component) to have a phase shift.

$$\begin{pmatrix} \sqrt{\alpha} \\ 1 \end{pmatrix} \rightarrow \begin{pmatrix} \sqrt{\alpha} \\ e^{i\phi} \end{pmatrix} \tag{6.25}$$

After solving a new eigenvalue problem, the energy will gain a term that is proportional to k_x^2 and what is more important the proportionality constant is of order t of conduction electrons. After some calculations one can get

$$E'(k_x, k_y) = E_0' + V\sqrt{\alpha} r(\phi) k_\perp + \alpha t \frac{e^{\frac{2\kappa\phi}{k_z}} - 1}{\alpha e^{\frac{2\kappa\phi}{k_z}} + 1} k_\perp^2 \tag{6.26}$$

Note that the k^2 term, which is canceled in the absence of phase shift, is due to the increase the conduction electron content of the surface states. The subleading linear term altered with the function $r(\phi)$ of order one $r(\phi) = 2(\cos\phi + \frac{\kappa}{k_z}\sin\phi)/(1 + \alpha\exp(\frac{2\kappa\phi}{k_z}))$. This is the main analytical result of this section that allows to explain the light quisiparticles of SmB_6.

6.2.2 Numerical consideration

Slab calculation robustly shows the characteristic difference that was predicted analytically. Numerical agreement is also excellent. Fig. 6.5 show the original surface state (left) without alternation of the surface f-electrons and (right) the case with removed last layer of f electrons (from both sides of the slab).

Figure 2(b) shows a finite-size slab calculation for the topological surface states when the surface local moment is decoupled from the bulk. This can be achieved by either removing the surface local moments in the calculation or putting the effective chemical potential for the local moment λ to be very large. Note that the topological surface states are quite different compared to the uniform solution [see Fig. 2(a)]: *(i)* First of all, unlike the uniform solution, the Fermi surface is significantly larger. This effect is a consequence

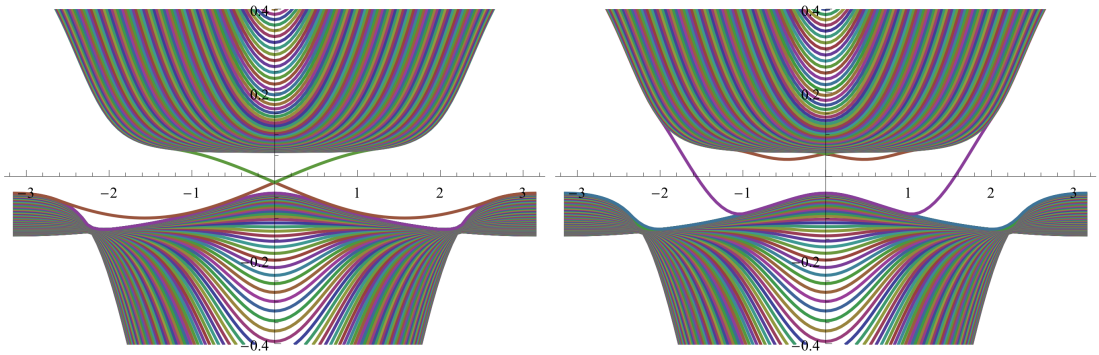

Figure 6.5: Slab calculation for topological Kondo insulator: (Left) for the uniform solution, (Right) surface Kondo breakdown: surface local moments decouples from the rest of the system. Notice the large Fermi surface with high velocity quasiparticles in the case of the surface Kondo breakdown.

of Luttenger's sum rule. The enclosed Fermi surface volume is equal to the total number density. Removing (or adding) an f electron leads to a change from a small Fermi surface to a large Fermi surface. *(ii)* The Dirac point shifts in the valence band in accord with ARPES experiments[118, 132, 112, 113]. *(iii)* Surface states have high velocity v_s in agreement with quantum oscillations [130] and *(iv)* large penetration depth $\kappa \simeq v_s/V$.

Zooming into the first couple of layers, we can show what exactly happens with the surface wave function. Fig. 6.6 shows the plot of $\rho(x) = \psi^\dagger\psi$. One can see that the conduction character increases drastically and thus it is not a surprise to see an increase in the surface state velocity.

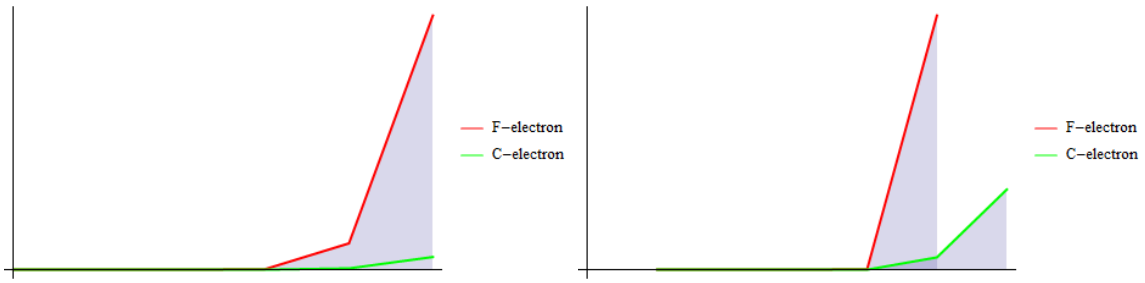

Figure 6.6: Corresponding wave functions densities

6.2.3 Discussion for chapter 6

Surface Kondo breakdown: The Kondo temperature of the surface is much smaller than bulk Kondo temperature due to smaller coordination number on the surface. As a result, the bulk

forms singlets with conduction electrons, leaving unquenched, decoupled local moments on the surface. This effect also known as "Kondo band bending" has been recently explored in 1D [117]. In one dimensions, the decoupled phase is no longer topological [117] . Below, we extend this idea to higher dimensions where we show that the decoupled phase is topological and dominated by the conduction electrons.

Penetration depth: An important consequence of the light quasi-particles is the large penetration depth since penetration depth is $\kappa \simeq v_s/V$. Given the values of v_s and V for SmB_6, we preliminary predict the penetration depth of the surface states to be quite large. The large penetration depth makes the surface states even more protected against disorder in the surface in accord with quantum oscillations at high fields. It is possible to observe the large penetration depth in experiments as a function of film thickness. For film thicknesses less than κ, the surface states will be gapped since the two surface states overlap. They will become gapless for thicker films.

Surface magnetism: Decoupled local moments are prone to magnetic order. RKKY interaction between the local moments and the topological surface states produces not only J, Heisenberg interaction, but also Dzyaloshinskii-Moriya, D and compass anisotropy, A terms[152]. The phase diagram of such a model is quite rich. For $AJ/D^2 > 1$, ground state is an in-plane ferromagnet whereas for $AJ/D^2 < 1$, it is a spiral where the pitch of the spiral is set by D/J[153]. Such a spiral state evolves into a skyrmion crystal in applied magnetic field[154]. Indeed indications of magnetism has been observed as hysteresis in magnetoresistance experiments[155]. The absence of ordered ferromagnetic moment in XMCD experiments[144] suggests that the ground state might be a spiral with no net moment.

To conclude, we have addressed an important puzzle, the light surface states of topological Kondo insulators by employing the simple idea of surface Kondo breakdown. Our results not only reconcile the light surface states and the peculiar shift of valence in Sm but also predicts an important experimentally observable quantity, the penetration depth of the surface states.

Bibliography

[1] W. Kohn, "Nobel Lecture: Electronic structure of matter?wave functions and density functionals," Reviews of Modern Physics 71 pp. 12531266 (1999).

[2] Anderson, P.W. "More is Different" (1972). Science 177 (4047): 393396.

[3] P. Hohenberg and W. Kohn. Inhomogeneous electron gas. Phys. Rev.,136:B864B871, Nov 1964.

[4] W. Kohn and L. J. Sham. "Self-consistent equations including exchange and correlation effects." Phys. Rev., 140:A1133A1138, Nov 1965.

[5] P. Coleman, "Heavy fermions: Electrons at the edge of magnetism", THandbook of Magnetism and Advanced Magnetic Materials, vol. 1. (2007), p. 97. [also avaible arXiv:cond-mat/0612006]

[6] M. Z. Hasan and C. L. Kane, Reviews of Modern Physics 82, 3045 (2010).

[7] X. L. Qi and S. C. Zhang, Reviews of Modern Physics 83, 1057 (2011).

[8] L. Fu, Topological Crystalline Insulators, Phys. Rev. Lett., vol. 106, no. 10, p. 106802, Mar. 2011.

[9] C. Wang, A. C. Potter, and T. Senthil, "Classification of interacting electronic topological insulators in three dimensions.", Science, vol. 343, no. 6171, pp. 62931, Feb. 2014.

[10] W. Shockley, "On the surface states associated with a periodic potential", Phys. Rev., vol. 56, 1939.

[11] L. Fu and C. Kane, "Time reversal polarization and a Z2 adiabatic spin pump," Phys. Rev. B, vol. 74, no. 19, p. 195312, Nov. 2006.

[12] J. Moore and L. Balents, Topological invariants of time-reversal-invariant band structures, Phys. Rev. B, vol. 75, no. 12, p. 121306, Mar. 2007.

[13] L. Fu, C. Kane, and E. Mele, Topological Insulators in Three Dimensions, Phys. Rev. Lett., vol. 98, no. 10, p. 106803, Mar. 2007.

[14] C. L. Kane and E. J. Mele, Z_2 "Topological Order and the Quantum Spin Hall Effect," Phys. Rev. Lett., vol. 95, no. 14, p. 146802, Sep. 2005.

[15] A. Bernevig, T. Hughes and S.C. Zhang, Science 314 , 1757 (2006).

[16] Hsieh, D., Xia, Y., Qian, D., Wray, L., Dil, J. H., Meier, F., Hasan, M. Z. . A tunable topological insulator in the spin helical Dirac transport regime. Nature, 460 (2009)

[17] L. Fu and C. Kane,"Topological insulators with inversion symmetry," Phys. Rev. B, vol. 76, no. 4, p. 045302, Jul. 2007.

[18] Z. Ringel, Y. E. Kraus, and A. Stern, "Strong side of weak topological insulators", Phys. Rev. B, vol. 86, no. 4, p. 045102, Jul. 2012.

[19] Hsieh, D., D. Qian, L. Wray, Y. Xia, Y. S. Hor, R. J. Cava and M. Z. Hasan, 2008, Nature 452, 970.

[20] B. Skinner, T. Chen, and B. I. Shklovskii, "Why Is the Bulk Resistivity of Topological Insulators So Small?," Phys. Rev. Lett., vol. 109, no. 17, p. 176801, Oct. 2012.

[21] M. Neupane, S. Basak, N. Alidoust, S.-Y. Xu, C. Liu, I. Belopolski, G. Bian, J. Xiong, H. Ji, S. Jia, S.-K. Mo, M. Bissen, M. Severson, H. Lin, N. P. Ong, T. Durakiewicz, R. J. Cava, A. Bansil, and M. Z. Hasan, "Oscillatory surface dichroism of the insulating topological insulator Bi_2Te_2Se", Phys. Rev. B, vol. 88, no. 16, p. 165129, Oct. 2013.

[22] G. Aeppli & Z. Fisk, Comm. Condens. Matter Phys. **16**, 155 (1992).

[23] P. Riseborough, ?Heavy fermion semiconductors,? Adv. Phys., no. November 2012, pp. 37?41, 2000.

[24] K. Andres, J. Graebner, and H. Ott, "4f-Virtual-Bound-State Formation in $CeAl_3$ at Low Temperatures," Phys. Rev. Lett., vol. 35, no. 26, pp. 1779?1782, Dec. 1975.

[25] A. Menth, E. Buehler, T. H. Geballe, and B. E. Menth A., "Magnetic and Semiconducting Properties of SmB6," Phys. Rev. Lett., vol. 22, no. 7, pp. 295?297, Feb. 1969.

[26] P. Coleman, "1/N expansion for the Kondo lattice", Phys. Rev. B, vol. 28, no. 9, pp. 52555262, Nov. 1983.

[27] N. Read and D. Newns, "On the solution of the Coqblin-Schreiffer Hamiltonian by the large-N expansion technique", J. Phys. C Solid State Phys., vol. 3273, 1983.

[28] M. Dzero, Eur. Phys. J. B **85**, 297 (2012).

[29] J. W. Allen, B. Batlogg, and P. Wachter, "Large low-temperature Hall effect and resistivity in mixed-valent SmB_6", Phys. Rev. B, vol. 20, no. 12, pp. 48074813, 1979.

[30] Mott, N. F., Phil. Mag., 26, 1015, (1972).

[31] P. Anderson and G. Yuval, "Exact results in the Kondo problem: equivalence to a classical one-dimensional Coulomb gas", Phys. Rev. Lett., vol. 23, no. 2, 1969.

[32] J. Cooley, M. Aronson, Z. Fisk, and P. C. Canfield, ?SmB6: Kondo Insulator or Exotic Metal?,? Phys. Rev. Lett., vol. 74, no. 9, pp. 1629?1632, Feb. 1995.

[33] M. M. Yee, Y. He, A. Soumyanarayanan, D. Kim, Z. Fisk, and J. E. Hoffman, "Imaging the Kondo Insulating Gap on SmB6", pp. 112, Aug. 2013.

[34] P. Syers, D. Kim, M. S. Fuhrer, and J. Paglione, "Tuning bulk and surface conduction in topological Kondo insulator SmB 6", pp. 15, 2014.

[35] S. Wolgast, . Kurdak, K. Sun, J. W. Allen, D.-J. Kim, and Z. Fisk, "Low-temperature surface conduction in the Kondo insulator SmB_6", Phys. Rev. B, vol. 88, no. 18, p. 180405, Nov. 2013.

[36] Z. Yue, X. Wang, D. Wang, J. Wang, D. Culcer, and S. Dou, "Four-fold symmetric magnetoresistance in topological Kondo insulator SmB6 single crystals", Sep. 2013. arXiv:1309.3005

[37] S. Thomas, D. J. Kim, S. B. Chung, T. Grant, Z. Fisk, and J. Xia, "Weak Antilocalization and Linear Magnetoresistance in The Surface State of SmB6", no. 100, Jul. 2013. arXiv:1307.4133

[38] N. Xu, P. K. Biswas, J. H. Dil, R. S. Dhaka, G. Landolt, S. Muff, C. E. Matt, X. Shi, N. C. Plumb, M. Radovic, E. Pomjakushina, K. Conder, a Amato, S. V Borisenko, R. Yu, H.-M. Weng, Z. Fang, X. Dai, J. Mesot, H. Ding, and M. Shi, "Direct observation of the spin texture in SmB6 as evidence of the topological Kondo insulator.", Nat. Commun., vol. 5, no. May, p. 4566, Jan. 2014.

[39] S. Sachdev, *"Quantum Phase Transitions"*, Cambridge University Press, Second Edition (2011).

[40] J. A. Hertz, *"Quantum critical phenomena"*, Phys. Rev. B **14**, 1165 (1976).

[41] A.J. Millis, *"Effect of a nonzero temperature on quantum critical points in itinerant fermion systems."* Phys. Rev. B **48**, 7183 (1993).

[42] P. Coleman, C. Pépin, Q. Si, and R. Ramazashvili, *"How do Fermi liquids get heavy and die?"*, J. Phys. Condens. Matter **13**, R723R738 (2001).

[43] P. Gegenwart, Q. Si and F. Steglich, *"Quantum Criticality in Heavy Fermion Metals"*, Nature Physics, **4**, 186 (2008).

[44] N. Mathur *et al.*, *"Magnetically mediated superconductivity in heavy fermion compounds"* Nature **394**,39 (1998).

[45] D. M. Broun, *"What lies beneath the dome"*, Nature Physics, **4**, 170, (2008).

[46] J. Custers, P. Gegenwart, H. Wilhelm, K. Neumaier, Y. Tokiwa, O. Trovarelli, C. Geibel, F. Steglich, C. Pépin and P. Coleman, *"Break up of the heavy electron at a quantum critical point"* Nature, **424**, 524 (2003).

[47] A. Schroeder *et al.*, *"Onset of antiferromagnetism in heavy-fermion metals",* Nature **407**, 351(2000).

[48] M.C. Aronson, R. Osborn, R.A. Robinson, J.W. Lynn, R. Chau, C.L. Seaman, and M.B. Maple, *"Non-Fermi-Liquid Scaling of the Magnetic Response in UCu 5-xPd_x(x = 1,1.5)",* Phys. Rev. Lett. **75**, 725 (1995).

[49] Q. Si, S. Rabello, K. Ingersent and J.L. Smith, *"Locally critical quantum phase transitions in strongly correlated metals"* Nature **413** 804 (2001)

[50] C. M. Varma, P. B. Littlewood, S. Schmitt-Rink, E. Abrahams, and A. E. Ruckenstein, *"Phenomenology of the normal state of Cu-O high-temperature superconductors",* Phys. Rev. Lett. **63**, 1996 (1989)

[51] V. Alexandrov and Piers Coleman, "Spin and holographic metals," Phys. Rev. B 86, 125145 (2012)

[52] J. M. Maldacena, *"The large N limit of superconformal field theories and supergravity,"* Adv. Theor. Math. Phys. **2**, 231 (1998)

[53] S.S. Lee, *"A Non-Fermi Liquid from a Charged Black Hole: A Critical Fermi Ball,"* Phys. Rev. D **79**, 086006 (2009)

[54] H. Liu, J. McGreevy and D. Vegh, *"Non-Fermi liquids from holography,"* Phys. Rev. D **83**, 065029 (2011)

[55] M. Cubrovic, J. Zaanen and K. Schalm, *"String Theory, Quantum Phase Transitions and the Emergent Fermi-Liquid,"* Science **325**, 439 (2009)

[56] A. Strominger, *"Black hole entropy from near horizon microstates,"* JHEP **9802**, 009 (1998)

[57] D. T. Son, A. O. Starinets, *"Viscosity, Black Holes, and Quantum Field Theory,"* Ann. Rev. Nucl. Part. Sci. **57**, 95 (2007).

[58] T. Faulkner, G. T. Horowitz, J. McGreevy, M. M. Roberts and D. Vegh, *"Photoemission 'experiments' on holographic superconductors,"* JHEP **1003**, 121 (2010)

[59] F. Denef, S. A. Hartnoll and S. Sachdev, *"Quantum oscillations and black hole ringing,"* Phys. Rev. D **80**, 126016 (2009)

[60] S. A. Hartnoll, C. P. Herzog and G. T. Horowitz, *"Building a Holographic Superconductor,"* Phys. Rev. Lett. **101**, 031601 (2008)

[61] T. Hartman and S. A. Hartnoll, *"Cooper pairing near charged black holes,"* JHEP **1006**, 005 (2010)

[62] G. T. Horowitz, *"Introduction to Holographic Superconductors,"* arXiv:1002.1722 [hep-th].

[63] S. A. Hartnoll, *"Lectures on holographic methods for condensed matter physics,"* Class. Quant. Grav. **26**, 224002 (2009)

[64] J. McGreevy, *"Holographic duality with a view toward many-body physics,"* Adv.High Energy Phys. **2010** 723105 (2010)

[65] N. Iqbal, H. Liu and M. Mezei, *"Lectures on holographic non-Fermi liquids and quantum phase transitions,"* arXiv:1110.3814 [hep-th].

[66] S. Sachdev, *"What can gauge-gravity duality teach us about condensed matter physics?",* Annual Rev. Cond. Mat. Phys. **3**, 9 (2012)

[67] P. Breitenlohner and D. Z. Freedman, *"Positive energy in Anti-de Sitter backgrounds and gauged extended supergravity,"* Phys. Lett. **B115** (1982) 197.

[68] M. Henningson and K. Sfetsos, *"Spinors and the AdS/CFT correspondence,"* Phys. Lett. B **431**, 63 (1998)

[69] G. T. Horowitz and M. M. Roberts, *"Zero Temperature Limit of Holographic Superconductors,"* JHEP **0911**, 015 (2009)

[70] D. T. Son and A. O. Starinets, *"Minkowski-space correlators in AdS/CFT correspondence: Recipe and applications,"* JHEP **0209**, 042 (2002)

[71] K. Skenderis, *"Lecture notes on holographic renormalization,"* Class. Quant. Grav. **19**, 5849 (2002)

[72] T. Faulkner and J. Polchinski, *"Semi-Holographic Fermi Liquids,"* JHEP **1106**, 012 (2011)

[73] T. Faulkner, H. Liu, J. McGreevy and D. Vegh, *"Emergent quantum criticality, Fermi surfaces, and AdS(2),"* Phys. Rev. D **83**, 125002 (2011)

[74] S. S. Gubser, S. S. Pufu and F. D. Rocha, *"Quantum critical superconductors in string theory and M-theory,"* Phys. Lett. B **683**, 201 (2010)

[75] J. P. Gauntlett, J. Sonner and T. Wiseman, *"Quantum Criticality and Holographic Superconductors in M-theory,"* JHEP **1002**, 060 (2010)

[76] J. P. Gauntlett, J. Sonner and D. Waldram, *"Universal fermionic spectral functions from string theory,"* Phys. Rev. Lett. **107**, 241601 (2011)

[77] S. -S. Lee, *"Background independent holographic description : From matrix field theory to quantum gravity,"* arXiv:1204.1780 [hep-th].

[78] M. Edalati, K. W. Lo and P. W. Phillips, *"Pomeranchuk Instability in a non-Fermi Liquid from Holography,"* arXiv:1203.3205 [hep-th].

[79] S. A. Hartnoll, C. P. Herzog and G. T. Horowitz, *"Holographic Superconductors,"* JHEP **0812**, 015 (2008)

[80] S. Nakatsuji et al., *"Superconductivity and quantum criticality in the heavy-fermion system β-YbAlB4".* Nat. Phys. **4**, 603 (2008)

[81] T. Albash and C. V. Johnson, *"Holographic Aspects of Fermi Liquids in a Background Magnetic Field,"* J. Phys. A **43** (2010) 345405

[82] P. Basu, J.Y. He, A. Mukherjee and H. -H. Shieh, *"Holographic Non-Fermi Liquid in a Background Magnetic Field,"* Phys. Rev. D **82**, 044036 (2010)

[83] N. Iqbal, H. Liu, M. Mezei and Q. Si, *"Quantum phase transitions in holographic models of magnetism and superconductors,"* Phys. Rev. D **82**, 045002 (2010)

[84] M. Edalati, R. G. Leigh and P. W. Phillips, *"Dynamically Generated Mott Gap from Holography,"* Phys. Rev. Lett. **106**, 091602 (2011)

[85] D. Guarrera, J. McGreevy, *"Holographic Fermi surfaces and bulk dipole couplings,"* [arXiv:1102.3908 [hep-th]].

[86] E. D'Hoker and P. Kraus, *"Holographic Metamagnetism, Quantum Criticality, and Crossover Behavior,"* JHEP **1005**, 083 (2010)

[87] C. P. Herzog and J. Ren, *"The Spin of Holographic Electrons at Nonzero Density and Temperature,"* arXiv:1204.0518 [hep-th].

[88] V. Alexandrov M. Dzero, and P. Coleman, "Cubic Topological Kondo Insulators", Phys. Rev. Lett., vol. 111, no. 22, p. 226403, Nov. 2013.

[89] D. Hsieh, D. Qian, L. Wray, Y. Xia, Y. S. Hor, R. J. Cava and M. Z. Hasan, Nature **452**, 970 (2008).

[90] Y. Xia, D. Qian, D. Hsieh, L.Wray, A. Pal, H. Lin, A. Bansil, D. Grauer, Y. S. Hor, R. J. Cava and M. Z. Hasan, Nat. Phys. **5**, 398 (2009).

[91] P. Roushan, J. Seo, C. V. Parker, Y. S. Hor, D. Hsieh, D. Qian, A. Richardella, M. Z. Hasan, R. J. Cava and A. Yazdani, Nature **460**, 1106 (2009).

[92] T. Zhang, P. Cheng, X. Chen, J. F. Jia, X. C. Ma, K. He, L. L. Wang, H. J. Zhang, X. Dai, Z. Fang, X. C. Xie and Q. K. Xue, Phys. Rev. Lett. **103**, 266803 (2009).

[93] J. Seo, P. Roushan, H. Beidenkopf, Y. S. Hor, R. J. Cava, and A. Yazdani, Nature **466**, 343 (2010).

[94] M. Z. Hasan and C.L. Kane, Rev. Mod. Phys. **82**, 3045 (2010).

[95] X.-L. Qi and S.-C. Zhang, Rev. Mod. Phys. **83**, 1057 (2011).

[96] M. Dzero, K. Sun, V. Galitski, and P. Coleman, "Topological Kondo Insulators," Phys. Rev. Lett., vol. 104, no. 10, Mar. 2010.

[97] T. Takimoto, J. Phys. Soc. Jpn. **80**, 123710 (2011).

[98] M. Dzero, K. Sun, P. Coleman and V. Galitski, Phys. Rev. B **85**, 045130 (2012).

[99] M. T. Tran, T. Takimoto, and K. S. Kim, Phys. Rev. B **85**, 125128 (2012).

[100] F. Lu, J. Zhao, H. Weng, Z. Fang and X. Dai, *pre-print* arXiv:1211.5863 (2012).

[101] S. Wolgast, . Kurdak, K. Sun, J. W. Allen, D.-J. Kim, and Z. Fisk, "Low-temperature surface conduction in the Kondo insulator SmB_6", Phys. Rev. B, Rapid Comm., vol. 88, no. 18, p. 180405, Nov. 2013.

[102] Zhang, X. et al. "Hybridization, inter-ion correlation, and surface states in the Kondo insulator SmB_6" Phys. Rev. X 3, 011011 (2013).

[103] D. J. Kim, S. Thomas, T. Grant, J. Botimer, Z. Fisk, and J. Xia, "Surface hall effect and nonlocal transport in SmB_6: evidence for surface conduction.", Sci. Rep., vol. 3, p. 3150, Jan. (2013).

[104] K. Izawa, T. Suzuki, T. Fujita, T. Takabatake, G. Nakamoto, H. Fujii and K.Maezawa , Phys. Rev. **B** 59, 2599 (1999).

[105] S. Paschen, H. Winkler, T. Nezu, M. Kriegisch, G. Hilscher, J. Custers, and A. Prokofiev, J. Phys: Conf. Ser 200, 012156 (2010).

[106] P. Nyhus, S. L. Cooper, Z. Fisk and J. Sarrao, Phys. Rev. B **55**, 12488 (1997).

[107] A. Yanase and H. Harima, Prog. Theor. Phys. Suppl. **108**, 19 (1992).

[108] V. N. Antonov, B. Harmon and A. N. Yaresko, Phys. Rev. B **66**, 165209 (2002).

[109] H. Miyazaki, Tesuya Hajiri, T. Ito, S. Kunii and S. Kimura, Phys. Rev. **B 86**, 075105 (2012).

[110] J. Derr *et al.*, Phys. Rev. B **77**, 193107 (2008).

[111] J. Jiang *et al.*, arXiv:1306.5664 (2013).

[112] N. Xu, X. Shi, P. K. Biswas, C. E. Matt, R. S. Dhaka, Y. Huang, N. C. Plumb, M. Radovic, J. H. Dil, E. Pomjakushina, K. Conder, A. Amato, Z. Salman, D. McK. Paul, J. Mesot, H. Ding, and M. Shi. Surface and bulk electronic structure of the strongly correlated system smb_6 and implications for a topological kondo insulator. *Phys. Rev. B*, 88:121102, 2013.

[113] E. Frantzeskakis, N. de Jong, B. Zwartsenberg, Y. K. Huang, Y. Pan, X. Zhang, J. X. Zhang, F. X. Zhang, L. H. Bao, O. Tegus, A. Varykhalov, A. de Visser, and M. S.

Golden. Kondo hybridization and the origin of metallic states at the (001) surface of smb_6. *Phys. Rev. X*, 3:041024, 2013.

[114] G. Li et al., arXiv:1306.5221(2013).

[115] S. Thomas *et al.*, arXiv:1307.4133 (2013).

[116] D. J. Kim, J. Xia and Z. Fisk, arXiv:1307.0448 (2013).

[117] V. Alexandrov and Piers Coleman, "End states in a 1-D topological Kondo insulator", Accepted for publication in Phys Rev. B, arXiv Prepr. arXiv1403.6819, Mar. 2014.

[118] M. Neupane, N. Alidoust, S.-Y.-Y. Xu, T. Kondo, D.-J. J. Kim, C. Liu, I. Belopolski, T.-R.-R. Chang, H.-T.-T. Jeng, T. Durakiewicz, L. Balicas, H. Lin, a Bansil, S. Shin, Z. Fisk, M. Z. Hasan, Y. Ishida, D.-J. J. Kim, C. Liu, I. Belopolski, Y. J. Jo, T.-R.-R. Chang, H.-T.-T. Jeng, T. Durakiewicz, L. Balicas, H. Lin, a Bansil, S. Shin, Z. Fisk, and M. Z. Hasan, "Surface electronic structure of the topological Kondo-insulator candidate correlated electron system SmB6.", Nat. Commun., vol. 4, p. 2991, Dec. 2013.

[119] F. Haldane, "Model for a quantum Hall effect without Landau levels: Condensed-matter realization of the parity anomaly", Phys. Rev. Lett., vol. 61, no. 18, 1988.

[120] C. L. Kane and E. J. Mele, "Quantum Spin Hall Effect in Graphene," Phys. Rev. Lett., vol. 95, no. 22, p. 226801, Nov. 2005.

[121] J. E. Moore, "The birth of topological insulators," Nature, vol. 464, no. 7286, Mar. (2010).

[122] R. Roy, "Topological phases and the quantum spin Hall effect in three dimensions," Phys. Rev. B, vol. 79, no. 19, p. 195322, May 2009.

[123] X.-L. Qi, T. L. Hughes, and S.-C. Zhang, "Topological field theory of time-reversal invariant insulators," Phys. Rev. B, vol. 78, no. 19, p. 195424, Nov. 2008.

[124] Z. Wang, X.-L. Qi, and S.-C. Zhang, "Topological Order Parameters for Interacting Topological Insulators," Phys. Rev. Lett., vol. 105, no. 25, Dec. 2010.

[125] H.-C. Jiang, Z. Wang, and L. Balents, "Identifying topological order by entanglement entropy," Nature Phys., vol. 8, no. 12, pp. 902905, Nov. 2012.

[126] R. Nourafkan and G. Kotliar, "Electric polarization in correlated insulators," Phys. Rev. B, vol. 88, no. 15, p. 155121, Oct. 2013.

[127] Z. Wang, X.-L. Qi, and S.-C. Zhang, "Topological invariants for interacting topological insulators with inversion symmetry," Phys. Rev. B, vol. 85, no. 16, p. 165126, Apr. 2012.

[128] Z. Wang and S. Zhang, "Simplified topological invariants for interacting insulators", Phys. Rev. X, vol. 1, no. 3, pp. 15, 2012.

[129] L. Fidkowski and A. Kitaev, "Topological phases of fermions in one dimension", Phys. Rev. B, vol. 83, no. 7, p. 075103, Feb. 2011.

[130] G. Li, Z. Xiang, F. Yu, T. Asaba, B. Lawson, P. Cai, C. Tinsman, A. Berkley, S. Wolgast, Y. S. Eo, D. Kim, C. Kurdak, J. W. Allen, K. Sun, X. H. Chen, Y. Y. Wang, Z. Fisk, and L. Li, Quantum oscillations in Kondo Insulator SmB_6, Jun. 2013.

[131] N. Xu, X. Shi, P. K. Biswas, C. E. Matt, R. S. Dhaka, Y. Huang, N. C. Plumb, M. Radovic, J. H. Dil, E. Pomjakushina, K. Conder, a. Amato, Z. Salman, D. M. Paul, J. Mesot, H. Ding, and M. Shi, "Surface and bulk electronic structure of the strongly correlated system SmB_6 and implications for a topological Kondo insulator", Phys. Rev. B, vol. 88, no. 12, p. 121102, Sep. 2013.

[132] J. Jiang, S. Li, T. Zhang, Z. Sun, F. Chen, Z. R. Ye, M. Xu, Q. Q. Ge, S. Y. Tan, X. H. Niu, M. Xia, B. P. Xie, Y. F. Li, X. H. Chen, H. H. Wen, and D. L. Feng, "Observation of possible topological in-gap surface states in the Kondo insulator SmB6 by photoemission.", Nat. Commun., vol. 4, p. 3010, Dec. 2013.

[133] E. Frantzeskakis, N. de Jong, B. Zwartsenberg, Y. Huang, Y. Pan, X. Zhang, J. Zhang, F. Zhang, L. Bao, O. Tegus, a. Varykhalov, a. de Visser, and M. Golden, "Kondo Hybridization and the Origin of Metallic States at the (001) Surface of SmB_6", Phys. Rev. X, vol. 3, no. 4, p. 041024, Dec. 2013.

[134] Lu, F., Zhao, J., Weng, H., Fang, Z., and Dai, X. (2013). "Correlated Topological Insulators with Mixed Valence" Phys. Rev. Lett.,110(9), 096401.

[135] I. Tamm, Physik. Zeits. Soviet Union 1, 733 (1932).

[136] S. S. Pershoguba and V. M. Yakovenko, "Shockley model description of surface states in topological insulators", Phys. Rev. B, vol. 86, no. 7, Aug. 2012.

[137] J. Duan, D. Arovas, and L. Sham, "Kondo Insulator: p-wave Bose Condensate of Excitons", Phys. Rev. Lett., 1997.

[138] N. Andrei and P. Coleman, "Cooper Instability in the Presence of a Spin Liquid", Phys. Rev. Lett., vol. 62, no. 5, Jan. 1989.

[139] P. Ghaemi and T. Senthil, "Higher angular momentum Kondo liquids", Phys. Rev. B, vol. 75, no. 14, p. 144412, Apr. 2007.

[140] A. Schnyder, S. Ryu, A. Furusaki, and A. Ludwig, "Classification of topological insulators and superconductors in three spatial dimensions", Phys. Rev. B, vol. 78, no. 19, Nov. 2008.

[141] A. Kitaev, "Periodic table for topological insulators and superconductors", AIP Conf. Proc. 1134, 22, 2009,

[142] R. King-Smith and D. Vanderbilt, "Theory of polarization of crystalline solids", Phys. Rev. B, vol 47, 1651-1654 (1993).

[143] A. Kitaev, "Unpaired Majorana fermions in quantum wires", Physics-Uspekhi, vol. 131, 2001.

[144] W. A. Phelan, S. M. Koohpayeh, P. Cottingham, J. W. Freeland, J. C. Leiner, C. L. Broholm, and T. M. McQueen, " Correlation between bulk thermodynamic measurements and the low-temperature-resistance plateau in SmB6", *Phys. Rev. X*, 4:031012, 2014.

[145] NF Mott, Rare-earth compounds with mixed valencies, Philosophical Magazine, vol. 30, no. 2, pp. 403?416, 1974.

[146] X. Li, E. Zhao, and W. Vincent Liu, "Topological states in a ladder-like optical lattice containing ultracold atoms in higher orbital bands.", Nat. Commun., vol. 4, p. 1523, Jan. 2013.

[147] X. Deng, K. Haule, and G. Kotliar, "Plutonium Hexaboride is a Correlated Topological Insulator", Phys. Rev. Lett., vol. 111, no. 17, p. 176404, Oct. 2013.

[148] J. Kim, K. Kim, C.-J. Kang, S. Kim, H. C. Choi, J.-S. Kang, J. D. Denlinger, and B. I. Min, "Termination-dependent Surface In-gap States in a Mixed-valent Topological Insulator: SmB_6", May 2014, arXiv:1405.2511

[149] Piers Coleman. Mixed valence as an almost broken symmetry. *Phys. Rev. B*, 35:5072, 1987.

[150] H. Zhang, C.-X. Liu, X.-L. Qi, X. Dai, Z. Fang, and S.-C. Zhang, "Topological insulators in Bi2Se3, Bi2Te3 and Sb2Te3 with a single Dirac cone on the surface", Nat. Phys., vol. 5, no. 6, pp. 438442, May 2009.

[151] G. E. Volovik, "Fermion zero modes at the boundary of superfluid 3He-B", JETP Lett., vol. 90, no. 5, pp. 398401, Nov. 2009.

[152] Jia-Ji Zhu, Dao-Xin Yao, Shou-Cheng Zhang, and Kai Chang. Electrically controllable surface magnetism on the surface of topological insulators. *Phys. Rev. Lett.*, 106:097201, 2011.

[153] S. Banerjee, O. Erten, and M. Randeria. Ferromagnetic exchange, spin-orbit coupling and spiral magnetism at the $laalo_3/srtio_3$ interface. *Nat. Phys*, 9:626, 2013.

[154] S. Banerjee, J. Rowland, O. Erten, and M. Randeria. Skyrmions in two-dimensional chiral magnets. *Phys. Rev. X*, x:xxx, 2014.

[155] Y. Nakajima, P. S. Syers, X. Wang, R. Wang, and J. Paglione. One-dimensional edge state transport in a topological kondo insulator. *arXiv*, page 1312.6132, 2013.